Electromagnetic interactions of high energy cosmic my muons

R. B. Coats

PLATE I

FRONTISPIECE

THE DURHAM VERTICAL

BURST EXPERIMENT

ELECTROMAGNETIC INTERACTIONS OF HIGH ENERGY COSMIC RAY MUONS

by

R. B. Coats, B.Sc.

A Thesis submitted to the

University of Durham

for the Degree of Doctor of Philosophy

August, 1967.

CONTENTS

ABSTRACT

Electromagnetic interactions of high energy muons incident in the nearly horizontal direction at Durham, 198 ft. above sea level, have been studied by detecting electron-photon bursts produced in iron absorbers. Over the measured burst size range, bremsstrahlung and knock-on electron production were the predominant energy transfer processes. No divergence from accepted theory has been observed for energy transfer in the range 3 - 240 GeV.

A second burst experiment has been performed to measure the spectra of nuclear-active particles incident at Durham in the nearly vertical direction. The observed spectra of both charged and neutral nuclear-active particles show a discontinuity at energies ~ 100 GeV, which can be taken as support for the SU_3 prediction that a proton is a tightly bound system of three charged quarks. This interpretation would indicate a quark mass of 10 GeV, and that high energy protons dissociate into their constituent quarks in about 18% of their collisions above threshold (1800 GeV). A further implication is that quarks interact strongly in the atmosphere, otherwise telescope detectors would have recorded an abundance of quarks. A decrease in the nucleon attenuation length from 127 gm. cm^{-2} to a value of 117 gm. cm^{-2} for sea level nucleon energies > 100 GeV would also account for the observed discontinuity.

PREFACE

This thesis describes work performed in the Physics Department of the University of Durham by the author while he was a Research Student under the supervision of Dr. F. Ashton.

An experiment to investigate electromagnetic interactions of muons has been performed to test the predictions of quantum electrodynamics at high energies. The development, building and day-to-day running of the apparatus has been the sole responsibility of the author, as also has been the analysis and interpretation of the data, and the theoretical calculations. Preliminary results were presented at the London Conference on Cosmic Rays by Ashton et al (1965), and a further paper based on superior statistics has been presented at the International Conference on Cosmic Rays at Calgary by Ashton et al (1967b).

The author has also performed a second experiment in which the spectra of nuclear-active particles at sea level have been measured. Again the running, analysis and interpretation of the data has been his sole responsibility. The results have been reported by Ashton et al (1967c) at the Calgary Conference on Cosmic Rays.

The author has investigated theoretically the light collection properties of the light guides in the scintillators, and a paper giving details of the characteristics of the scintillation counters has been published in Nuclear Instruments and Methods (1965).

CHAPTER 1

INTRODUCTION

1.1 General

Prior to 1930 most physical phenomena could be explained adequately in terms of the proton, the electron and the photon, and their interactions with matter through the electromagnetic and gravitational fields. The proton and electron were treated as classical particles, i.e. their charge and mass could be considered as acting at a point. The strength of electromagnetic interactions is characterised by the fine structure constant, which is dimensionless and of magnitude $e^2/hc = 1/137$, where e is the electronic charge, h is Plank's constant and c the velocity of light. On the same scale the strength of the gravitational field is about 10^{-36}, which is many orders of magnitude smaller than the fine structure constant, and accounts for the negligible contribution of the gravitational field in atomic and nuclear physics. However, in the realm of the nucleus itself, it was apparent that very much stranger forces were operative. The nucleus consists of protons and neutrons, and has a net positive charge due to neutrons being uncharged. Calculations showed the repulsive force between protons to be very large. Hence, to account for the stability of nuclei Yukawa (1935) postulated a strong 'nuclear' force acting between nucleons; its strength was unity on the dimensionless scale used to

compare the strengths of the electromagnetic and gravitational fields. Since that time the emphasis of fundamental physics has been on the study of this nuclear force and the particles associated with it.

The only way open to study nuclear phenomena is to examine collisions between high energy particles and target nuclei. This has led in the last thirty years to the building of both particle accelerators and detection devices to give detailed information about nuclear collisions. The picture that has emerged is one of great complexity. An interaction between particles is best expressed as an exchange of matter between the two colliding particles. Hence the close association of particles and fields. If the energy of the collision is above threshold, then the bits of exchange material can appear as additional particles after the collision. The lightest of such fragments is the pion, which was predicted by Yukawa (1935) and subsequently found by Lattes et al. (1947) in nuclear emulsions exposed to the cosmic radiation at mountain altitudes. With the advent of bubble chambers and the development of larger accelerators during the last ten years, a whole range of new particles has been discovered. The understanding and classification of this wide spectrum of subnuclear particles, of which the pion and nucleon are amongst the lowest mass states, is one of the major problems of fundamental physics today.

Progress in classification has been made by studying the

conservation laws which govern particle interactions. The conservation of charge is thought to be an absolute conservation law. A second law - conservation of baryon number (B) - has been formulated to account for the stability of the proton, which is suggested by its abundance in the universe. All baryons eventually decay into a proton together with lighter particles. As the proton is the least massive baryon, it can only decay into lighter particles through annihilation with an anti-proton. Observations on the production of hyperons has led to the third conservation law, applicable to strong interactions. It was noted in π - N collisions that positive or neutral kaons were always associated with Λ or Σ baryons. This can be explained by assigning a hypercharge (Y) to each particle and postulating that hypercharge is conserved in strong interactions.

It is found that particles can be formed into groups. For instance, the spin zero mesons and spin $\frac{1}{2}$ baryons form octets, whilst the spin 3/2 baryon resonances form a decuplet. These symmetry properties of particles can be obtained in a natural way from the assumption that all particles are composed of fundamental building blocks, which have been named quarks by Gell-Mann. The three different types of quark are postulated to have charges of $+\frac{2}{3}$, $-\frac{1}{3}$ and $-\frac{1}{3}$. The half integral spin particles are then a tightly bound combination of three quarks, and zero and integral spin particles are a tightly bound system of a quark and an

antiquark. The concept of quarks has brought some order to the numerous subnuclear particles, and has had a great deal of success in predicting such quantities as mass, magnetic moments and also new particles (e.g. the Ω^-). However, the principal question that nuclear physicists are asking at the present time is whether quarks actually exist, or are they just a convenient mathematical invention?

Since the existence of quarks was first postulated, many experiments have been performed to look for fractionally charged particles. Accelerator experiments carried out at CERN and Brookhaven failed to substantiate the theoretical predictions. This can be due to either the non-existence of quarks, or to the threshold energy for their production being above the present machine limits. The largest machines available today accelerate protons to energies of about 30 GeV. For proton collisions in a hydrogen bubble chamber this corresponds to an energy of ~4 GeV in the C.M. system of the colliding nucleons. This figure then represents a lower limit to the quark mass. Plans have been laid for larger machines. The United States is to commence building a 200 GeV machine in the near future. A 300 GeV machine has been recommended as part of the European accelerator development, and 30 GeV colliding beams are under construction at CERN. However, at the present time, the cosmic radiation provides the only source of particles of energy in excess of 30 GeV. Several groups (e.g. Lambeet al.,(1966), Ashton et al.,(1967)) have taken advantage

of this fact to try and detect quarks produced in collisions between primary cosmic rays and air nuclei, but so far no conclusive experimental evidence has been presented to show the existence of quarks.

Cosmic rays have been used to study strong, electromagnetic and weak interactions. Measurements on the sea level muon spectrum in the vertical and near horizontal directions give information about the nuclear interactions of the primary particles at energies far exceeding those attainable by machines. Similarly the sea level charge ratio of muons also reflects on the primary and subsequent interactions. An important aspect of cosmic ray research is the use of the sea level muon beam as a source of high energy particles. At large angles to the zenith the median muon energy is higher than in the vertical direction due to the increased probability of pion and kaon decay. Also the contamination in inclined directions by nuclear-active particles is thought to be negligible for zenith angles $\theta > 50^{\circ}$.

In the present work two experiments have been performed. Firstly, electromagnetic interactions with energy transfers exceeding 3 GeV have been studied by detecting electron-photon cascades (bursts) produced in local iron absorbers by muons incident at large zenith angles. The second experiment, to measure the spectra of nuclear-active particles at sea level, was carried out in an attempt to establish the existence of quarks.

1.2 Horizontal Burst Experiment

Quantum electrodynamics (Q.E.D.) deals with interactions between charged particles and electromagnetic fields and, as a theory, it has met with considerable success when compared with experiment. Pipkin (1965) has reviewed the present evidence for the validity of Q.E.D. when applied to energies within the capabilities of present day machines. The theory appears to describe very precisely the electromagnetic interactions of low energy (<1 GeV) electrons, photons and muons. The best evidence for the validity of the theory is derived from measurements of the Lamb shift in hydrogen-like atoms and the gyromagnetic ratios of the muon and electron. Until recently measurements up to the largest momentum transfers had been in agreement with theory, but there is some evidence of disagreement from the latest measurements (Pipkin). Only further experimental evidence can show whether the deviation is real. With the advent of accelerating machines capable of producing primary protons of energy ~300 GeV the validity of Q.E.D. at higher energy transfers can be determined precisely using the available secondary beams of muons, electrons and photons. The Horizontal Burst Experiment was undertaken to test the predictions of Q.E.D. at energies beyond the capabilities of the present day accelerators.

The muon appears to behave like a heavy electron, apart from it being unstable (lifetime ~2.2μs). Several experiments have

been carried out to examine the Coulomb interaction between the muon and the electron (e.g. Barton et al., (1966)), but no deviation from the predictions of Q.E.D. has been observed. Such a deviation would either indicate structure in the muon, or that it was interacting through some other field. The present experiment is to study local interactions of muons incident at large zenith angles at Durham (198 ft. above sea level). An account of the experimental arrangement is given in the next chapter. Three aspects of the theoretical analysis - quantum electrodynamics, the incident muon spectrum and electron-photon cascade theory in iron - are reviewed in chapters 3-5. Chapter 6 contains the analysis of the measurements. The feasibility of measuring the high energy muon spectrum ($E\mu > 1000$ GeV) by burst techniques is considered in Chapter 7.

1.3 Vertical Burst Experiment

Nucleons arriving at sea level are the result of primary protons that have made several interactions on their passage through the atmosphere. Due to charge exchange, the spectra of protons and neutrons with energies greater than a few GeV are expected to be identical. At sufficiently high energies, primary protons may dissociate into three quarks, as a result of colliding with air nuclei in the atmosphere. If this process occurs in a large enough fraction of collisions, then a discontinuity in

the sea level nucleon spectra should be observable. Consequently the vertical Burst Experiment was designed to measure the spectra of both charged and uncharged nuclear-active particles at sea level in an attempt to search for such a discontinuity. The spectrum of charged nuclear-active particles is thought to consist primarily of protons and pions, with neutrons as the neutral particles.

The sea level spectrum of protons has been measured by Brooke et al., (1964b) using a magnetic spectrograph in conjunction with an I.G.Y. neutron monitor, for energies $\leq$ 100 GeV. In the Vertical Burst Experiment the energy range has been extended to >1500 GeV. In the region of overlap (40 - 100 GeV) a comparison between the two independent measurements can be made. The experiment is described in chapter 8, together with the method of analysis and the results.

Finally a summary of both experiments is presented in Chapter 9.

CHAPTER 2

THE HORIZONTAL BURST EXPERIMENT

2.1 Introduction

Electromagnetic interactions in iron of high energy cosmic ray muons incident at large zenith angles at sea level have been studied. The apparatus, a scale diagram of which is shown in figure 2.1, consists essentially of two iron targets, F_1 and F_2, each of thickness 25 cms (13.7 radiation lengths), and two scintillation counters, S_1 and S_2, each of area 1.20 m^2 and similar to the counter described in Appendix A. A high energy electron or photon produced in either iron target by an electromagnetic interaction of a muon, will cascade in the iron to produce a burst of electrons and photons. The scintillation pulse produced by the passage of this burst through S_1 or S_2 is used both for the selection of such events and to determine the size of the burst. Visual information about each event is obtained from neon flash tubes.

2.2 The geiger counters

Three trays of geiger counters, G_1, G_2 and G_3 are shown in figure 2.1. 48 counters (20th Century, G60), each of sensitive length 60 cms, make up G_2, which covers an area of 120 x 92 cm^2. The counters are grouped in units of eight, and each unit is connected to one of six quenching units. The outputs from the quenching units are mixed and fed into one

PLATE II

THE DURHAM HORIZONTAL

BURST EXPERIMENT

plan view

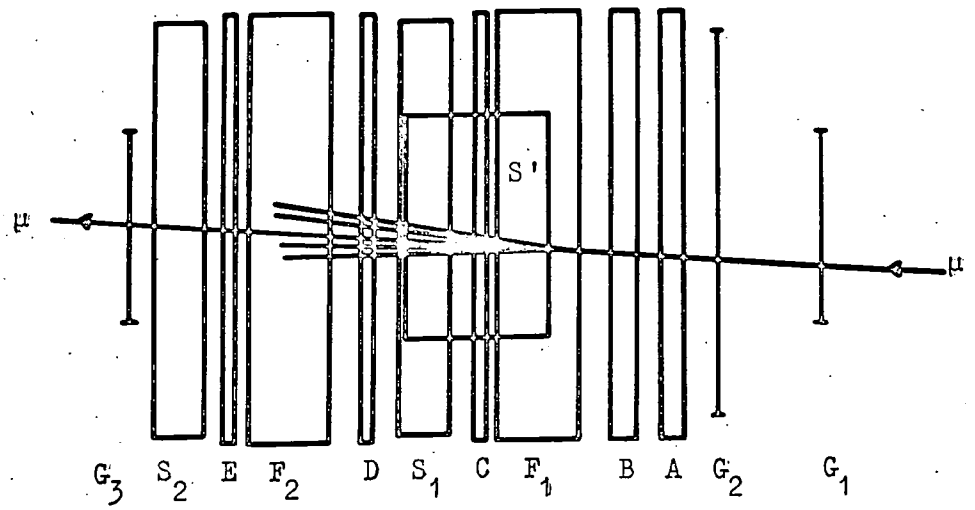

side elevation

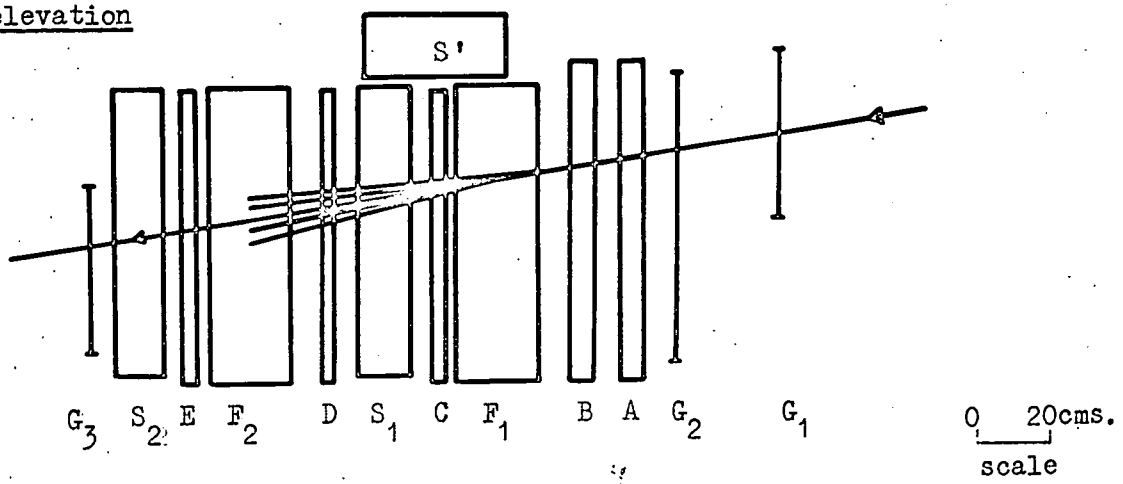

Figure 2.1. Scale diagram of the apparatus.
G - geiger counters; A,B,C,D,E - flash tubes;
S_1,S_2,S' - scintillation counters; F_1,F_2 - iron.
G_1 and G_3 are only used to calibrate the scintillation counters in terms of their response to the passage of single relativistic muons.

channel of a coincidence unit. The total counting rate of the tray is about 2×10^4 per min., which results in each quenching unit being insensitive for 2.8% of the running time. Bursts are selected by a pulse from G_2 in coincidence with a large pulse from either S_1 or S_2.

Calibration of the scintillators is achieved using single particles traversing the apparatus. These are selected by a three-fold coincidence between G_1 and G_3, each containing 14 counters (20th Century G60), and G_2. The rate of singles through the apparatus with this selection arrangement is 67 / hour, which affords a relatively quick method of checking the stability of the scintillation counters.

2.3 The flash tube trays

The positions of the five flash tube trays are illustrated in figure 2.1. Each tray consists of two outer earthed electrodes, and an insulated central electrode to which a high voltage pulse is applied. In trays A and B, two layers of neon flash tubes are stacked on either side of the central electrode. These tubes are filled with commercial neon (98% Ne, 2% He) to a pressure of 60 cms Hg. The dimensions of the glass envelope are: external diameter 1.80 cms., internal diameter 1.55 cms., length 140 cms. Trays C, D and E, adjacent to and covering the area of the scintillators, are of similar construction, but contain only one layer of tubes on each side of the

central electrode.

Efficiency measurements on the flash tubes were carried out using single particles traversing the array. A high voltage pulse (3.0 kv/cm.) was applied to the flash tube trays at a time interval of 17μs after the occurrence of the three-fold coincidence, so as to simulate the conditions under which bursts were recorded (§2.5). The flashes are recorded photographically on Ilford H.P.S. film using a camera (f2 lens, focal length 5 cms) viewing the tubes from a distance of 5.6 metres. Nearly 500 single muons were selected, and the layer efficiencies of each tray were determined by noting the flashes in each layer for every single track. These layer efficiencies were then converted into internal tube efficiencies by correcting for the glass thickness and for gaps between tubes. The following average values for the internal efficiency of the tubes in each tray were obtained: A : 96.5%; B : 96.4%; C : 94.7%; D : 91.5%; E : 92.0%.

A burst consists of a single track in A and B, with a group of flashes in C and D, or E. For analysis purposes a single track in A and B is defined as being $n \geq 3$ flashes in a line. The probability of a true single producing a burst but being rejected on account of there being < 3 flashes in A and B is 0.029%. This figure has been evaluated from the efficiency measurements, and represents a negligible loss of events.

2.4 The scintillation counters

During normal operation the gains of the two photomultipliers in each scintillation counter are matched. This was achieved by two independent methods. Each photomultiplier in turn was placed in a light-tight box and viewed the light pulses generated in the arc-discharge of a mercury-wetted relay (Kerns et al., (1959)). The variation of response as a function of E.H.T. was measured for each tube, and is shown in figure 2.2. The two photomultipliers in S_1 are designated by the letters A_p, C_p, while E_p and G_p refer to the tubes in S_2. These measurements were checked by a second method. With the two scintillation counters in position and the E.H.T. on each tube set according to the light flasher data, single particles traversing the centre of each counter in turn were selected using a small telescope, and the pulse height distributions produced by each photomultiplier were recorded. The mean values of the four distributions agreed closely, inspiring confidence in the former method of matching. During the actual burst experiment the values of the E.H.T. on each tube were as follows:

A_p : 1.40 kv; C_p : 1.39 kv; E_p : 1.23 kv; G_p : 1.20 kv.

The linearity of response of each photomultiplier to variations in the intensity of light incident on the photocathode has been tested. The tubes were again placed in turn

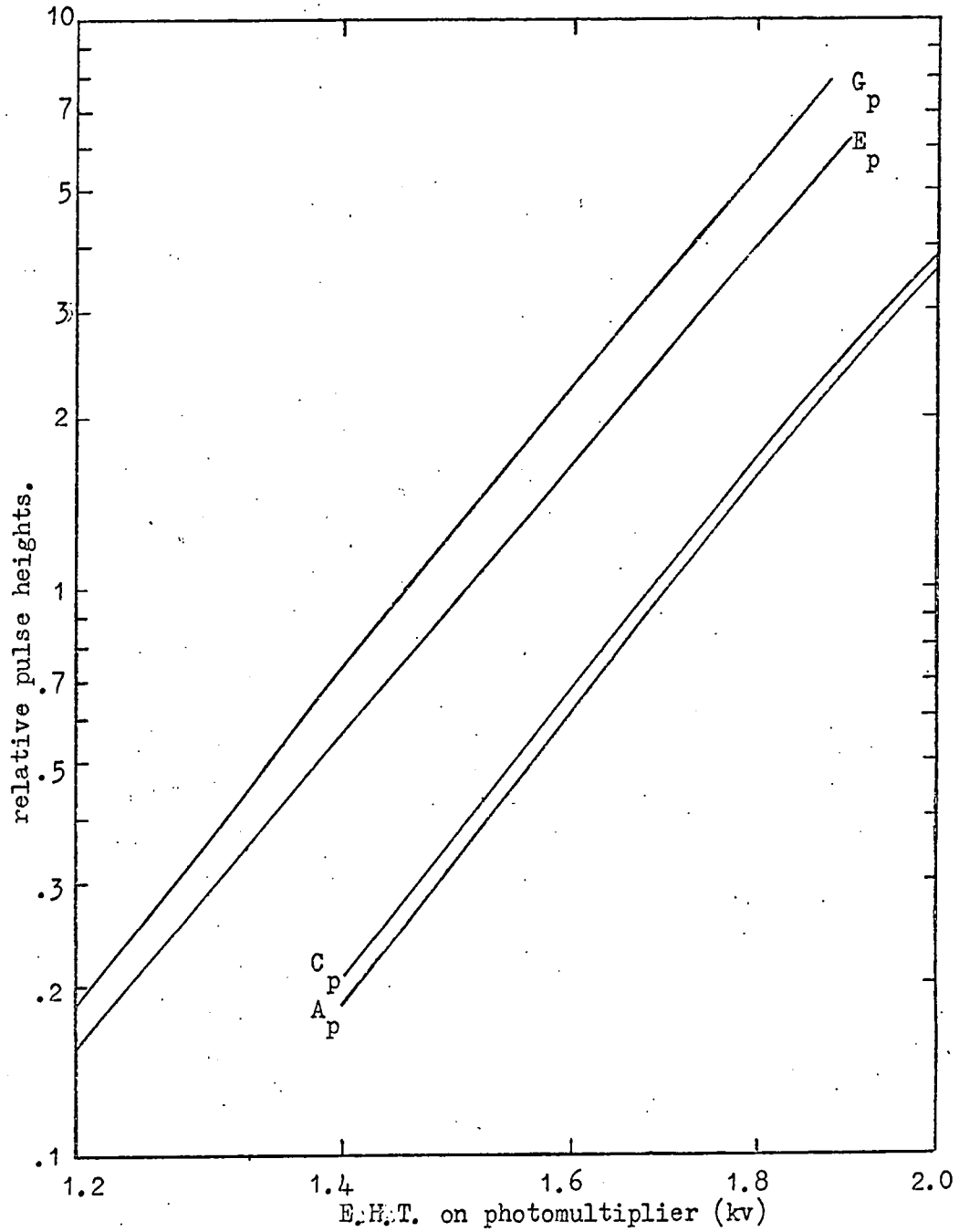

Figure 2.2. variation of response with E.H.T. for the light flasher.

in the light flasher box and run at their operating voltages. Variations in the intensity of light were obtained by means of an optical wedge, a glass strip of varying transparency along its length, quoted by the manufacturers to be 0.13 density units cm^{-1}, where a density unit = $\log_{10} I/I_o$. With the wedge available the intensity could be varied over a range 250 : 1. Measurements on each tube showed the pulse height to be proportional to the number of incident photons over the range of pulse heights relevant to the burst experiments described in this thesis.

The size of a burst is defined as the ratio of the measured pulse height to the mean pulse height produced by a single horizontal ionizing particle traversing the counter at normal incidence. G_1, G_2 and G_3 in coincidence were used to select single muons traversing the scintillators. For each event the pulse heights from S_1 and S_2 were recorded on film, and the flash tube trays photographed. The projected zenith of each single particle was determined from the flash tube data, and each pulse height was corrected for the corresponding increase in track length in the phosphor. The resulting distributions are shown in figure 2.3(a). The mean pulse height for S_1 was 1.82 mv., and that for S_2 was 2.34 mv. Corrections have been made for the increase in track length in the phosphor due to particles incident at

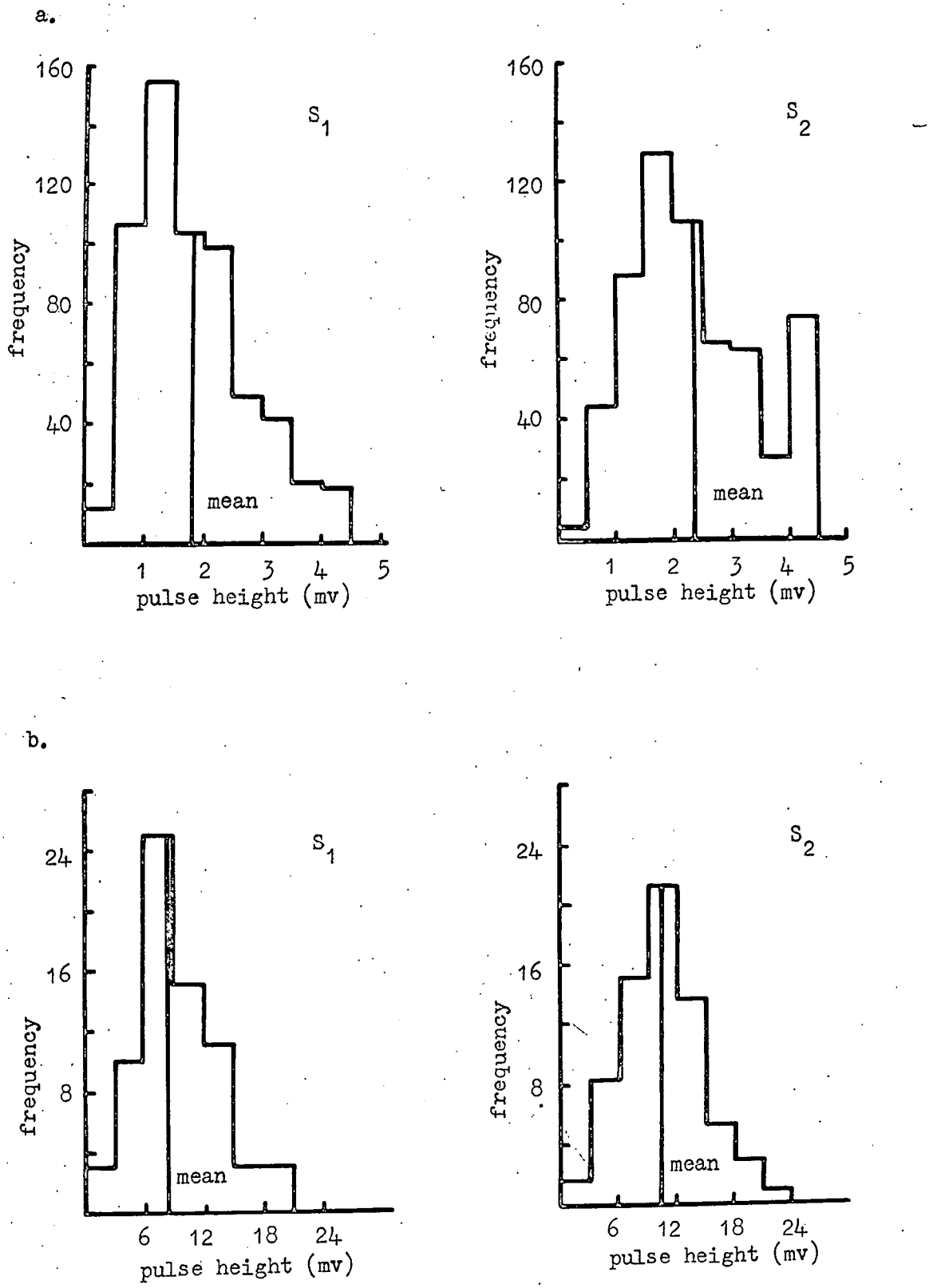

Figure 2.3. Distributions of pulse heights for S_1 and S_2 produced by:

a. horizontal muons selected by G_1, G_2, G_3 coincidence.

b. vertical particles selected by geiger telescope.

inclined directions in the azimuthal plane. As no information was available about the azimuthal angle from the flash tubes, particles were assumed to be incident at the mean azimuth angle of the telescope.

As a check on these measurements, single particles traversing the centre of each counter in a vertical direction were selected by the small telescope, and the resulting distributions recorded. These are displayed in figure 2.3(b). The mean pulse height for S_1 was 8.5 mv, and that for S_2 was 10.2 mv. The track length of a particle travelling vertically through the phosphor is five times that of a horizontal particle, so that the mean pulse height of vertical particles should be a factor of five greater than that produced by horizontal particles. The observed ratios are 4.92 and 4.85 for S_1 and S_2 respectively, which is in good agreement with expectation.

Extensive Air Showers incident on the array can simulate the triggering conditions of a burst produced by a nearly horizontal muon. In order to reduce the rate of these triggers a scintillation counter, s′ (figure 2.1), was included in anti-coincidence with the selection system. The phosphor of s′, medicinal paraffin plus 0.5 $g.l^{-1}$ paraterphenyl, 0.005 $g.l^{-1}$ POPOP and 10% Shellsol A was of area 48 x 73 cm^2 and was viewed by one 5" photomultiplier (E.M.I. type 9583B) in optical contact. A mirror on the face opposite the photo-

multiplier was incorporated so as to double the amount of light available for collection. The photomultiplier was operated at an E.H.T. of 2.0 kv, and biassed so that a single particle traversing the counter vertically produced a veto pulse. The single particle peak was determined using the small telescope to select particles traversing the counter. The most probable pulse height was 1.20 volts. As a check the total integral distribution of pulse heights was measured for the whole counter, and a value of 1.35 volts was obtained for the most probable pulse height of the differential distribution. The discrepancy is probably due to the longer track lengths of particles traversing the counter at angles other than normal incidence. The discriminator was biassed to select single particles, and a veto pulse applied to the burst selection system whenever this criterion was satisfied. By this means 90% of showers which would otherwise have triggered the apparatus were rejected. The dead time introduced by the anti-coincidence counter amounted to 0.05% of the total running time.

2.5 The electronics

A block diagram of the electronics is shown in figure 2.4. Pulses from the two photomultipliers in one scintillator are added after being amplified by two head units, and the resulting pulse then passes through a fan-out unit, which reproduces an identical pulse on three output channels.

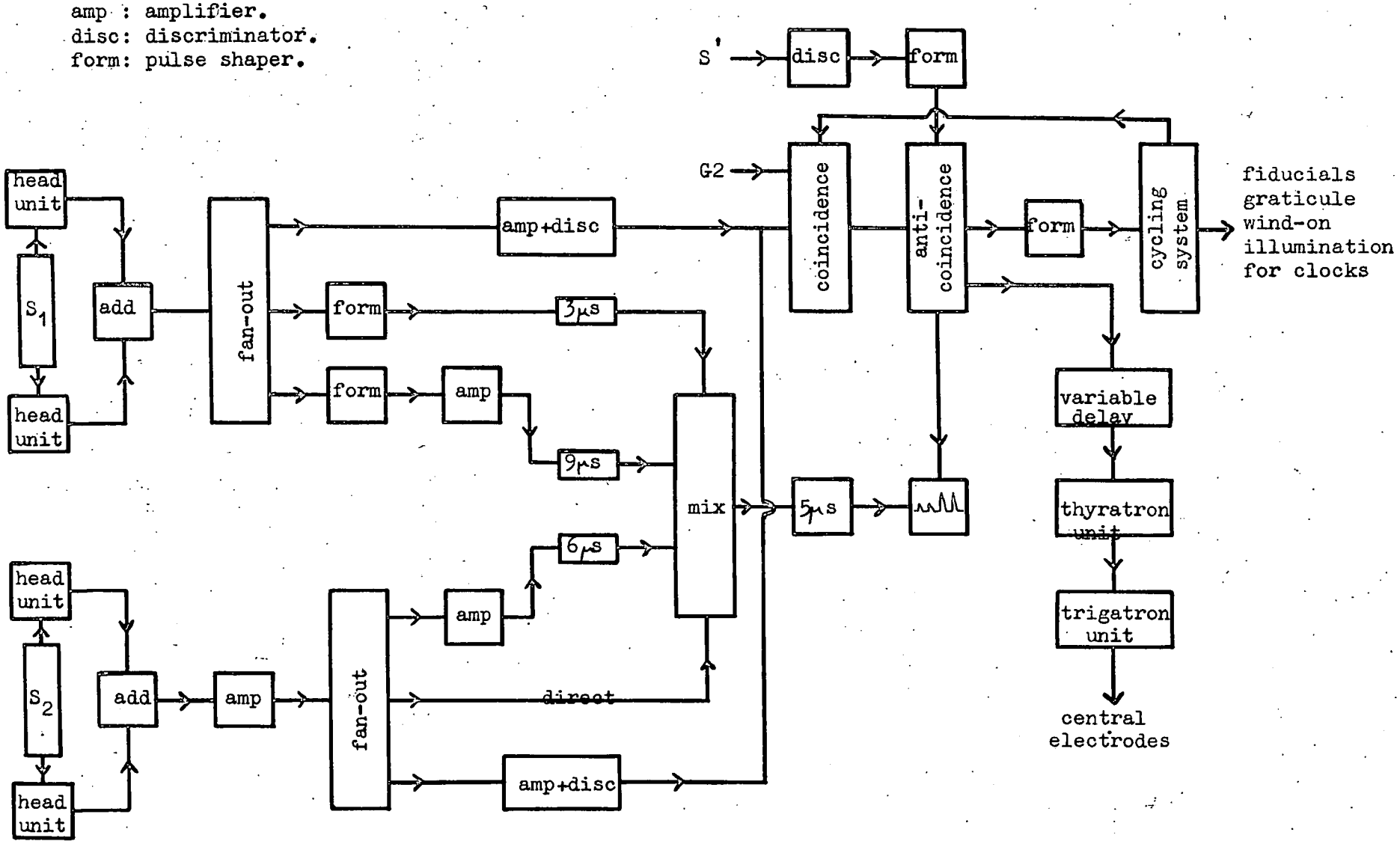

Figure 2.4. Block diagram of the electronics.

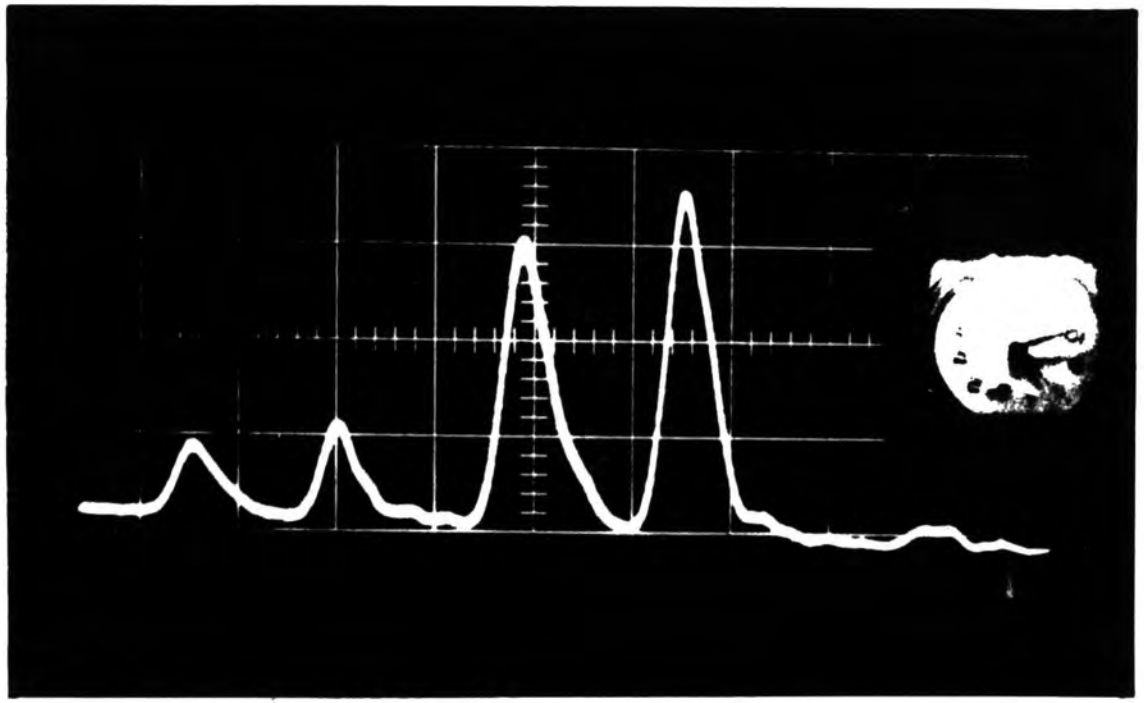

Figure 2.5. Pulse information for a typical event.

Two of these channels are used for display, and the third for selection. Both display channel pulses feed into one oscilloscope, but one is amplified so as to increase the dynamic range of observable pulse heights. An identical system is employed for the second scintillator. The four pulses, which are suitably delayed so that each is separated from the next by 3μs, are recorded photographically for each event. A typical event is shown in figure 2.5. The first and second pulses correspond to S_1 and S_2 respectively, while the third and fourth pulses are the respective amplified versions of the first and second pulses.

The pulse on the selection channel of each scintillator passes through a discriminator, which is preceded by a variable gain amplifier so as to increase the dynamic selection range. The outputs of the two discriminators are mixed before being fed into one channel of a Rossi coincidence unit. The second channel of the unit is connected to the geiger counters in tray G_2. When a coincidence occurs, the resulting selection pulse feeds through an anti-coincidence gate. If the gate is open (no signal from s′) the oscilloscope is triggered externally, and the pulse information recorded on film. The gate output pulse is delayed for 17μs so as to avoid pick-up from the high voltage pulse during the recording of the scintillator pulses. It then triggers a unit consisting of an 8 kv hydrogen thyratron and a pulse transformer. This in turn triggers an enclosed spark gap (Trigatron cv85) which discharges a bank of condensors through a pulse transformer. The resulting high voltage pulse, of magnitude 10 kv and duration 3μs, is fed

onto the central electrodes of the flash tube trays. The gate output pulse also starts a cycling system, which firstly paralyses the Rossi unit and then, by means of microswitches, illuminates fiducial marks and a clock near the flash tubes. The graticule on the oscilloscope is also illuminated, and the two films are then wound on. Finally the paralysis is removed on completion of the 8 second cycle, and the system is ready so select another event.

2.6 Running time

Corrections to running times for the dead time of the electronics have been made. The cycling system dead time becomes appreciable when selecting small bursts, due to the large photography rate. For example the photography rate was 67 hr^{-1} when the discriminators were set to select bursts of size >15 particles, resulting in a dead time of about 15% of the total running time. For larger burst sizes the dead time becomes negligible.

The apparatus was run during the period 29th June 1965 to 10th August 1965 selecting bursts produced in F_1, and a total useful running time of 489 hours was recorded. Between 11th February 1966 and 8th July 1966 bursts produced in either F_1 or F_2 were selected during a useful running time of 1442 hours. The first runs are grouped together and are referred to as the A series. The latter are the B series.

CHAPTER 3

MUON SPECTRUM AT LARGE ZENITH ANGLES

3.1 Introduction

Cosmic rays which arrive at large zenith angles have been studied for two reasons: firstly, because they constitute a very pure beam of muons of high average energy, and secondly, because information can be derived about the parent particles from which they have been produced as decay products. Advantage has been taken of the former fact in the Horizontal Burst Experiment. However, before any predictions of expected burst spectra can be made, it is necessary to know the spectrum of muons incident on the apparatus. In the following sections a survey of the previous theoretical treatments and also of the past experimental work has been undertaken in order to determine the 'best' spectrum of muons in inclined directions.

3.2 Theoretical treatments

The problem of deriving the momentum spectra of muons at large zenith angles has been undertaken by several workers. In general the procedure is to commence with the sea level vertical muon spectrum and from it calculate the production spectra of parent particles. These production spectra are then used to predict the muon spectrum in inclined directions.

Smith and Duller (1959) calculated the change in zenith angle dependence with respect to a flat earth for muons in the energy range 40-160 GeV. In the 'flat earth' approximation the thickness of the earth's atmosphere at zenith angle θ is taken to be proportional to sec θ. This is valid for $\theta < 65^{\circ}$.

Zatsepin et al., (1961) took the curvature of the earth into account, and also the energy spread of muons from their parent particles. In treating the energy loss of muons it was assumed that the muons traverse a large portion of their geometric path in an atmosphere of low density where the probability of energy loss may be ignored, and the decay probability calculated, and that the only important energy loss occurs in the last fraction of the path, which is so short that decay is unimportant. The results are presented in the form of a ratio of the intensity of muons with a given energy at zenith angle θ to the intensity of vertical muons with the same energy, and cover the energy range 10^{11} - 10^{14} ev for all angles. The approach of treating decay loss and energy loss as separate entities is only approximate, but is valid in the energy range considered. The calculations assume an attenuation length of 75 gm. cm^{-2} for nucleons, pions and kaons.

In the treatment of Allen et al., (1961) the energy spread of muons produced in the decay of pions is neglected. It is thought that this introduces an error of about 1%. Only the $K_{\mu 2}$ decay mode is taken into consideration, and a single level of production has been assumed. Allen et al., concluded that the

inclined muon spectrum is insensitive to the parents of the muons. This has been shown to be incorrect.

Maeda (1964), commencing from integral expressions for the pion and $K_{\mu 2}$ production spectra, has calculated sea level muon spectra in inclined directions for energies in the range 40 - 10^5 GeV for both pion and $K_{\mu 2}$ parents. The attenuation length was taken to be 120 g. cm^{-2} for both pions and nucleons.

The work of Osborne (1966) differs from the earlier calculations in that fewer approximations are made. In the case of kaons as parents of muons the effect of all decay modes is considered instead of only the $K_{\mu 2}$ mode as in other calculations. The vertical spectrum adopted is that of Osborne et al. (1964), which will be referred to as the O.P.W. spectrum. This spectrum was derived from the Durham magnetic spectrograph measurements at low momenta, together with the underground intensity-depth measurements up to an energy of 7000 GeV. The rate of energy loss of muons in the atmosphere, and the energy spread of muons from the decay of pions was taken into account, together with the distribution of heights of origin of the muons throughout the atmosphere. The attenuation length of both protons and pions was taken to be 120 g.cm^{-2}.

A comparison of the theoretical spectra at 80° as predicted by the various workers is shown in figure 3.1. The predictions of Osborne and Zatsepin et al. are in good agreement in the overlapping energy range, i.e. 100-1000 GeV. The Zatsepin spectrum has been obtained by using the O.P.W. spectrum

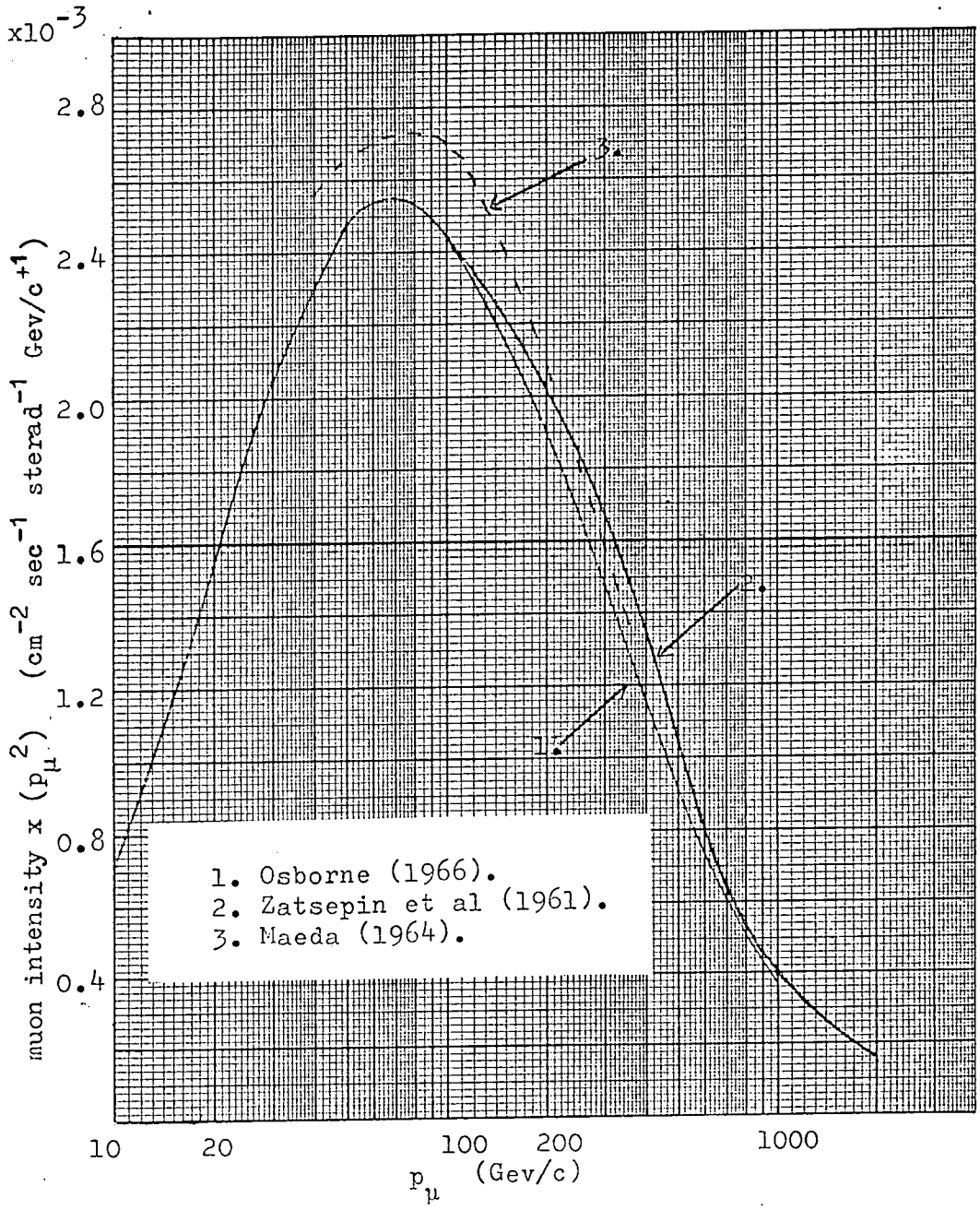

Figure 3.1. Comparison of theoretical muon spectra at 80°.

in conjunction with the ratios calculated by Zatsepin et al. at 80°. The theoretical curve of Maeda, deduced in a manner similar to that used to derive the Zatsepin curve, agrees reasonably at energies in excess of 200 GeV but predicts a greater flux at lower energies, the excess being typically ~10% at 100 GeV.

The various approaches to derive the momentum spectra of muons incident in inclined directions have made different estimates of the contribution of kaon decay to the muon flux. Comparison by Said (1966) between the measured muon spectra in the zenith angle range 82.5°-90° and the expected spectra based on different assumptions about the kaon contribution shows the best value of the K/π ratio to be

$$K/\pi = 0.42 \pm 0.20 \quad \text{for} \quad 70 \leqslant E\ (S/L) \leqslant 2000 \text{ GeV}.$$

There is not much evidence that the fraction of charged particles other than pions is very different from the value measured by emulsion experiments and quoted by Perkins (1961) as

$$(N_X^{\pm}) \,/\, (N_X^{\pm} + N_{\pi}^{\pm}) = 0.18 \pm 0.05 \quad \text{for } E \leqslant 10^{14} \text{ev}.$$

In deriving this fraction the assumption has been made that all γ-rays observed in emulsions derive from π^{o} decay, and that $N(\pi^{o}) = \frac{1}{2}N(\pi^{\pm})$.

In the burst calculations the measured muon spectra will be used as far as possible, but where there is no available data, predicted curves based on $\pi - \mu$ decay will be used.

3.3 Experimental results

Measurements on the total intensity of particles at large zenith angles, made by Jakeman (1956) and other workers, indicated a greater intensity of high energy particles incident in nearly horizontal directions than in the vertical direction, as was expected. With the introduction of magnetic spectrographs measurements of the muon momentum spectra were made.

Pak et al. (1961) determined the spectrum of muons at 68° in the momentum range 2-70 GeV/c using a spectrograph. At about the same time measurements were made on the absolute cosmic ray intensity in the momentum range 1-100 GeV/c at zenith angles between 65° and 85° by Allen et al. (1961) using an emulsion spectrograph at Durham. The statistics of the latter experiment were limited, so that the results were presented in the form of an integral intensity as a function of zenith angle, rather than as a momentum spectrum.

More recently a magnetic spectrograph, comprising a 'solid iron' magnet with counter reading, has been operated at Durham by Ashton et al. (1963) and the momentum spectrum of muons incident at $\theta = 80^{\circ}$ measured in the range 1.5-40 GeV/c. This is displayed in figure 3.2, and it is found that the measured spectrum is close to that expected if all muons are derived from pions. The spectrograph used three trays of geiger counters for selection, and its axis was inclined at 55° $36'$ east of magnetic north. An improvement to the Durham spectrograph was made by

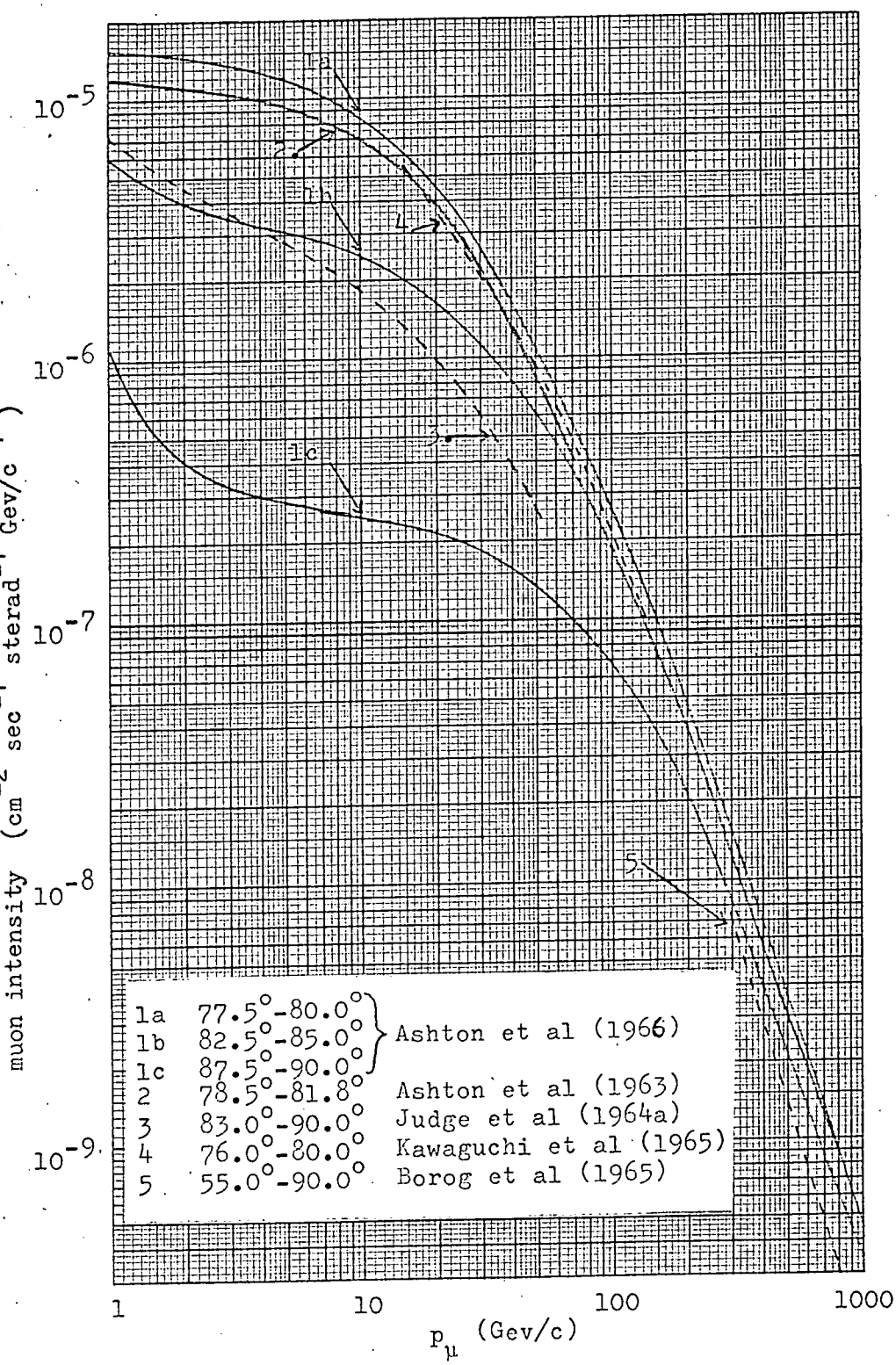

Figure 3.2. Comparison of muon spectrum measurements at large zenith angles. 1-4 are spectrograph measurements, and the curves represent the best fit to the experimental points. 5 is a calorimeter experiment.

Ashton et al. (1966) by incorporating trays of neon flash tubes into the apparatus in order to increase the accuracy of track location. The accepted zenith angle range was 77.5°-90°, and the axis was re-orientated to 7.8° east of magnetic north. Over 10,000 particles were accepted in a total running time of about 1500 hours. The measurements are in agreement with the predictions of Osborne (1966), which are shown in figure 3.2. The Durham spectrograph was again modified by MacKeown et al. (1965) by doubling the magnetic path and increasing the longitudinal dimensions of the apparatus, so as to increase its resolution. The zenith angle acceptance range was reduced to 82.5°-90°. Nearly 4000 particles ($p_{\mu} > 5.8$ GeV/c) were analysed, and the resulting spectra again found to be in agreement with the theoretical curves of Osborne.

Kawaguchi et al. (1965) have measured the spectrum of muons up to 170 GeV/c using the Nagoya spectrometer. A total of 8343 particles incident at $\theta = 78^{\circ}(\pm 2^{\circ})$ were analysed. The curve best fitting the measurements is shown in figure 3.2. This is in agreement with the Durham measurements within experimental error. Measurements have also been made by Judge et al. (1964a) on the momentum spectrum of muons arriving at sea level in the angular range 83°-90° using the Nottingham spectrograph with its axis aligned east-west. The best fit to these measurements is also displayed in figure 3.2.

Borog et al. (1965) have studied showers initiated by muons at large zenith angles by means of an ionisation calorimeter.

An integral burst spectrum was obtained, produced by muons incident at $\theta \geq 55^{\circ}$. This has been converted into the incident muon spectrum, which is shown in figure 3.2. A linear translation has been assumed by the authors in which 70% of the muon energy is transferred into γquanta in the bremsstrahlung process. The discrepancy is absolute magnitude between the Borog et al. spectrum and the spectra of Osborne probably arises from the method for converting from the burst spectrum to the muon spectrum.

The momentum spectrum of muons in the east-west azimuth has been determined at Nottingham by Judge et al. (1964b) at $\theta = 60^{\circ}$ using a spectrograph of m.d.m. 28 GeV/c, and is displayed in figure 3.3. A comparison with the spectrum of Allen et al. (1961), calculated for muons incident from geomagnetic north and corrected for scattering and geomagnetic deflection, shows agreement with the experimental results at momenta in excess of 10 GeV/c. However, at lower momenta, there is a discrepancy between prediction and measurement, the predicted flux from the north being less than the measured flux from the east. This is inconsistent with geomagnetic deflection expectations.

3.4. Conclusions

In order to calculate the expected burst spectra, the spectrum of muons ($E_{\mu} > 3$ GeV) in the zenith angle range 50°-90°

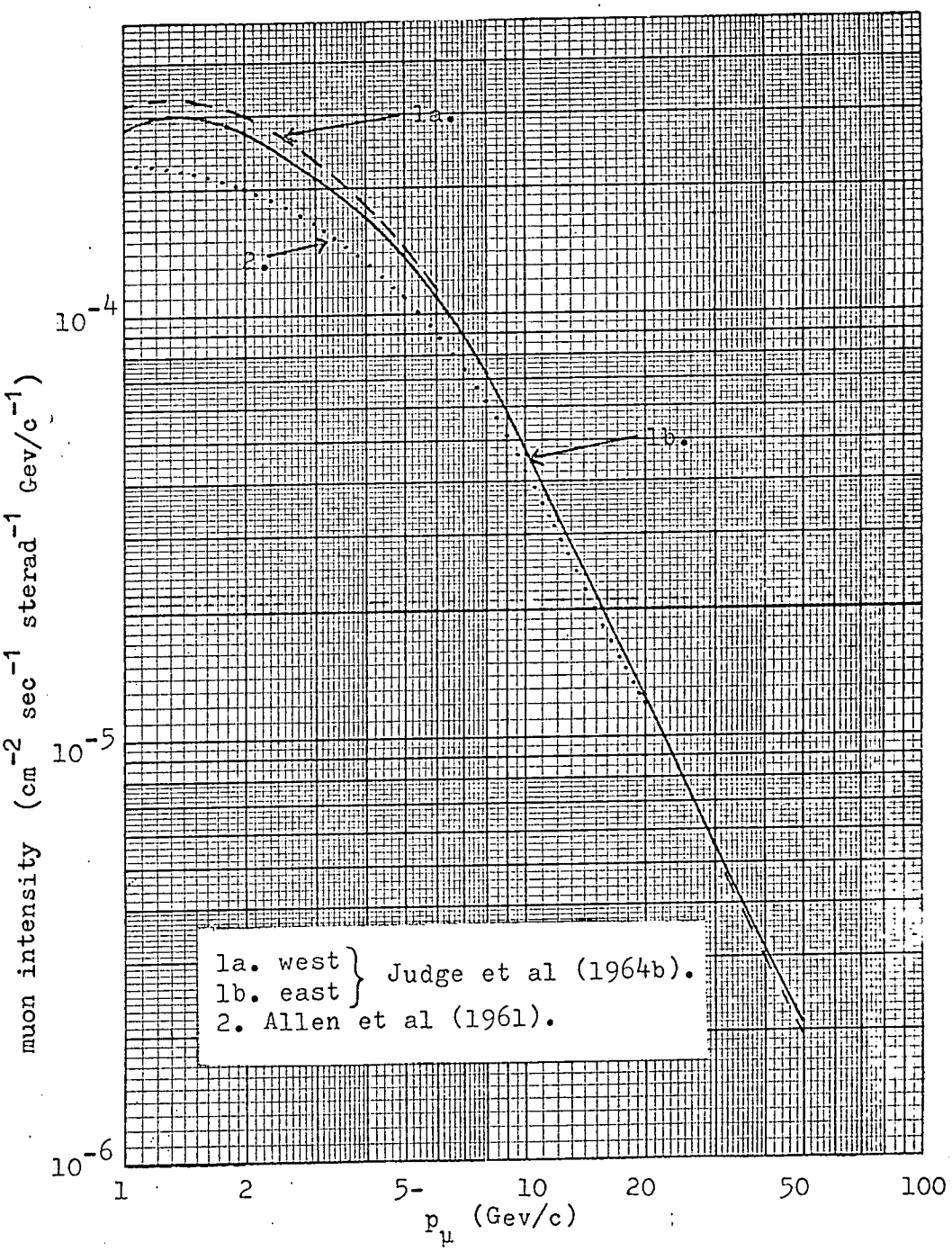

Figure 3.3. Comparison of measured muon spectra at 60° for different azimuth angles.

(1938) and is represented by:

$$\phi_{COL}(E,E')\,dE' = \frac{2Cm_e c^2}{\beta^2}\,\frac{dE}{(E')^2}\left\{1 - \beta^2\,\frac{E'}{E_m} + \tfrac{1}{2}\left(\frac{E'}{E+mc^2}\right)\right\}$$

where βc is the velocity of the particle and Z,A refer to the material.

$C = 0.15\ Z/A$ gm. cm^{-2} represents the total 'area' covered by the electrons in one gm. cm^{-2}, each electron being considered as a sphere of radius equal to the classical electron radius. From consideration of the conservation of energy and momentum, there is a maximum transferable energy , E_m, given by

$$E_m' = 2m_e c^2\,\frac{p^2c^2}{m_e^2c^4 + m^2c^4 + 2m_e c^2\,(p^2c^2 + m^2c^4)^{\frac{1}{2}}}$$

where m, m_e are the masses of the particle and the electron respectively. In these calculations it was assumed that the particle has a normal magnetic moment as predicted by the Dirac theory for spin $\frac{1}{2}$ particles.

4.1.3 Bremsstrahlung

The distance from the nucleus at which the radiation process occurs is important in the theoretical treatment. If the distance is large compared with the nuclear radius and small compared with the atomic radius, then the electromagnetic field of the nucleus can be treated as being the Coulomb field of a point charge Ze at the centre of the nucleus, and the screening effect of the outer electrons can be neglected. Screening is

important when the distance becomes of the order of the atomic radius. On the other hand, for interactions close to the nucleus, the electromagnetic field can no longer be considered as being due to a point discharge, and corrections have to be introduced into the theory.

In the case of electrons undergoing bremsstrahlung, the interaction takes place at distances large compared with the nuclear radius, so that the nucleus can be considered as a point charge, although screening is important. On account of the larger mass of the muon, radiation occurs much closer to the nucleus. Screening can be neglected to a larger extent, but at such close distances the field can no longer be treated as the Coulomb field of a point charge. The spin of the radiating particle has also to be taken into account.

Christy et al. (1941) calculated the differential radiation probability for particles of mass m, spin $\frac{1}{2}$ and normal magnetic moment, making the following assumptions:

1. The kinetic energy of the particle is large compared with its rest mass.
2. The potential of a nucleus is that of a point charge for distances larger than the nuclear radius, r_n, and is constant for distances less than r_n.
3. Screening by the outer electrons is negligible. The screening effect is thought to become important for primary energies $\geq 137\ (m^2c^2/m_e)\ Z^{-\frac{1}{3}}$.

The general expression of the radiation probability is:

$$\phi_{rad}(E,E')dE' = \alpha \frac{N}{A} Z^2 r_e^2 \left(\frac{m_e}{m}\right)^2 \frac{dE'}{E'} F(U,v),$$

where E is the kinetic energy of the incident particle (rest mass (mc^2).

E' is the energy of the secondary photon.

$v = E'/U$ is the fractional energy transfer.

$U = E + mc^2$ is the total energy of the incident particle

α is the fine structure constant.

N is Avagadro's number.

$F(U,v)$ is a slowly varying function of U and v which, for a spin $\frac{1}{2}$ particle, is given by :

$$F(U,v) = \frac{16}{3} \left(\tfrac{3}{4} v^2 + 1-v\right) \left\{ \ln \left(\frac{2U}{mc^2} \frac{\hbar}{mcr_n} \left(\frac{1-v}{v} \right) \right) - \tfrac{1}{2} \right\}$$

4.1.4 Direct pair production

When a particle passes through the electromagnetic field of a nucleus, and close to the nucleus, there is a certain probability of one of the virtual photons associated with the field of the particle undergoing materialization to produce an electron-positron pair. Although the spin of the incident particle is comparatively unimportant, the screening effect of the outer atomic electrons has to be taken into account.

Rossi (1952) has given the probability per gm.cm^{-2} of a particle (mass m and kinetic energy E) producing an electron-

positron pair with energy between E′ and (E′ + dE′) :

$$\phi_{pp}(E,E')dE' = \frac{8}{\pi} \alpha^2 \frac{N}{A} Z^2 r_e^2 L(U,v)$$

where L(U,v) is a function depending on U and v.

From the calculations of Bhabba (1935) four distinct regions, depending on the energy of the pair and the degree of shielding, give rise to different expressions for L(U,v), and these are given by Rossi (1952).

Murota et al. (1956) [M.U.T.] have calculated the cross-section for the creation of an electron-positron pair by an energetic charged particle using the Feynman-Dyson method, which is valid so long as the energies of the particles are large in comparison with their irrespective rest masses. In the Bhabba approach the incident particle is regarded as being a classical one moving along a straight line with uniform velocity, the field of which is replaced by a classical field. This approximation gives a correct description only when the energy transferred to the pair is small compared with the energy of the incident particle. This approximation has not been made in the M.U.T. approach, which considers the whole range of possible energy transfers more rigorously.

The cross-sections for the three processes are shown in figure 4.1 for typically a 100 GeV muon in iron. For low energy transfers, direct pair production and the collision process predominate, whereas bremsstrahlung is the major process for

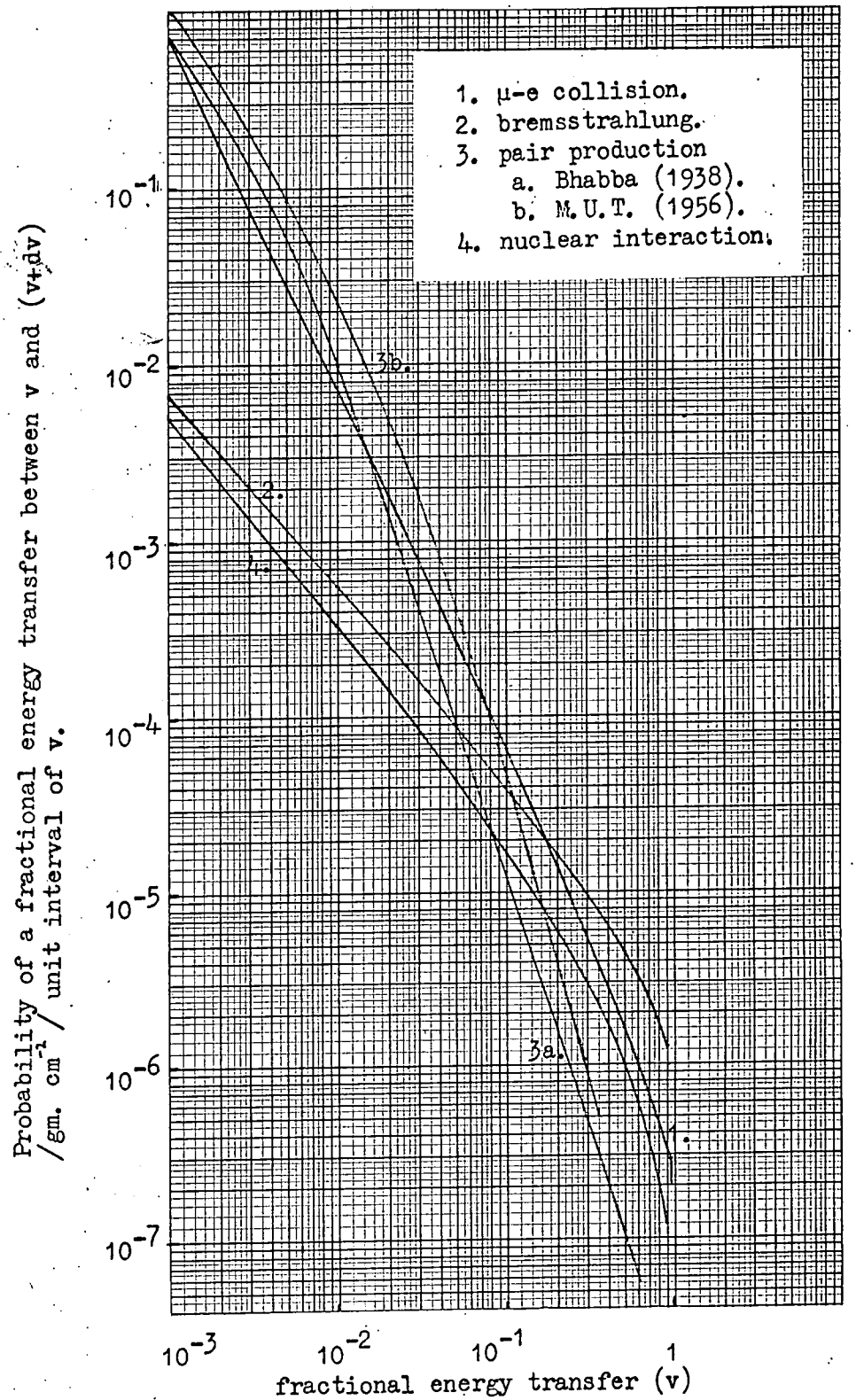

Figure 4.1. Interaction cross-sections for a 100 Gev muon in iron.

transfers > 17 GeV. Hence, to study bremsstrahlung experimentally, it is necessary to detect large energy transfers. The Horizontal Burst Experiment detects large energy transfers in the form of large bursts, which can be attributed mainly to bremsstrahlung, and also smaller bursts (~ 30 particles) which arise mainly from the collision process.

4.2 Comparison with experiment

The results of work done prior to 1958 are contained in a review article by Fowler et al (1958). Up to that time experimental results agreed with prediction for energy transfers ~ 1 GeV. A comprehensive survey of the experimental work since 1958 in the field of electromagnetic interactions has been carried out by Rogers (1965). In the case of the μ - e collision process, Deery et al (1960), using a cloud chamber, found an excess of events with energy transfers in excess of 1 GeV. Backenstoss et al (1963) have made measurements with an absorption spectrometer situated in the muon beam from the CERN proton synchrotron and found no discrepancy for energy transfers in the region 1 - 3.4 GeV; of these two experiments, that of Backenstoss appears to be the more accurate, the quoted error being 5%. It is possible that the discrepancy found by Deery arises from statistical fluctuations, for it has not been substantiated by other experimental evidence. Another experiment which finds agreement with the Bhabba theory for transfers up to 1 GeV is that of Chaudhuri et al (1965),

using a multiplate cloud chamber in the cosmic ray beam. The statistics of this experiment are fairly good, with over 70 events of energy transfer in excess of 350 Mev.

The experimental results with regard to direct pair production are not entirely in agreement with theory. While Roe et al (1959) and Gaebler et al (1961), both using multiplate cloud chambers, find cross-sections which are a factor of 2 lower than those predicted by the M.U.T. theory, for energy transfers in the range 0.2 - 1 GeV, the work of Chaudhuri et al (1964) finds good agreement with the M.U.T. theory for energy transfers in the range 0.035 - 1 GeV. At the present time, there is no conclusive evidence to discriminate between the Bhabba theory and that of M.U.T.

Bremsstrahlung is the one process which seems to be adequately described by theory. The experimental work of McDiarmid et al (1962) found no deviation from prediction over the energy transfer range where radiation losses were important i.e. 10-50 GeV. The large energy transfers which arise mainly from bremsstrahlung can be detected by means of the electron-photon bursts which they produce, and several experiments have been undertaken during the last few years to measure these large bursts.

4.3 Burst experiments

4.3.1 Introduction

The cosmic ray muon spectra in both the vertical and largely inclined directions have been well established by magnetic spectrographs for sea level energies< 500 GeV. Consequently, muons have been used to study large energy transfers in various absorbers, enabling the predictions of quantum electrodynamics to be tested at large energytransfers. At higher muon energies (> 500 GeV), where bremsstrahlung is predominant, measurements have been made on the shape of the cosmic ray spectrum, assuming the correctness of the radiation cross-section. Agreement between the muon spectrum measured in this way and the spectrum obtained from measurements on γ cascades at various depths in the atmosphere establishes the validity of the bremsstrahlung cross-section.

4.3.2 Barton et al (1966)

Barton et al (1966) have studied the electromagnetic interactions of high energy cosmic ray muons at a depth of 60 m.w.e. below sea level, using an apparatus consisting of six liquid scintillation counters, each of area 1.1 m^2, interleaved with sheets of lead of thickness 2.5 radiation lengths. The measured range of energy transfers was 0.1-50 GeV. The number of electrons at shower maximum was used as a measure of the energy of the shower, and the cascade theory of Buja (1963) was employed

to convert from burst size to the corresponding shower energy. This technique has the advantage that fluctuations due to the stochastic nature of showers are a minimum at shower maximum. The results indicate no significant discrepancy between the measured spectrum and the spectrum predicted from theory. The μ - e collision process was dominant for energy transfers in the range 0.1 - 6 GeV with bremsstrahlung more important at larger energy transfers.

4.3.3 Hilton (1967)

A prototype of the University of Utah neutrino detector has been operated to register bursts produced by muons incident in the zenith angle range 60°-90°. The detector consisted essentially of two large water Cerenkov counters on either side of an iron absorber, each having a sensitive area of 30 m^2. The Cerenkov counters were used to determine the number of particles in a burst, and layers of cylindrical spark counters interspaced in the detector determined the trajectory of the muon with an accuracy of less than one degree. Some evidence about the lateral spread of the burst could also be obtained from the spark counter information. The three-dimensional co-ordinates of each spark in the accoustic spark counters, together with the pulse heights from the Cerenkov counters, determined using pulse height analysers, and the time of each event was recorded automatically on magnetic tape. The relevant data, over 1300 events, were

extracted from the total recorded data by means of computer. The minimum burst size considered was 40 electrons. Comparison of the measured data with expectation shows a discrepancy, there being fewer large bursts than predicted. This deviation can be accounted for by postulating that the theoretical bremsstrahlung cross-section is in error for large energy transfers (> 50 GeV).

4.3.4 Higashi et al (1964)

The cascade showers produced by high energy muons in the earth have been measured at a depth of 20 m.w.e. underground by means of scintillation counters of total area $8m^2$. The apparatus consisted of four scintillators (each of area $2m^2$), and two neon flash-tube arrays positioned under the counters. With this arrangement the authors claim it was possible to observe bursts due to muons from all incident directions. The neon flash-tube arrays were used to distinguish bursts produced by muons with small angles of incidence ($< 60^\circ$) from those bursts produced by more oblique muons.

Three processes were considered as contributing to the production of bursts : bremsstrahlung, μ - e collision and direct pair production. Bremsstrahlung was predominant, and the case of no screening was assumed in the theoretical analysis. Fluctuations were taken into account by the Furry distribution. Uncertainty in the effective aperture of the apparatus leads to some ambiguity in the method of determining the limitation

of zenith angle, and the possibility of bursts produced by muons at zenith angles around 70^{o} could not be excluded. The theory of Barrett et al (1952) was used to predict the vertical muon spectrum from the measured data. The resulting form of the vertical spectrum was :

$$F_{\gamma}(>E) = 3.8 \begin{smallmatrix} +0.3 \\ -1.3 \end{smallmatrix} \quad (E/10^{3})^{-\gamma} \qquad cm^{-2}sec^{-1}sterad^{-1}$$

with $\gamma = 2.5 \begin{smallmatrix} +1.0 \\ -0.3 \end{smallmatrix}$ for $10^{3} < E < 4 \times 10^{3}$ GeV.

A modification to the apparatus has been made by increasing the counter area to 20 m^{2} and incorporating a second layer of scintillators (area 20 m^{2}) at a distance of 2m. below the original layer. Making use of the variation in response of 20 photomultipliers with position of the shower axis over the area, it is possible to establish the position of the burst in each layer, and hence the zenith angle of the incident muon. The measured burst spectrum has been converted to an incident vertical muon spectrum using cascade theory, and the resulting spectrum (private communication to Professor A. W. Wolfendale) is shown in figure 4.2. There is good agreement with the O.P.W. spectrum for muon energies up to 2000 GeV but above this energy the O.P.W. spectrum predicts less muons than are measured. The best value of the exponent as determined from the burst experiment is $\gamma = 2.7 \pm 0.2$ for muons of energy up to 10^{4} GeV.

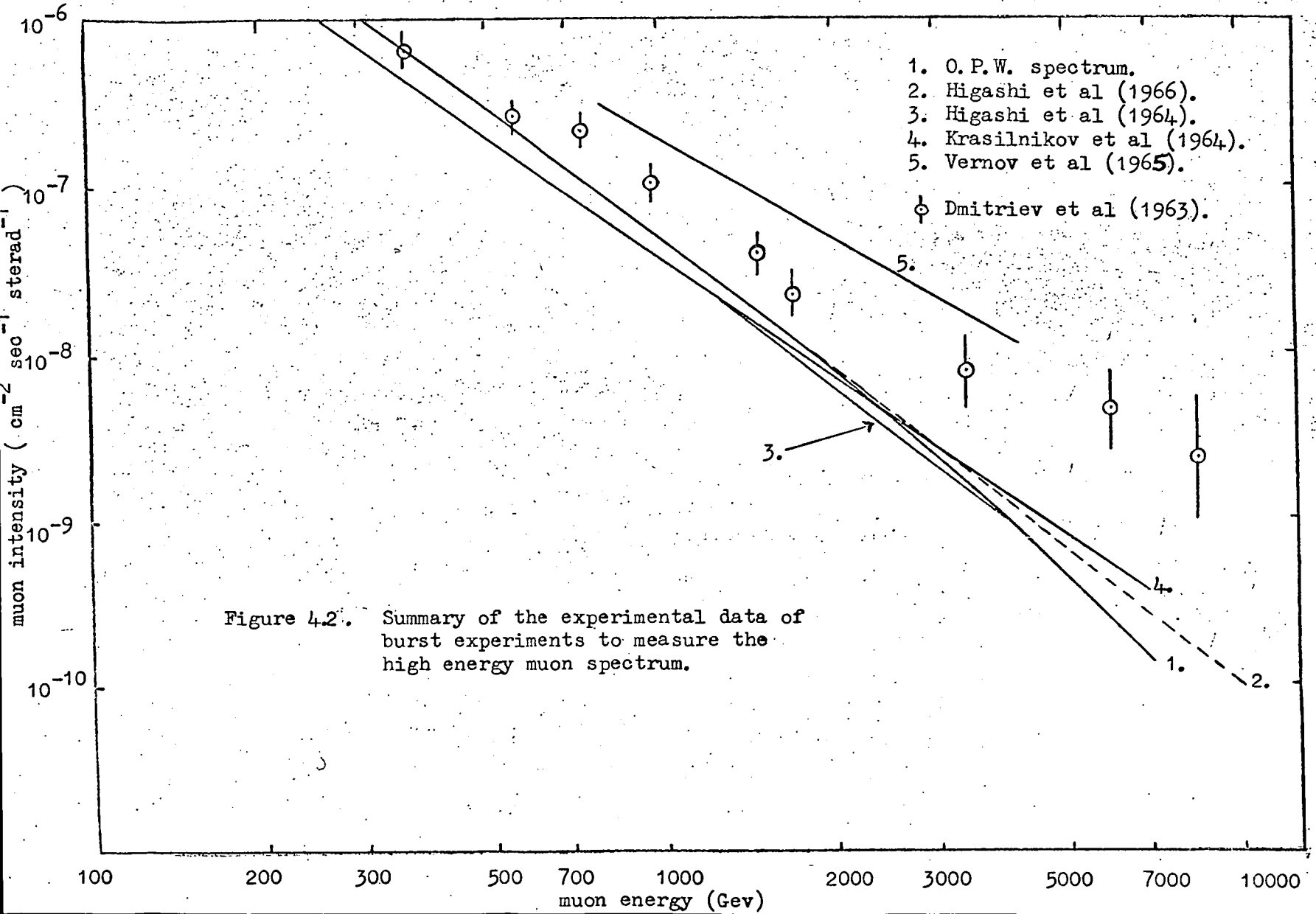

Figure 4.2. Summary of the experimental data of burst experiments to measure the high energy muon spectrum.

4.3.5. Krasilnikov (1965)

Large ionisation bursts produced in a thickness of 10.5 cms of lead were measured in spherical ionisation chambers by Krasilnikov (1965). The fraction of bursts caused by residual nuclear active components and by extensive air showers was estimated from altitude dependence and from consideration of the barometer effect. The effect of fluctuations was not taken into consideration. Bursts detected by the apparatus are produced by an omnidirectional flux over a solid angle of nearly 2π steradians. The incident muon spectrum in the vertical direction has been derived from the measured burst spectrum and is given by

$$F(>E) = (1.0 \pm 0.14) \times 10^{-5} \ (E/10^{11})^{-\gamma} \ cm^{-2}.sec^{-1}.sterad^{-1}.$$

where $\gamma = 2.4 \pm 0.1$ for $10^{11} < E < 6 \times 10^{12}$ ev.

The spectrum is shown in figure 4.2. The results of both Krasilnikov and Higashi et al. (1964) give values of the exponent which are smaller than the O.P.W. spectrum. However, the later measurements of Higashi et al. (1966) are more in agreement with the O.P.W. spectrum.

4.3.6. Dmitriev et al. (1963)

The energy spectrum of muons in the range 100 - 3000 GeV was derived by Dmitriev et al. (1963) from the spectrum of large bursts produced under a lead filter at a depth of 40 m.w.e. underground.

Basically the apparatus consisted of ionisation chambers (sensitive area 1.75 m^2) screened on top of a layer of lead 16 cms thick. Below the chambers geiger counters were installed so that muons travelling with zenith angle $\theta \leq 50^\circ$ could be selected.

The measured spectrum of bursts was converted to the incident vertical muon spectrum using the cascade curves of Ott (1954) and the theory of Barrett et al. (1952). Allowance was made for different track lengths in the chambers and for the angular distribution of particles in a burst, and fluctuations were accounted for by means of a Monte-Carlo method. The integral muon spectrum is shown in figure 4.2, and is found to have an exponent $\gamma = 2.1 \pm 0.2$ in the muon energy range 100 - 3000 GeV. There is a very marked discrepancy between these results and the others displayed in figure 4.2., especially in the energy region > 1000 GeV.

4.3.7. Vernov et al. (1965)

An investigation of the penetrating component of cosmic rays has been carried out at a depth of 40 m.w.e. underground by Vernov et al. (1965). The apparatus consisted of 240 ionisation chambers and 200 geiger counters, presenting a total sensitive area of 45 m^2. A multi-tray detector (area 5m^2), consisting of 5 trays of geiger counters and three trays of ionisation chambers, was incorporated in the array. The burst size in each chamber was

recorded individually in one channel of a pulse height analyser, and the direction of the trajectory of a charged particle passing through the counter trays was measured with the aid of the multi-tray detector. The spectrum of bursts produced by penetrating particles traversing the array with zenith angle $\theta < 45^{\circ}$ was measured. This has been converted into the vertical muon spectrum, which is displayed in figure 4.2. Again there is a considerable discrepancy, both in absolute value and in exponent, between this spectrum and the O.P.W. spectrum.

4.3.8. Borog et al. (1965)

Cascade showers were studied by Borog et al. (1965) using an ionisation calorimeter. The apparatus consisted of six rows of rectangular ionisation chambers placed between layers of iron 9 cms thick. With this arrangement it was possible to measure the total number of ionising particles at six levels in the cascade curve and also to determine the angle of incidence of the primary particle. Over 1400 showers were recorded in a running time of 2520 hours. Measurement of the angular distribution of showers established that for $\theta \geq 55^{\circ}$-60° the fraction of showers initiated by nuclear-active particles was negligible compared with muon bursts. The exponent of the burst spectrum measured in the angular range 55°-90° was $\gamma = 2.15 \pm 0.15$. Using a linear conversion factor to determine the average muon energy producing a given energy transfer, the authors derived the integral muon

spectrum in the zenith angle range 55^{o}-90^{o} :

$$I = (10^{-5})\, E^{-\gamma} \qquad cm^{-2}.\ sec^{-1}\ sterad^{-1}$$

with $\gamma = 2.15 \pm 0.15$ and E in units of 10" ev.

This spectrum, which is valid in the energy range 300 - 3000 GeV, is plotted in figure 3.2.

4.3.9. Discussion

The burst experiments of Barton and Hilton were performed to test quantum electrodynamics in the region of large energy transfers. Barton studied bursts produced by vertical cosmic ray particles in a region where μ-e collisions were predominant, and found agreement with theory. Hilton, on the other hand, detected bursts produced by muons incident at large zenith angles, and comparison of the observed spectrum with prediction showed a discrepancy for energy transfers > 50 GeV. It seems unlikely that this discrepancy could arise from either fluctuations or from errors in the incident muon spectrum. The measurements indicate an over-estimation in the theoretical bremsstrahlung cross-section - a result which is not substantiated by the work described in this thesis.

The remaining burst experiments are concerned with determining the incident muon spectra, assuming the validity of Q.E.D. The results of Higashi et al. (1966) are largely in agreement with Krasilnikov and the O.P.W. spectrum, any disparity between the respective experiments being due to the uncertainties inherent in the experimental technique. The measurements of both Dmitriev

and Vernov give rise to spectra which have smaller exponents than the O.P.W. spectrum. However, it should be remembered that these two spectra are 'global' spectra, whereas the O.P.W. spectrum refers to vertical muons. Finally the measurements of Borog et al. in largely inclined directions are not in agreement with the Ashton et al. (1966) measurements, as shown in figure 3.2. It should be noted that the measurements refer to the total angular range 55°-90°, whereas the Ashton data are measured in a much narrower angular range. The conflicting evidence produced by measurements of the muon spectra by means of burst techniques underlines some of the difficulties inherent in the method.

4.4. Conclusions

The cross-sections for knock-on electron production, bremsstrahlung and direct pair production used in the burst calculations are those given by Rossi (1952). Both the knock-on and bremsstrahlung processes are adequately described by theory, the former for energy transfers $\leq$ 15 GeV and the latter for transfers $\leq$ 50 GeV. At the present time the experimental results with regard to direct pair production are in conflict. However, in the Horizontal Burst Experiment the dominant processes are μ-e collision and bremsstrahlung, and the contribution to bursts from direct pair production is small. Hence the predicted burst spectrum is fairly insensitive to the cross-section employed to describe direct pair production.

CHAPTER 5

CASCADE SHOWERS IN IRON

5.1. Introduction

Electrons lose energy by collision and by the radiation process in traversing matter, and for energies greater than the critical energy of the medium (ϵ_o) radiation losses predominate. On passing through the Coulomb field of the nucleus, there is a definite probability that an electron will emit a photon by bremsstrahlung, the energy of which is close to that of the initial electron. A photon of such energy can either materialize into an electron-positron pair or can undergo Compton scattering. In either case the resulting charged particles can emit further photons, which in turn produce more electrons. Hence, at a certain depth in the medium, instead of there being one electron of energy E_o, there are several electrons and photons whose total energy is close to E_o. As the cascade process continues, the average energy of the electrons decreases until eventually collision losses dominate bremsstrahlung, and the shower dies out, all the initial energy being dissipated in excitation and ionisation of atoms.

Over the last thirty years many workers have attempted to explain theoretically the behaviour of an electron-photon cascade in matter. The approaches can be divided into two categories:

1. The analytical method, in which a set of diffusion equations

are formulated to represent the cascade, and solutions are obtained under varying simplifying conditions.

2. The Monte-Carlo method, in which the primary particle and all subsequent particles are followed through the material, and the fate of each is determined by a 'wheel of chance'.

5.2 Analytical method

5.2.1. Simplifying assumptions

Mathematically, it is very difficult to predict the probability of an electron or photon incident on an absorber producing N_e electrons and N_γ photons at a depth t in the solid angle range $(\omega,\omega+d\omega)$, in the energy range $(E,E+dE)$ and at a distance $(r,r+dr)$ from the shower axis. Consequently, only the average behaviour of showers is calculated, and any specific probability is calculated as a deviation from the average behaviour.

The angles of emission of secondary electrons and photons are very small, of magnitude $m_e c^2/E_o$, where E_o is the energy of the primary particle. In substances of low atomic number Rutherford scattering is also small, so that the shower essentially develops in the direction of the incident particle. However, in high Z absorbers cascade multiplication continues to lower secondary electron energies where multiple scattering becomes important. In general the approach adopted is to treat the cascade as being one-dimensional and then to make corrections for the increased track length due to scattering.

5.2.2. Basic equations

The equations of the one-dimensional cascade theory, which includes pair production and Compton scattering by photons and bremsstrahlung and ionisation losses by electrons, are derived in detail by Rossi (1952) by considering the various production and absorption processes taking place in an infinitesimal layer of thickness dt. The expressions $\pi(E,t)\,dE$ and $\gamma(E,t)dE$ are the numbers of electrons and photons respectively with energies between E and (E + dE) at a thickness t. The diffusion equations relating the numbers of electrons and photons at depth t to the numbers of electrons and photons at depth (t + dt) are:

$$\frac{\partial \pi(E,t)}{\partial t} = \int_E^\infty \gamma(E',\, t)\, \phi_p\,(E,E')dE' + \int_E^\infty \pi\,(E',t)\, \phi_E\,(E',E'-E)dE'$$

$$- \int_0^E \pi\,(E,t)\, \phi_E(E,E')dE' - \beta\, \frac{\partial \pi(E,t)}{\partial E}$$

$$\frac{\partial \gamma(E,t)}{\partial t} = \int_E^\infty \pi(E',t)\, \phi_E(E',E)dE' - \int_0^E \gamma\,(E,t)\, \phi_p\,(E,E')dE'.$$

where β is the average ionisation loss per radiation length

$\phi_E(E,E')$ is the differential probability per radiation length for the production of a photon (energy E′) by an electron (energy E).

$\phi_p(E,E')$ is the differential probability per radiation length for the production of an electron (energy E) by a photon (energy E′). This can occur by either pair production or Compton scattering.

5.2.3. Solutions of the basic equations

Detailed solutions of the diffusion equations under the assumptions of Approximations A and B are given by Rossi (1952). Compton scattering and collision losses are ignored in the simpler Approximation A approach, and the probabilities for pair production and radiation are described by their asymptotic values. Similar simplifications are made under Approximation B, but with the exception that collision losses are taken into account by subtracting an amount of energy equal to the critical energy per radiation length from each of the electrons in the cascade.

A survey of the cascade theory of electron-photon showers by Belenkii et al. (1959) gives a comprehensive account of the various methods and the different approximations adopted by several workers in their attempts to solve the diffusion equations. Using the method of functional transformations, a fairly complete description of the average one-dimensional cascade in light substances can be obtained. However, this method is not valid in light materials when the electron energies are $\sim \epsilon_0$, or in heavy substances where scattering is important. A further difficulty in high Z substances is that the total absorption coefficient for photons is strongly energy dependent. In Approximation B this coefficient is constant and equal to the asymptotic value of the pair production cross-section. For this reason, the method of functional transformations, whose usefulness is due to the application of asymptotic expressions for the cross-sections of the basic processes, does not give an accurate picture of

shower development in heavy substances, especially in the tail of the shower, where the absorption of photons of energy ~ ϵ_o has a value smaller than the asymptotic value.

Another approach which has been used extensively in solving the problem makes use of the fact that the function can be defined by its moments. This method of moments has been applied to heavy absorbers by Belenkii et al. (1959).

5.2.4. Cascades in iron

Bursts corresponding to mean energy transfers in the range 2×10^9 - 3×10^{11} ev have been observed in the Horizontal Burst Experiment. Hence any cascade theory employed in a theoretical analysis must cover this particular energy range and also pertain to iron. Ivanenko et al. (1958) have calculated cascade curves in copper for primary electron or photon energies in the range 3.2×10^8 - 1.3×10^{12} ev by means of the method of moments, taking into account the energy dependence of the total photon absorption coefficient, and multiple scattering. These curves, which may be applied to iron due to the Z of copper being only ~10% different from that of iron, are the only ones available at the present time which satisfy the experimental criteria, and so have been employed to calculate theoretical burst spectra in S_1 and S_2.

Shower development curves of Ivanenko are shown in figure 5.1 for showers initiated in iron by primary electrons of

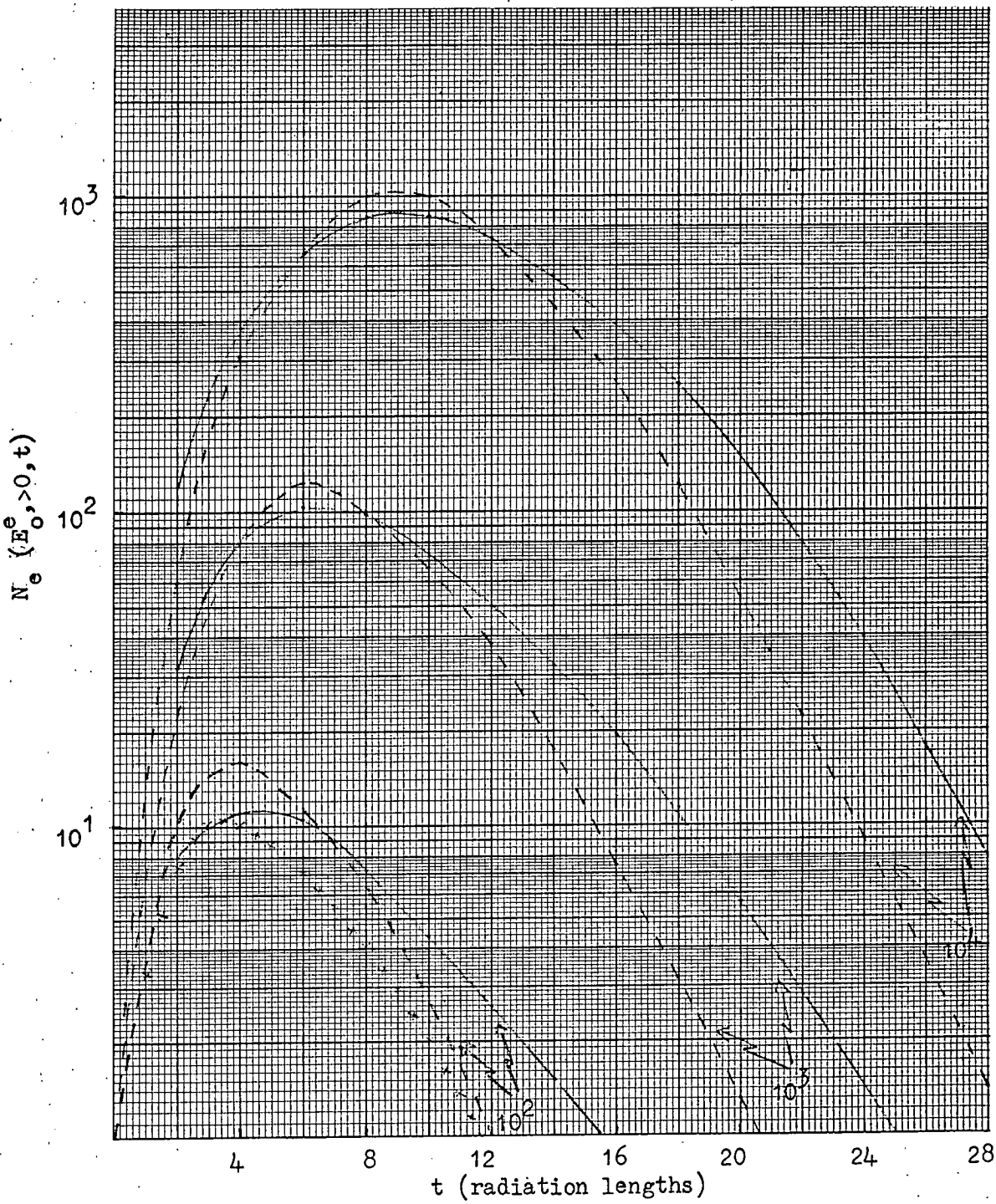

Figure 5.1. Comparison of shower development curves of Ivanenko et al (1958) (full lines) and Approximation B (broken lines) for showers initiated in iron by primary electrons of energies $E_o/\epsilon_o = 10^2, 10^3$ and 10^4. The curve ××××× represents the Monte-Carlo calculations of Crawford et al (1965) and is for an energy $E_o/\epsilon_o = 9.5 \times 10$

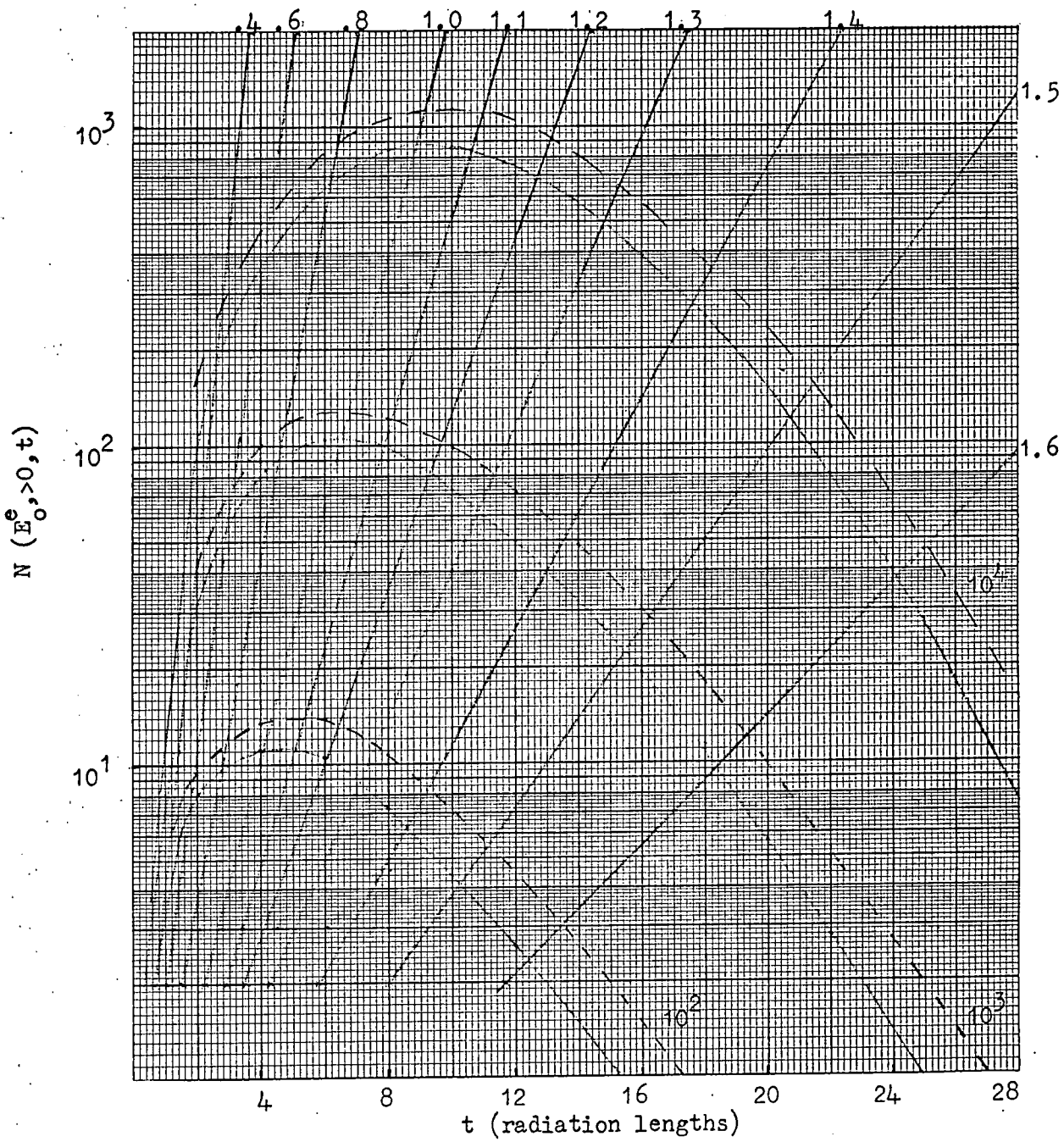

Figure 5.2. Shower development curves giving the numbers of electrons (full lines) and photons (broken lines) for cascades initiated in iron by primary electrons of energies $E/\epsilon = 10^2, 10^3$ and 10^4. The full lines are according to Ivanenko et al (1958), and the broken lines have been interpolated from Approx. A. the straight lines are the loci of constant age parameter s.

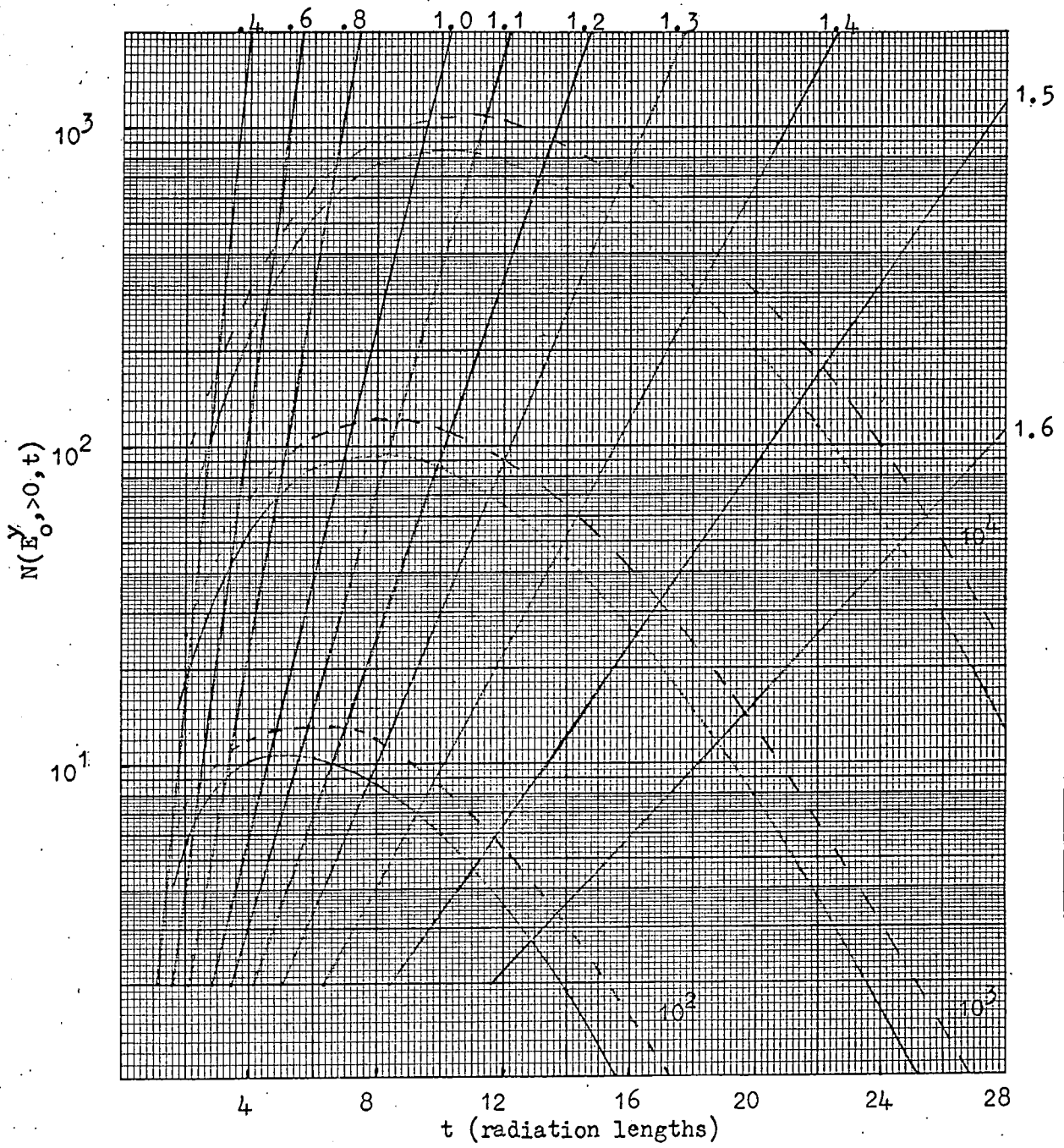

Figure 5.3. Shower development curves giving the numbers of electrons (full lines) and photons (broken lines) for cascades initiated in iron by photons of energies $E_o/\epsilon_o = 10^2, 10^3$ and 10^4. The full lines are according to Ivanenko et al (1958), and the broken lines have been interpolated from Approx. A. The straight lines are the loci of the age parameter s.

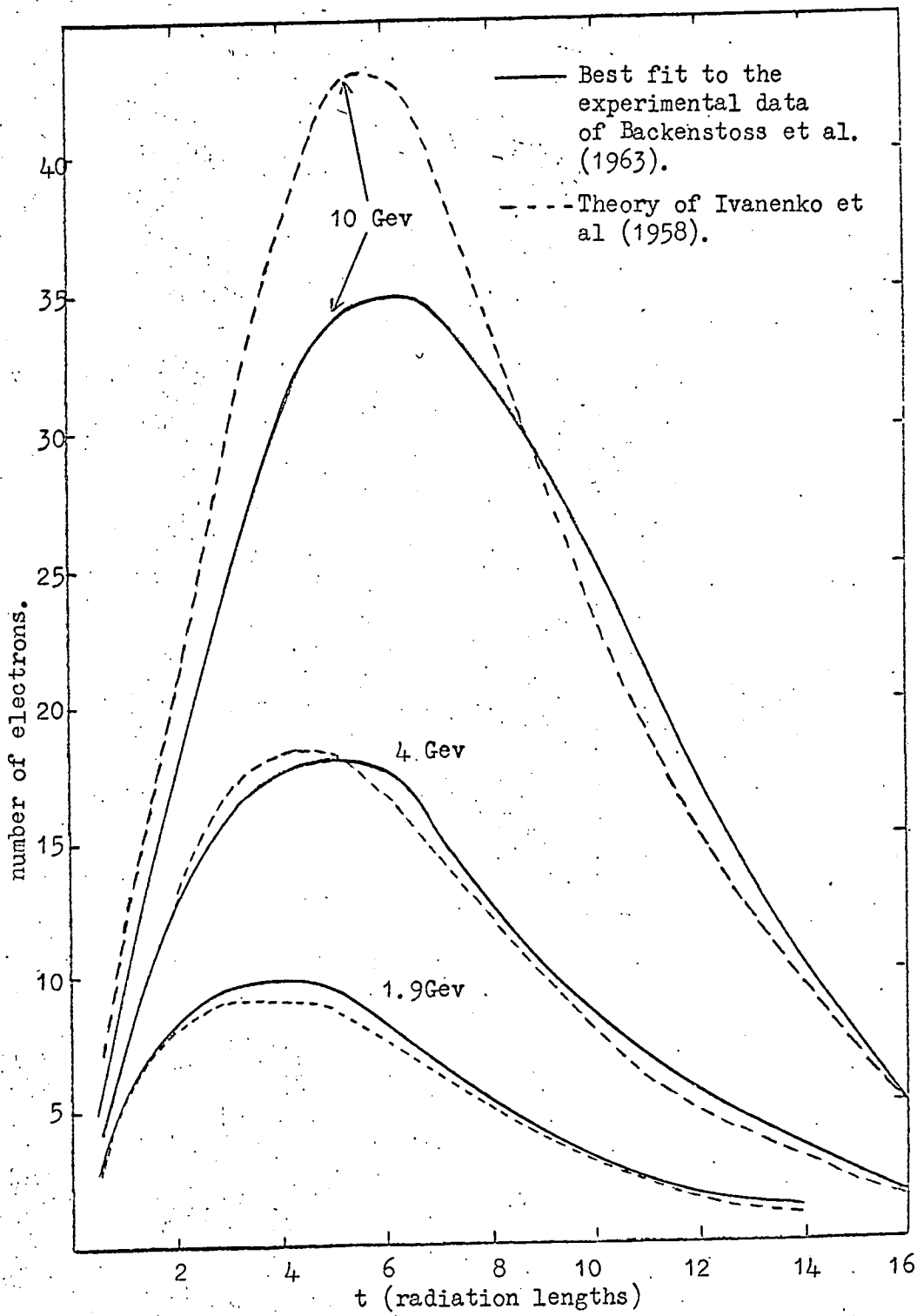

Figure 5.4. Experimental data of Backenstoss et al for iron compared with the theory of Ivanenko et al.

energies E_o given by $E_o/\epsilon_o = 10^2$, 10^3 and 10^4. ϵ_o = 21 Mev for iron. The curves indicate the total number of electrons at any depth. Comparison is made in the same figure with curves calculated under Approximation B. The divergence after shower maximum is due to the use of asymptotic values in Approximation B. Cascade curves for electron and photon initiated showers are displayed in figures 5.2 and 5.3 respectively. The full lines represent the total number of electrons, and the broken lines refer to the total photon flux. The latter have been interpolated from Approximation A. The loci of constant age parameter s as given by Approximation B are also displayed in the figures.

5.3. Comparison with experiment

5.3.1. Backenstoss et al. (1963)

Cascade showers produced in a total absorption spectrometer by a beam of muons from the CERN proton synchrotron have been studied by Backenstoss et al. (1963). Average showers in iron resulting from knock-on electron production were obtained for energies up to 10 GeV, and these are shown in figure 5.4 together with the theoretical predictions of Ivanenko. There is good agreement between theory and experiment for showers of energy $\leq$ 4 GeV, but at 10 GeV the theory predicts ~ 20% more electrons at shower maximum than are actually observed.

5.3.2. Takbaev et al. (1965)

Electron-photon showers have been recorded in iron by Takbaev et al. (1965) using an ionisation calorimeter consisting of 12 layers of chambers separated by absorber. Showers initiated by nuclear-active particles were rejected by means of a large carbon plate (160 gm. cm^{-2}) and two layers of ionisation chambers beneath the main calorimeter. Pions produced in the interaction of a nuclear-active particle would be expected to produce a further shower beneath the carbon, whereas electromagnetic cascades would be absorbed. A total of 187 electromagnetic showers were observed. The energy of each cascade was determined using the relation

$$E_o = \beta \int_0^\infty N_o(t)\, dt$$

where β is the average energy loss of an electron per gm.cm^{-2}. It was found that the primary energies were in the range 100 - 300 GeV. The showers were normalised to an energy of 100 GeV, and the average curve is shown in figure 5.5. The experimental points are in good agreement with the theoretical curves of Ivanenko.

5.3.3. Murzin et al. (1963)

The shape of electron-photon cascade curves in iron has been measured with an ionisation calorimeter by Murzin et al. (1963) for primary electron and photon energies ~ 200 GeV. The The calorimeter consisted of six layers of ionisation chambers

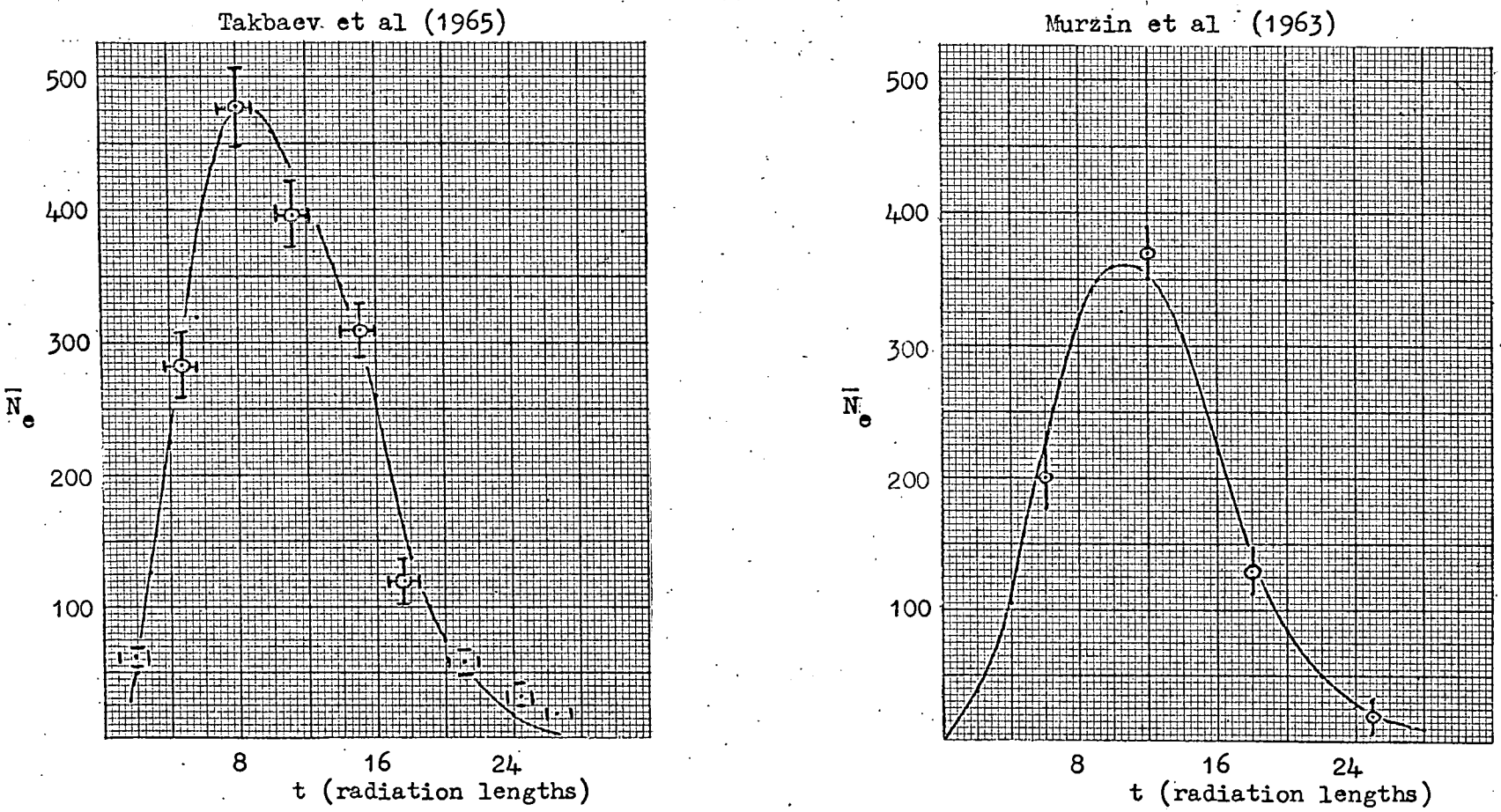

Figure 5.5. Comparison of the experimental results of Takbaev et al (1965) and Murzin et al (1963) with the theory of Ivanenko et al (1958).

interleaved with iron, and only events in which there were at least 250 relativistic charged particles in each of three layers were selected.

In general, interactions of nuclear-active particles lead to a broader depth distribution of ionisation in the calorimeter, often possessing several peaks. Consequently, the basis for selecting electromagnetic bursts was an ionisation distribution of minimum width, one peak and commencing within the first three radiation lengths of the absorber. To avoid selecting events arising from several primary electrons and photons, only cases were considered in which 75% of the ionisation produced in one row occurred in a single ionisation detector.

Using these selection criteria, 10 out of 80 recorded events were interpreted as being electromagnetic cascades. These events were normalised to a primary energy of 100 GeV, and are shown in figure 5.5 together with the theoretical curve of Ivanenko. Despite the limited statistical accuract of the measurements, the agreement with theory is good.

It should be noted that the absolute numbers of electrons measured by Takbaev et al. and Murzin et al. are not in agreement, despite both measurements being normalised to an energy of 100 GeV.

5.4. Monte-Carlo calculations

The Monte-Carlo method of simulating electron-photon cascades has been used by Crawford et al. (1965) to study the three-dimensional cascade problem in copper for various primary and secondary energies. They have produced extensive tables of electron and photon number distributions, together with radial and angular distributions. In these calculations bremsstrahlung, pair production, Compton scattering, multiple scattering and ionisation losses were taken into account. The Bethe-Heitler cross-sections for pair production and bremsstrahlung were used, with allowances made for the screening effect. Any deflections as a result of these processes was considered negligible compared with multiple scattering.

The results of Crawford et al. are restricted with regard to primary energy, and the tables available for copper were for a maximum energy of 2 GeV. Hence, it is only possible to compare Ivanenko et al and Crawford et al at this energy. A difficulty in making a comparison arises from the fact that Ivanenko et al. calculate the total number of electrons whereas Crawford et al. present the results in the form of the flux of electrons with energy in excess of 10 MeV. In the burst experiment calculations it is important to know the energy spectrum of electrons in a cascade, so as to be able to calculate the equivalent burst size measured by a scintillator.

5.5. Energy spectrum of electrons in a burst

A scintillation counter measures the total track length of ionising particles in the phosphor. Because the phosphor has a finite thickness, a particle requires a definite energy to traverse the counter, and particles with energy less than this minimum value will be stopped in the phosphor. In particular the mean minimum energy for the scintillators used in the burst experiments was 28 MeV. An equivalent particle is defined as a particle which completely traverses the counter. Hence two electrons each of energy 14 MeV incident on the phosphor would be detected as one equivalent particle by the scintillator. Consequently, it is necessary to know the energy spectrum of electrons in a cascade so as to establish a relationship between the number of equivalent particles measured by the scintillator and the true number of electrons in the burst.

The integral energy spectrum of electrons in a cascade as calculated under Approximation B is proportional to $(E + \epsilon_o)^{-S}$, where S is the age parameter. Mitra et al. (1949) measured the momentum spectrum of particles in extensive air showers at sea level using a counter-controlled cloud chamber operated in a magnetic field, and found the results to be consistent with an integral spectrum proportional to $(E + \epsilon_o)^{-\gamma}$ with $\gamma = 1.1 \pm 0.3$. According to the authors the theoretical value of the exponent is 1.5 but the discrepancy was due to selection bias and scattering of the particles.

In figure 5.6 the energy distribution of electrons at the maximum of a 2 GeV cascade initiated by a primary electron in iron is shown by the full line, and has been calculated from the cascade curves of Ivanenko et al using the expression

$$N(>E) = N(>o) \quad (1 + E/\epsilon_o)^{-S}$$

Nassar et al (1946) attempted to check the validity of shower theory using a counter controlled cloud chamber operated in a magnetic field of 1100 gauss. The chamber contained four lead plates, and events were selected in which cascades initiated by a single electron were observed in the chamber. The average energy distribution of electrons near the maximum was determined using 17 showers with a maximum number of particles between 6 and 20. The experimental points are plotted in figure 5.6, and are normalised to the Ivanenko et al curve at an electron energy E given by $E/\epsilon_o = 0.45$, having been corrected so as to apply to an iron absorber.

Also displayed in the same diagram is the energy distribution predicted by Richards et al (1948), normalised at the point $E/\epsilon_o = 0.5$. This has been derived using precise expressions for the probabilities of Compton effect, radiation and pair production. The production of secondary electrons by collision processes was also considered. The assumption was made in the computation that the equation representing loss and gain of particles by radiation can be described by a continuous energy loss; this procedure is

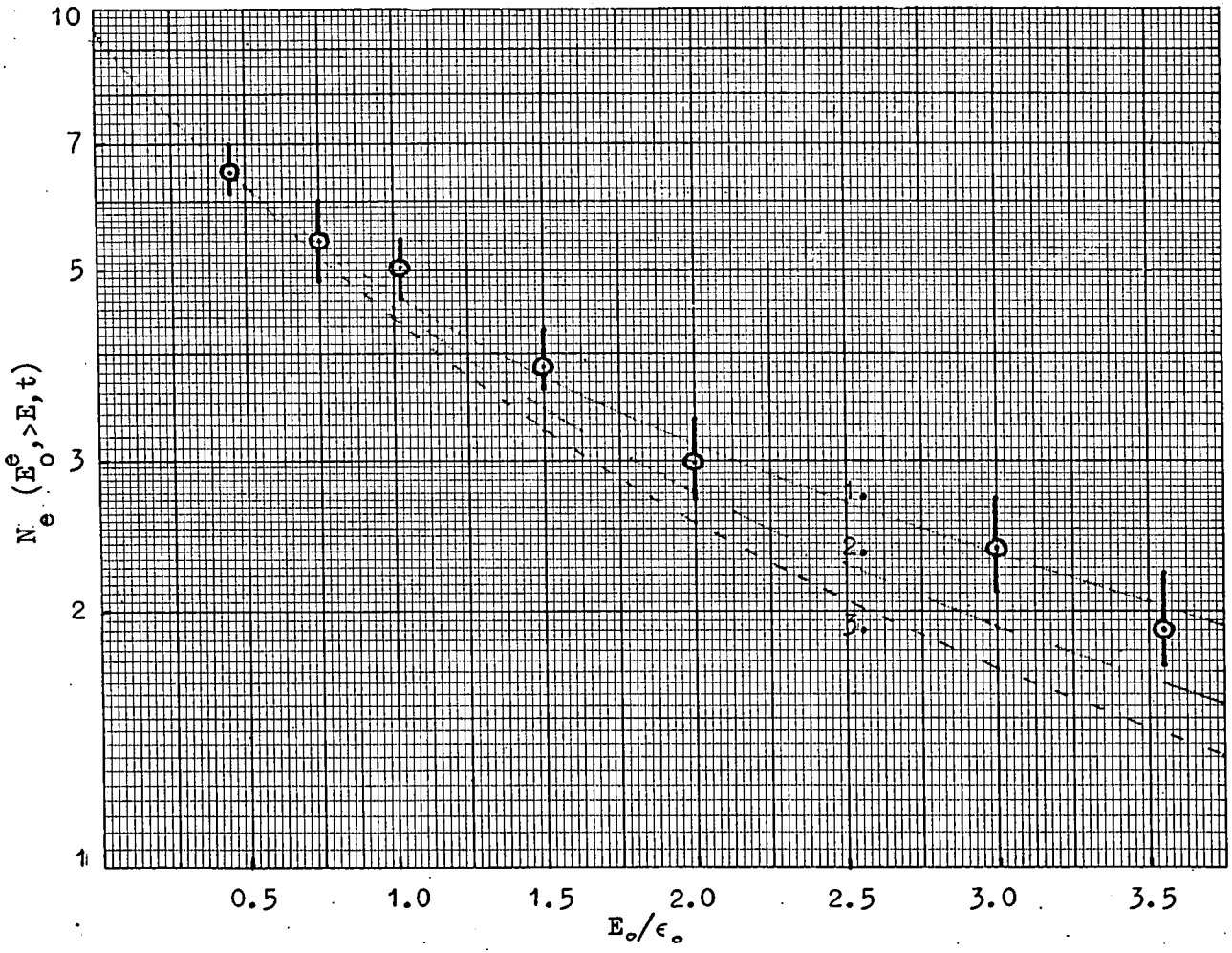

Figure 5.6. Energy distribution of electrons at shower maximum in a 2 Gev cascade initiated in iron by a primary electron.

1. prediction of Ivanenko using the expression $N(>E)=N(>0)/(1+E/\epsilon_0)^s$.
2. Richards et al (1948).
3. Crawford et al (1965).

⊙ Nassar et al (1946).

valid for electron energies $E \ll E_o$, where E_o is the primary energy.

The energy distribution of electrons at the maximum of a 2 GeV cascade as determined by Crawford et al is displayed in figure 5.6, and is normalised to Ivanenko et al at $E/\epsilon_o = 0.5$. Both Crawford et al and Richards et al predict fewer electrons of a given energy than does the $(E + \epsilon_o)^{-S}$ variation, which is in agreement with the experimental data of Nassar et al. The data of Crawford et al for the energy distribution of electrons in 1 GeV and 2 GeV cascades in copper is best fitted by

$$N(>E) = N(>0) \; / \; (1 + E/\epsilon_o)^p \quad \text{with } p = 1.5S - 0.2.$$

This expression has been used to determine the total number of electrons in a 2 GeV cascade as predicted by Crawford et al, and this is displayed in figure 5.1. There is a considerable discrepancy between Crawford et al and Ivanenko et al with regard to the absolute number of electrons.

5.6. Photon contribution to a burst

A simple model has been adopted. Ivanenko et al do not evaluate photon cascade curves for either primary photons or electrons. Hence, photon curves have been interpolated from Approximation A, and these are shown in figures 5.2 and 5.3, for primary electrons and photons respectively.

Bursts are composed of both photons and electrons. A scintillator measures the total track length of ionising particles in the phosphor, so that the burst size as recorded by the counter will comprise the track length of electrons entering the phosphor from the iron, together with a contribution from electrons produced by photon interactions in the phosphor. There are two important processes by which photons interact to produce electrons:

1) Pair production

The differential probabilities per radiation length for pair production given by Rossi (1952) are:

for $m_e c^2 \ll E \ll 137\, m_e c^2\, Z^{-\frac{1}{3}}$

$$\mu(E) = \left(\frac{7}{9} \ln \frac{2E}{m_e c^2} - \frac{109}{54}\right) / \ln (183\, Z^{-\frac{1}{3}})$$

and for $E \gg 137\, m_e c^2\, Z^{-\frac{1}{3}}$

$$\mu(E) = \frac{7}{9} - 1 \Big/ \left((54 \ln (183\, Z^{-\frac{1}{3}})\right)$$

The expressions have been interpolated in the intermediate energy region.

2) Compton scattering

The probability for a photon of energy E traversing a thickness dx gm.cm^{-2} to undergo a Compton collision in which the scattered photon has an energy between E′ and (E′ + dE′) is given by Rossi (1952) as:

for $E \gg m_e c^2$ and $\frac{1}{2} m_e c^2 < E' < E$

$$\phi\,(E,E')dE'\,dx = 0.15\,\frac{Z^2}{A}\,m_e c^2\,\frac{dE'}{E'}\,\frac{1}{E}\left\{1+\left(\frac{E}{E}\right)^2\right\}dx$$

The total track length of electrons produced in the phosphor by photons has been evaluated using the above cross-sections, and assuming the energy spectrum of photons to be the same as that of electrons. The contribution by photons to a given burst size is 24%.

At high electron and photon energies the ratio of photons to electrons in a burst is 9/7, but at ~~larger~~ lower energies photons become more abundant due to the reduced photon absorption coefficient. The total track length distribution of photons in iron has been interpolated from the data evaluated for air and lead by Richards et al, and using these figures the contribution by photons to a given burst size is 37%. The difference principally arises from the increased flux of low energy photons undergoing Compton scattering. However, any underestimation to the contribution by the adoption of the simple approach will apply to all burst sizes, and so will affect only the absolute magnitude of the predicted burst spectrum and not its shape.

5.7. Conclusions

The theory of Ivanenko et al is, in general, in good agreement with the available experimental measurements for iron. The energy spectrum of electrons in a cascade is best described by the expression

$$N(>E) = N(>0) \;/\; (1 + E/\epsilon_o)^S$$

where ϵ_o is the critical energy of the absorber, and S the age parameter.

5.8. Fluctuations

5.8.1. Distributions

So far only the average behaviour of cascade showers has been considered. It is a much more complicated problem to compute the distribution function giving the probability of obtaining more than N particles at a depth t, taking into account the fluctuation problem, due to the difficulty in solving the resulting complex integro-differential equations. Hence attempts have been made to derive this distribution function from general considerations or from simplified models.

The Poisson distribution was the first to be tried, on the basis of genetic independence of the shower particles. This assumption depends on the number being large for its validity. However, the Poisson formula underestimates the effect of fluctuations due to the genetic dependence of the particles - any deviation from the average behaviour occurring early in the development of the cascade reflects at greater depths.

A more promising approach was made by Furry (1937) who obtained a distribution as a solution of a differential equation based on the actual mechanism of the shower. However, ionisation losses were ignored in the derivation of the distribution, and electrons

and photons were treated as identical particles. In a cascade the effect of ionisation losses becomes important at large depths, so that the Furry distribution might be expected to apply over the first few cascade lengths.

The experimental mean square deviation from the average is too large to fit a Poisson distribution and too small to fit a Furry distribution, so it would appear that a distribution whose mean square deviation lies between these two extremes would be appropriate. The Polya´ is such a distribution. Its shape depends on a parameter b, and it reduces to the Poisson and Furry limits when b = 0 and 1 respectively. The probability $P(N,\bar{N})$ of obtaining a number N if the mean is $\bar{N}$, according to the Polya´ distribution, is given by:

$$P(N,\bar{N}) = \frac{1}{N!}\left(\frac{\bar{N}}{1+b\bar{N}}\right)^{N}(1 \times (1+b)\ldots.(1+(N-1)b))(1+b\bar{N})^{-1/b}$$

where $0 \leq b \leq 1$. The distribution for various values of b is shown in figure 5.7 for $\bar{N} = 20$. The Poisson distribution is fairly symmetrical about the mean value, but for values of $b > 0$, the distributions become skew towards smaller values of N.

5.8.2 Effect on a spectrum

The theory of cosmic ray bursts played an important part in the determination of the spin of the muon. Christy et al. (1941) found the theoretical size-frequency distributions of large bursts produced by bremsstrahlung of high energy muons were

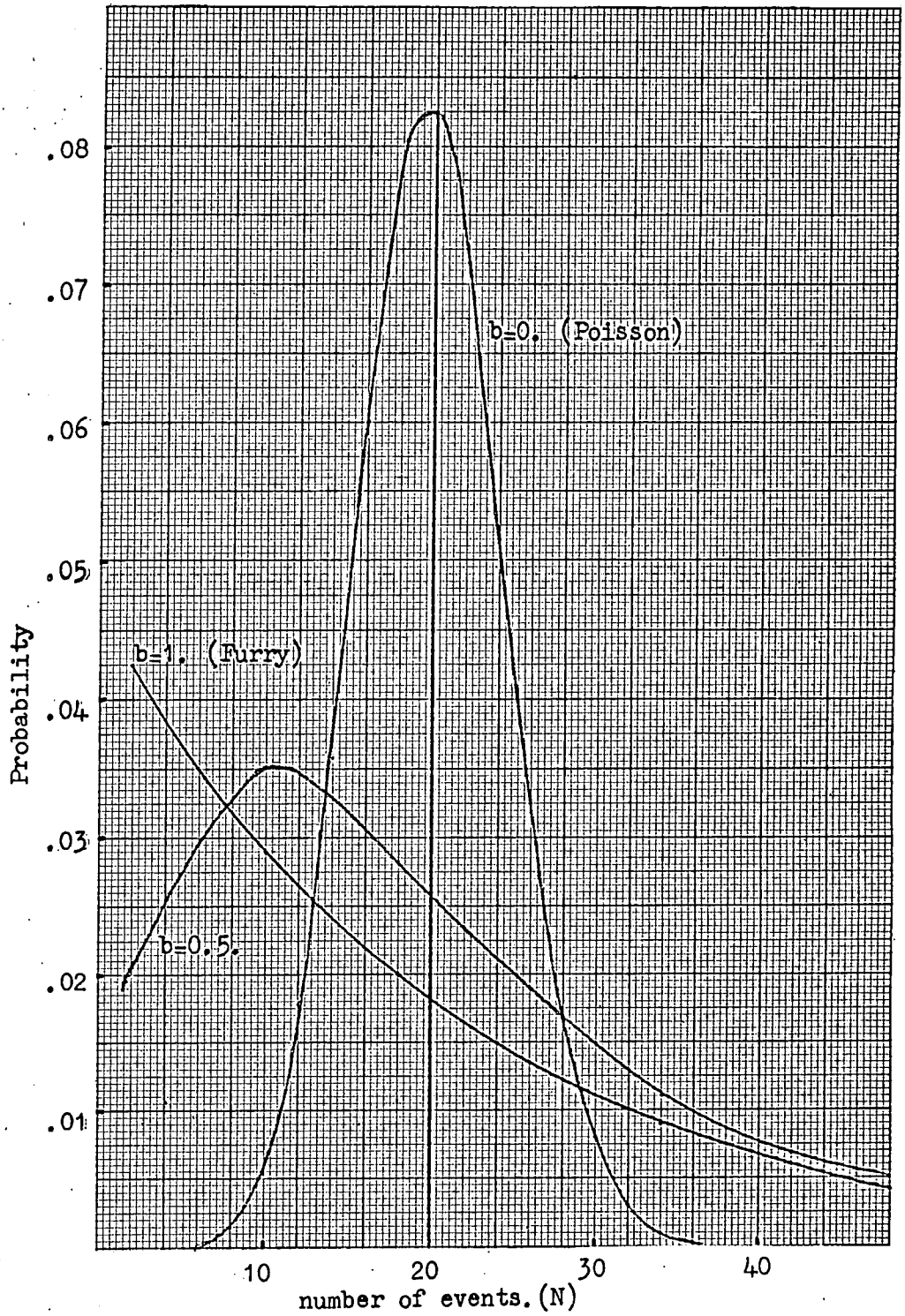

Figure 5.7. Polyá distribution for various values of b. The mean number is $\bar{N}=20$.

sensitive to the muon spin. From a comparison of their theoretical burst spectra with experimental measurements, they concluded that muons were Dirac particles of spin $\frac{1}{2}$. Mitra (1957) has applied fluctuation distributions to the theoretical spectra of Christy et al to show that fluctuations have a considerable effect on burst size. He concludes that the effect of fluctuations would be to obscure any conclusion that might be made about the muon spin. In particular, Mitra compares his results with the experimental measurements, and concludes the best value of b in the Polya´ distribution is 0.87, indicating a distribution very close to that of Furry.

It is important to know the effect of fluctuations on the theoretical burst spectra in S_1 and S_2, derived from 'average' cascade theory. Hence, fluctuation corrections have been applied to the predicted S_1 spectrum of bursts according to the two extreme cases - Poisson and Furry. The Poisson distribution alters the curve little, but the effect of the latter distribution is to change the absolute rate at any given burst size. However, the exponent of the new spectrum is essentially unaltered, over the range of burst sizes relevant to the Durham burst experiments.

5.8.3. Experimental data

Takbaev et al. (1965) have examined the distribution of charged particles in cascades produced in iron by means of an

ionisation calorimeter (§ 5.3.2). The experimental distributions were measured as a function of depth in the absorber, and the following conclusions were drawn:

1. At small thicknesses ($t < 2$ radn. lengths) the distribution approximates to Furry.
2. At large thicknesses ($t > 17$) the distribution approximates to Poisson.
3. Near shower maximum ($8 < t < 11$) the distribution is Normal.

The above results refer to showers of energy ~ 100 GeV.

The data of Crawford et al. (1965) also shows the same form as observed by Takbaev et al, being a minimum at shower maximum and becoming larger for small and large depths in the shower. Both these results are in agreement with the calculations of Gerasimova (1965). Near the beginning of the shower, there are a few highly energetic particles, so that fluctuations are significant for the development of the shower. These fluctuations, particularly for photon induced showers, are close to Furry. Near shower maximum, the fluctuations are smaller due to the larger number of particles present.

CHAPTER 6

ANALYSIS OF RESULTS

6.1. Introduction

The procedure adopted to interpret the measured bursts has been to predict burst spectra for S_1 and S_2 assuming the validity of Q.E.D. Comparison between the measured and predicted spectra then indicates the accuracy of the cross-sections. The predominant process contributing to small bursts is that of knock-on electron production, whereas large bursts arise mainly through bremsstrahlung. Hence, any discrepancy would reflect on either of these two processes.

6.2. Experimental analysis

Bursts produced in the apparatus (figure 2.1) are detected by a pulse from the geiger tray G_2 (figure 2.1), a large pulse from either S_1 or S_2, and no pulse from s'. When the selection criteria were satisfied, the size of the scintillator pulse was recorded photographically on an oscilloscope, and the flash tube trays photographed by a second camera. For a discriminator setting of > 100 particles in either S_1 or S_2, the ratio of useful events to the total number of exposures was 1:4.

For each burst the projected zenith angle of the muon was determined from the flashes in A and B, and the burst size in either S_1 or S_2 (defined as the recorded pulse height divided by

the mean pulse height produced by a single relativistic muon traversing the counter at normal incidence to its largest face). Also recorded for each event were the mean numbers of flashes, $\overline{N}_c$, $\overline{N}_d$ and $\overline{N}_e$ in the flash tube trays C, D and E respectively.

Figure 6.1 shows typical bursts produced by an energy transfer in F_1. In both cases the muon penetrates F_2 and is recorded by tray E. Interactions occurring in F_2 are displayed in figure 6.2. The muon track is clearly visible in trays A, B, C and D, together with a burst in E. Double bursts probably produced by the cascade from a large energy transfer in F_1 penetrating the second absorber are displayed in figure 6.3. In both cases the burst size in S_2 was not recorded. A double burst event, probably caused by two independent muon interactions, one in F_1 and the second in F_2, is shown in figure 6.4a. The possibility of employing events of this nature to determine the high energy muon spectrum ($E\mu > 500$ GeV) is discussed in Chapter 7. Figure 6.4b is probably a nuclear interaction of a muon, the transverse momenta of the produced pions accounting for the double core nature. However, the low number of flashes in tray E is not typical of a pion cascade. The fiducials and clock have been omitted from all these photographs for the sake of clarity.

6.3. Theoretical burst spectra

6.3.1 Incident muon spectrum

Functions for the differential aperture of a detector of

a.

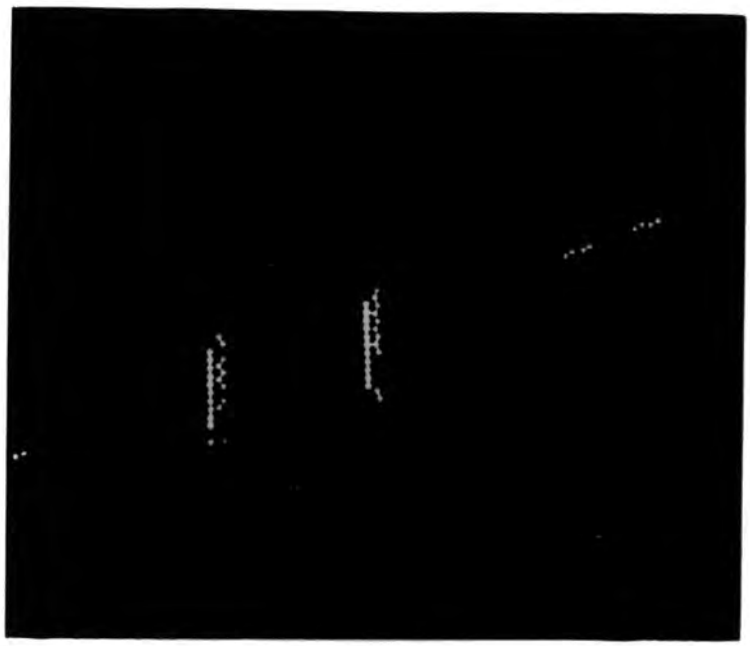

b.

Figure 6.1. Typical bursts in S_1.

a. $\theta=73^{\circ}$. $N_s=56$ particles.

b. $\theta=78.5^{\circ}$. $N_s=16$ particles.

a.

b.

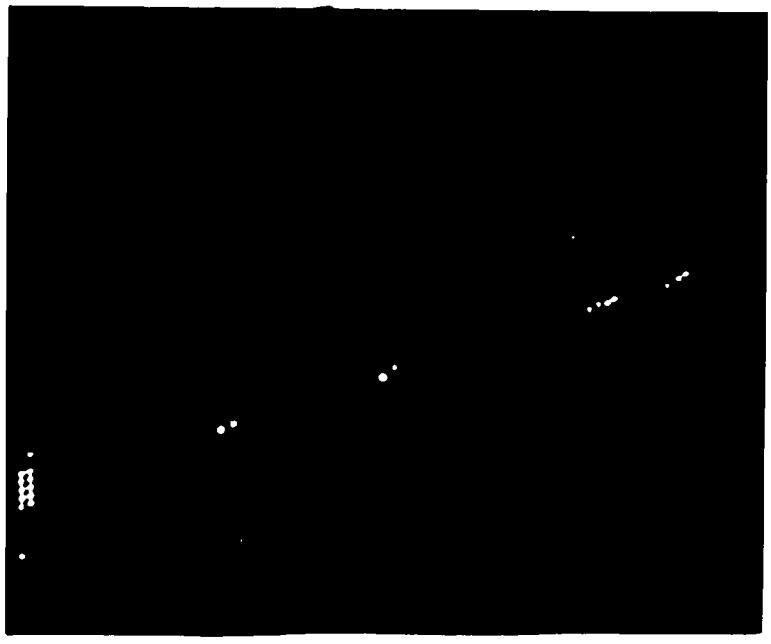

Figure 6.2. Typical bursts in S_2.

a. $\theta = 70.5^{\circ}$. $N_s > 280$ particles.

b. $\theta = 73^{\circ}$. $N_s = 26$ particles.

a.

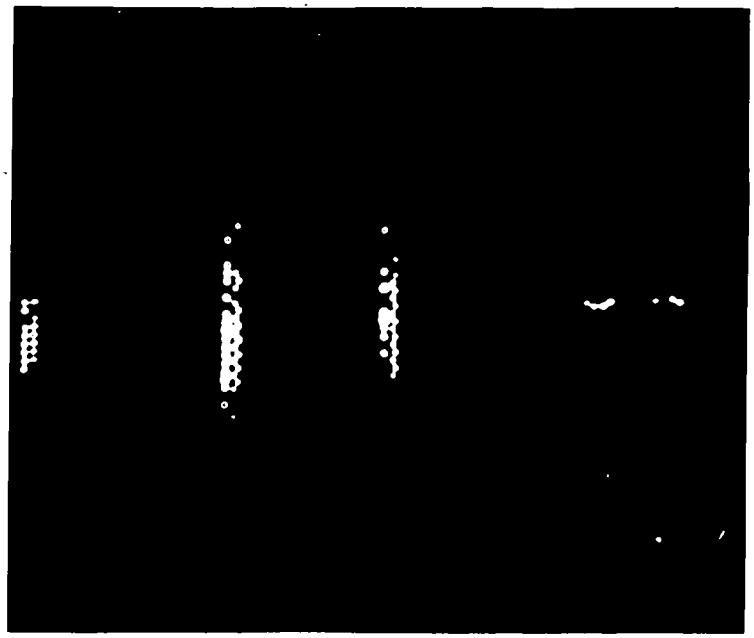

b.

Figure 6.3. Double bursts.

a. $\theta=88^{\circ}$. $N_{S1}=510$ particles.
b. $\theta=77^{\circ}$. $N_{S1}=44$ particles.

} N_{S2} not recorded.

a.

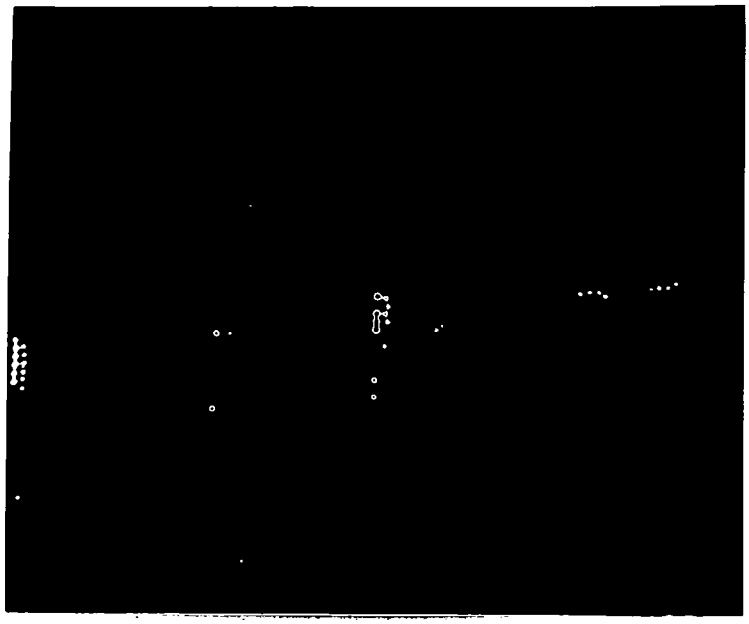

b.

Figure 6.4. Unusual events.

a. Double interaction - one in F_1 and a second in F_2. $N_{S1}=38$ particles; N_{S2} not recorded.

b. Double core event - probably a nuclear interaction of a muon.

rectangular dimensions X, Y and Z have been calculated by Osborne (1966) for muons incident on the XY face :

for $\frac{\pi}{2} \geq \theta \geq \cot^{-1}\left(Y/(X^2 + Z^2)^{\frac{1}{2}}\right)$

$$\frac{d\Omega}{d\theta} = 2\left(\sin^2\theta\left[Y(X^2+Z^2)^{\frac{1}{2}} - YZ\right] - \sin\theta\cos\theta\left[XZ\tan^{-1}\frac{X}{Z} - Z^2\ln\left((X^2+Z^2)^{\frac{1}{2}}/Z\right)\right]\right)$$

and for $\cot^{-1}\left(Y/(X^2 + Z^2)^{\frac{1}{2}}\right) > \theta \geq \tan^{-1}\frac{Z}{Y}$

$$\frac{d\Omega}{d\theta} = 2\sin\theta\left(XY\left(\sin^2\theta - \frac{Z^2}{Y^2}\cos^2\theta\right)^{\frac{1}{2}} - YZ\sin\theta + \cos\theta\left[Z^2\left(1-\ln\frac{Z}{Y}\right) - XZ\cos^{-1}\left(\frac{Z}{Y}\cot\theta\right) - Z^2\ln\cot\theta\right]\right).$$

The muon spectrum summarised in Table 3.1 has been used in conjunction with the above acceptance functions to derive the spectrum of muons traversing the array. The axis of the apparatus was orientated at an angle 8° east of magnetic north, and only particles incident from the north were accepted, due to a hill on the south side of the laboratory attenuating the muon flux from this direction. Corrections to the differential aperture for dead space between the geiger counters in G_2 have been included. Considering S_1 alone, muons of energy $\leq$ 100 GeV come predominantly from the zenith angle range 50°-77.5°, whereas larger energy muons mainly arrive at larger zenith angles. The median zenith angle increases from $\theta = 66.5^\circ$ for muons of energy 10 GeV to $\theta = 81^\circ$ for muons of energy 1000 GeV. For muons traversing S_2 the values of the median zenith angles are larger than thosefor S_1, due to the cut-off being 63° instead of 50° as in S_1.

6.3.2 Electromagnetic cascades

The three electromagnetic processes by which a muon can lose energy are bremsstrahlung, μ-e collision and direct pair production, and these have been considered in Chapter 4. The spectra of energy transfers in F_1 and F_2 were evaluated using the incident muon spectrum and the known cross-sections for the interaction processes. As no information about the azimuth of the incident muon is available from the experiment, muons were assumed to be incident at the mean azimuth of the apparatus and corrections were applied to the energy transfer spectra for the increase in target thickness.

The theory of Ivanenko et al, which was shown in Chapter 5 to be in good agreement with the available experimental evidence, has been adopted in order to derive a burst spectrum from the energy transfer spectrum. The energy spectrum of electrons in a burst is taken to be $N(>E) \propto (1 + E/\epsilon_o)^{-S}$. Integrating the energy distribution of electrons over the thickness of the phosphor shows that the equivalent number of particles as measured by the scintillator is represented by the number of electrons in a shower with energy > 15 MeV. Standard cascade curves in terms of the equivalent burst size are shown in figure 6.5 for electron and photon initiated showers, and include a 24% contribution by photons interacting in the phosphor.

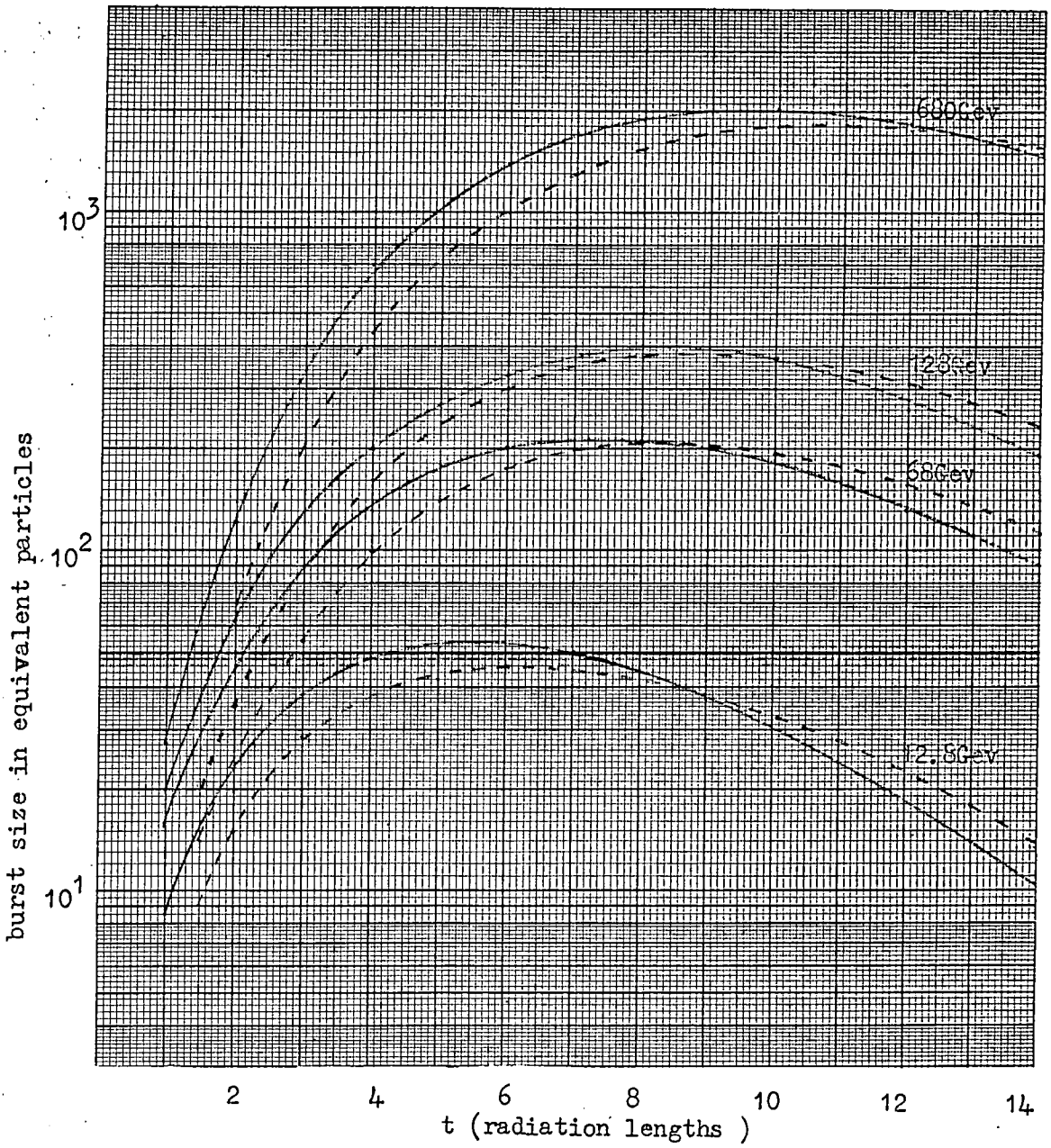

Figure 6.5. Shower development curves for cascades initiated by primary electrons (full lines) and primary photons (broken lines) of energy E_o. The burst size is in terms of equivalent numbers of particles recorded by a scintillator, and includes a 24% contribution from photon interactions in the phosphor.

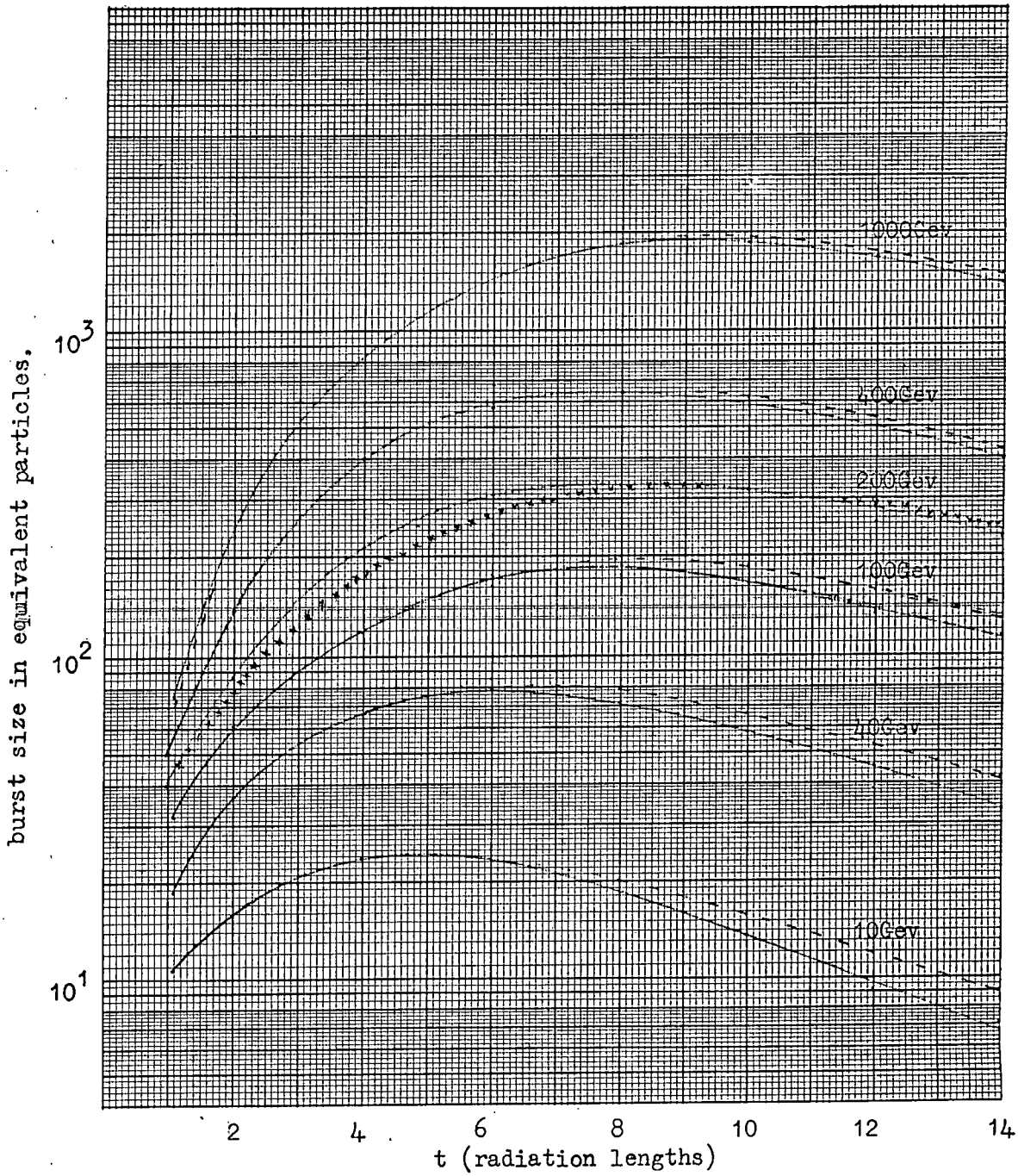

Figure 6.6. Cascade curves for nuclear interactions of muons. The full lines are calculated using the pion inelasticities of Brooke et al (1964a). The broken lines are calculated assuming pion interactions to be 100% inelastic. The figures against each curve denote the cascade energy in Gev. The curve ×××××××× is taken from the data of Denisov et al (1965) and refers to an energy of 200Gev.

6.3.3. Pion cascades

It has been known since the work of George et al. (1950) that there is a significant cross-section for the inelastic collision with a nucleus. The interaction is regarded as being between a photon of the virtual photon cloud accompanying the muon, and the nucleus. The cross-section for the interaction is then derived from a knowledge of the flux of virtual photons, and the measured cross-section for the interaction of real photons.

The probability of a muon of total energy U transferring a fraction between v and (v + dv) is given by

$$\phi(U,v) = \frac{N}{A} \cdot Z \cdot \frac{\alpha}{\pi} \cdot \sigma_{h\nu} \cdot \frac{dv}{v} \ln\left(\frac{1}{v}\right)$$

where $\sigma_{h\nu}$ is the photonuclear cross-section.

When a nuclear interaction occurs, the resulting pions cascade in the iron. Neutral pions decay rapidly into two γs, which then give rise to an electromagnetic cascade. Charged pions penetrate the iron and interact again to produce further pions, both charged and neutral. Hence, the cascade is a composite one, consisting of electron-photon showers originating at various depths in the absorber from the decay of neutral pions, together with a flux of charged pions. The inelastic cross-sections for π-p and p-p interactions have been given by Morrison (1963) as 22 mb and 30 mb respectively. The resulting cross-sections for pion and proton interactions with an iron nucleus are 631 mb and 715 mb respectively, so that the respective mean free paths for

pions and protons in iron are 19.3 cms and 17 cms.

In the calculations it was assumed that the total multiplicity of pions produced in γ-N collisions is given by $n_s = 3E_\gamma^{\frac{1}{4}}$, with E_γ in GeV. Equipartition of energy among the produced pions is assumed, and in the subsequent pion cascade the inelasticity of π-N collisions has been taken from Brooke et al (1964c). A total multiplicity of secondary pions, $n_s = 3E_\pi^{\frac{1}{4}}$, with E_π in GeV has been used.

Assume a γ-N interaction occurs after a muon has traversed a distance (X - x) of the iron (thickness X), and let the pion interaction length be λ. Then a fraction $\exp(-x/\lambda)$ of the produced charged pions will leave the iron without further interaction, and the remainder will, on average, interact after travelling a distance $\bar{x}$ given by

$$\bar{x} = \lambda - x \,/\, (\exp(\tfrac{x}{\lambda}) - 1).$$

Pion cascades for various primary energies and different points of origin have been followed through the iron. The contribution to the total by the electromagnetic cascade has been evaluated using the curves in figure 6.5. It was assumed that charged pions with energy < 1 GeV lose all their energy by nuclear disintegration. The resulting cascade curves are shown in figure 6.6. Also displayed in the same figure are the curves for a pion inelasticity of 100%. The difference between the curves at depths relevant to the burst experiment is small, indicating a weak

dependence of the cascade development on this parameter.

The characteristic features of nuclear cascades produced in iron by primary nucleons have been studied by Denisov et al. (1965) using Monte-Carlo methods. The results for a 200 GeV cascade, corrected so as to take into account the photon contribution, are shown in figure 6.6, together with the corresponding curve calculated by the method described in the previous paragraph. The agreement is good for $t > 7$ radiation lengths, but over the first few radiation lengths there is a discrepancy, being typically $\sim 17\%$ at $t = 4$ radiation lengths. It should be noted that the results of Denisov et al assume a nucleon inelasticity of 75%.

6.3.4 Burst spectra

The burst spectrum produced by energy transfers occurring in a thin layer, dx, has been evaluated from the spectrum of energy transfers and from cascade theory, taking into account the increased track length of electrons in the phosphor due to the incident muon arriving at angles other than normal incidence. The total burst spectrum was obtained by integrating over the whole thickness of the absorber, and may be represented by:

$$b(>n) = \sum_{\text{all pr.}} \int_0^x dx \int_{E_{MIN}}^{\infty} dE_\mu \int_{\theta_{MIN}}^{\pi/2} d\theta \int_{E_{MIN}}^{\infty} \omega_{\text{pr.}}[E_\mu, E] 1(>n, E, x) \phi(E_\mu, \theta) A(\theta\phi) dE$$

where $\phi(E_\mu,\theta)\, d\theta\, dE_\mu$ is the number of muons with energy between E_μ and $(E_\mu + dE_\mu)$ in the zenith angle range θ to $(\theta + d\theta)$.

$\omega_{pr}(E_\mu,E)$ is the probability of a muon of energy E_μ producing an energy transfer E for each process (pr.).

$1(>n,E,x)$ is the probability of there being more than n equivalent particles at a distance x from the position of an energy transfer E.

E_{MIN} is the minimum energy transfer to produce a burst size n.

$A(\theta\phi)$ is the acceptance function of the apparatus.

The spectra of burst arising from the different energy transfer processes have been evaluated for S_1 and S_2, and are displayed in figures 6.7 and 6.8 respectively. Bursts detected in S_2 can be produced by energy transfers occurring in either F_1 or F_2. However, they predominantly are the result of interactions taking place in F_2, the contribution from F_1 being 3% for bursts > 10 particles and 8.5% for bursts > 100 particles.

The relative contribution of each process to the total burst spectrum can be seen in figures 6.7 and 6.8. μ-e collision is the dominant energy loss process for both S_1 and S_2 for burst sizes less than ~ 30 particles, but for larger bursts, bremsstrahlung becomes the major process. The remaining processes do not contribute significantly to the total.

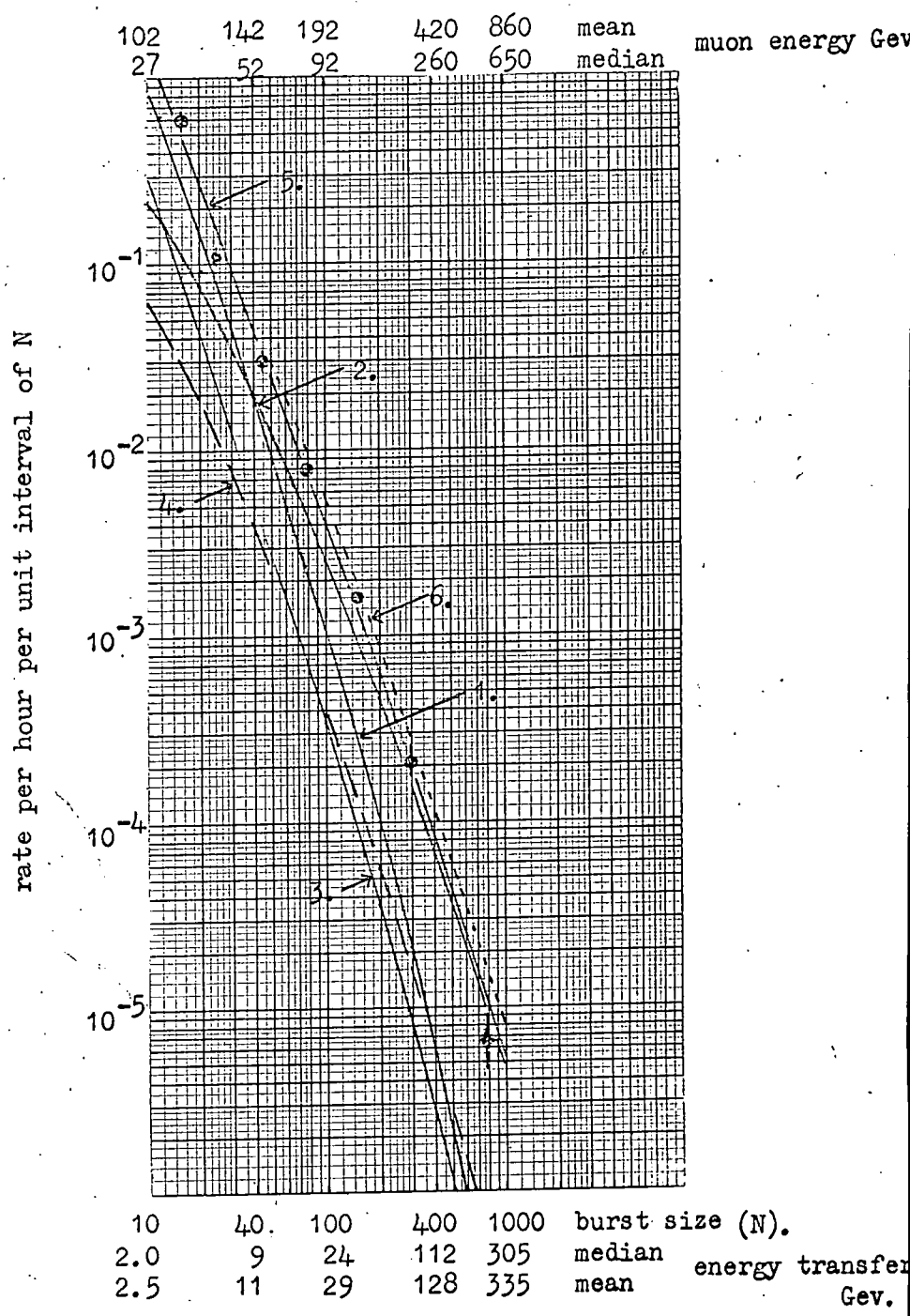

Figure 6.7. The measured burst spectrum in S_1 and comparison with expectation.
1. μ-e collision.
2. bremsstrahlung.
3. direct pair production
4. nuclear interaction ($\sigma_{h\nu}$=constant= 2.6×10^{-28} cm^2/nucleon).
5. total.
6. total if $\sigma_{h\nu}$ varies as $\frac{1}{E^2}$.

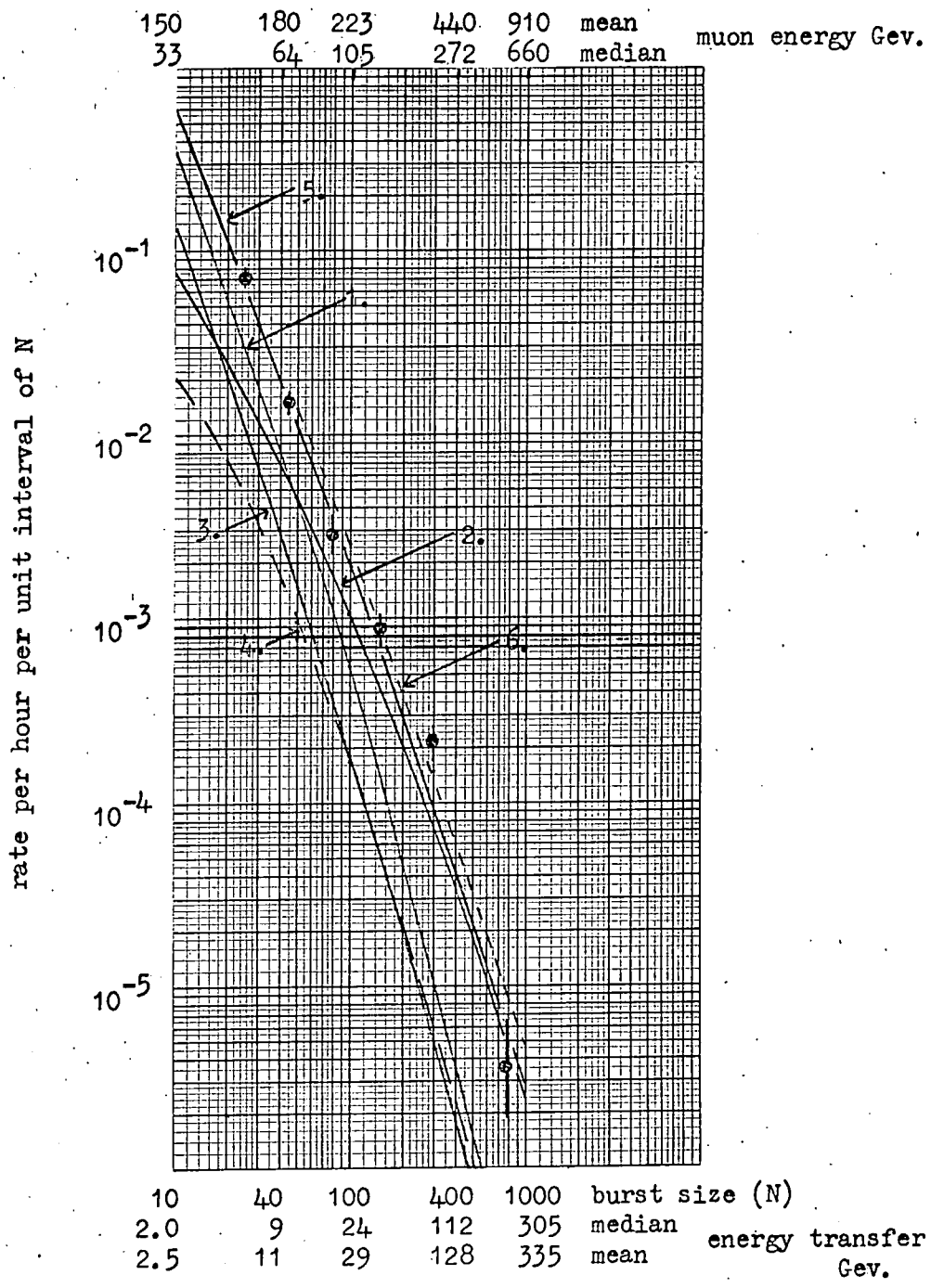

Figure 6.8. The measured burst spectrum in S_2 and comparison with expectation.

1. μ-e collision.
2. bremsstrahlung.
3. direct pair production.
4. nuclear interaction (σ_h =constant= 2.6×10^{-28} cm^2/nucleon).
5. total.
6. total if σ_h varies as $E^{\frac{1}{2}}$.

It was suggested by Matano et al. (1965) that the photonuclear cross-section should depend on energy as $E^{\frac{1}{2}}$, for $E > 5$ GeV. The expected spectra of bursts in S_1 and S_2 have been calculated assuming

$$\sigma_{hr}(E) = (E/5)^{\frac{1}{2}} \sigma_{hr}(5) \quad \text{for } E \geq 5 \text{ GeV}$$

$$\text{and} \quad \sigma_{hr}(E) = \sigma_{hr}(5) \quad \text{for } E < 5 \text{ GeV}$$

where $\sigma_{hr}(5) = 2.6 \times 10^{-28}$ cm^2/nucleon,

and are shown in figures 6.7 and 6.8 by the broken lines. There is a significant contribution to the total spectrum, as is indicated by the difference between the new spectrum and the spectrum calculated on the basis of a constant photonuclear cross-section (2.6×10^{-28} cm^2/nucleon).

The probability of a muon of energy E_μ producing a burst size between n and (n + dn) is a composite function of the muon spectrum, interaction cross-sections and cascade theory. Distributions of muon energies producing bursts in the range 13.2-26.4 particles have been evaluated for S_1, and are shown in figure 6.9. Similar distributions for bursts of size 132 - 264 particles are displayed in figure 6.10. The mean and median muon energies giving rise to the particular burst size by the different interaction processes are indicated, as are the relative contributions of each process to the total burst spectrum.

Small bursts arise principally from low energy transfers

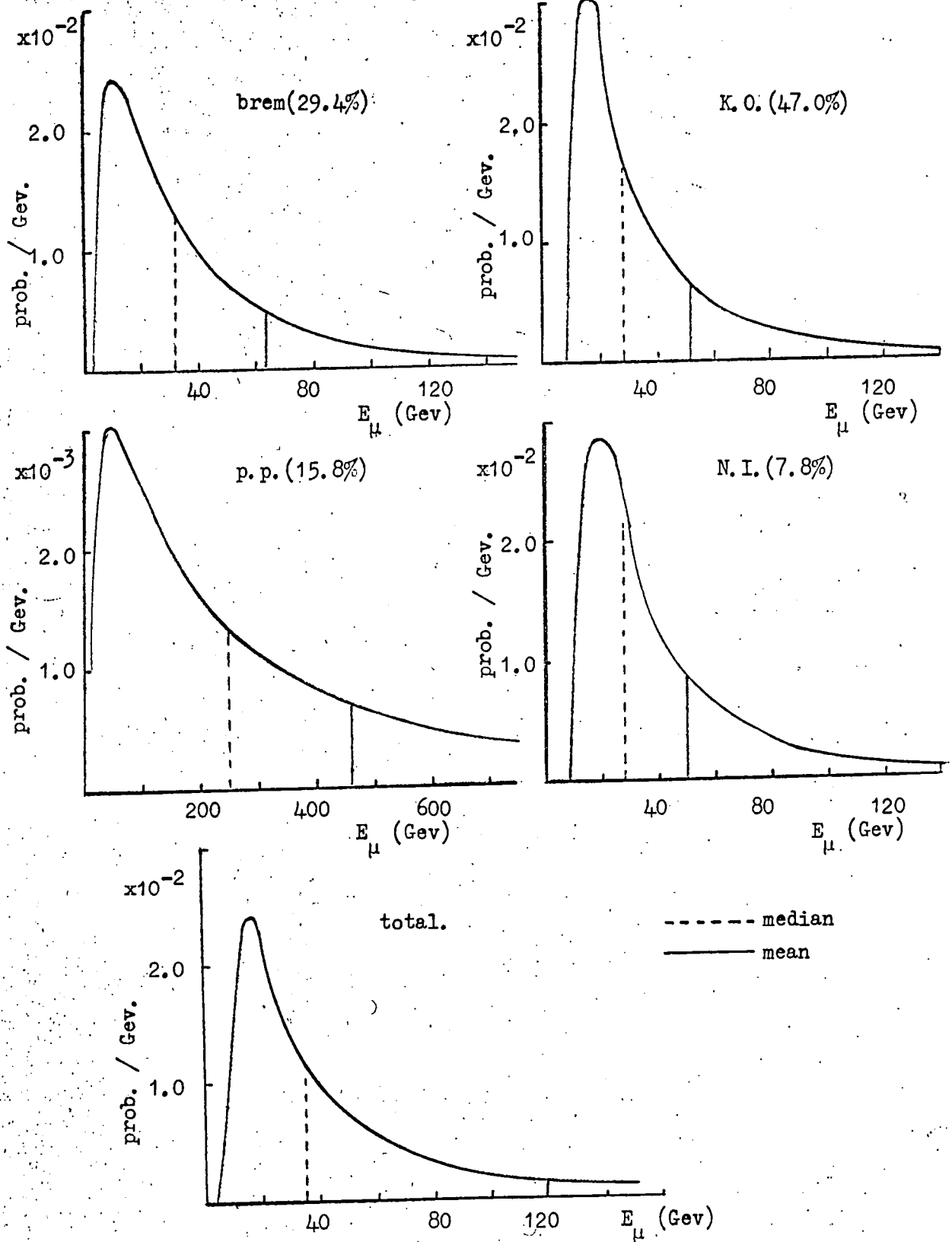

Figure 6.9. Distributions of muon energies producing a burst of 13.2-26.4 particles in S_1 for the different processes. The figures in parenthesis are the relative contributions of each process to the total.

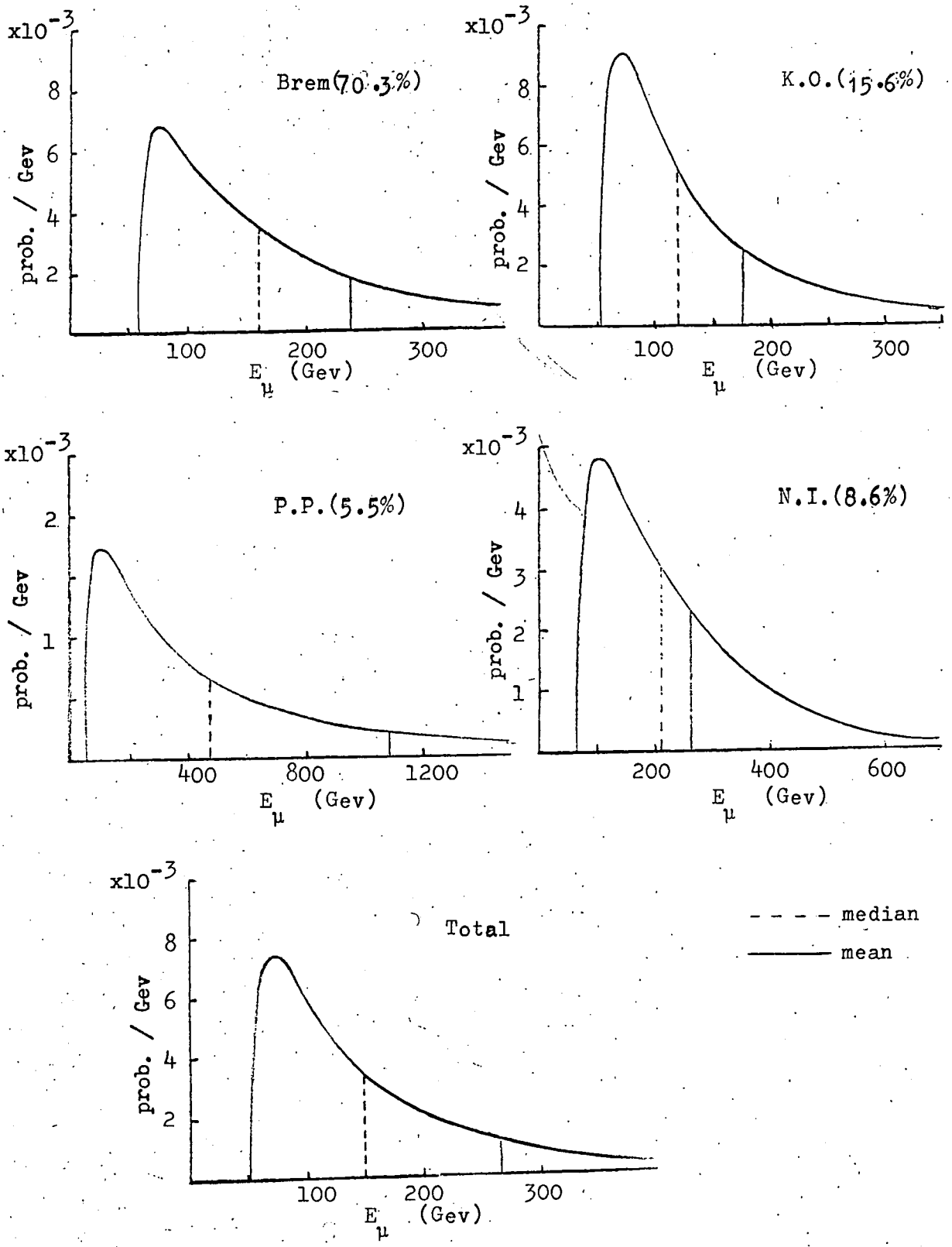

Figure 6.10. Distributions of muon energies producing a burst of 132-264 particles in S_1 for the different processes. The figures in parenthesis are the relative contributions of each process to the total.

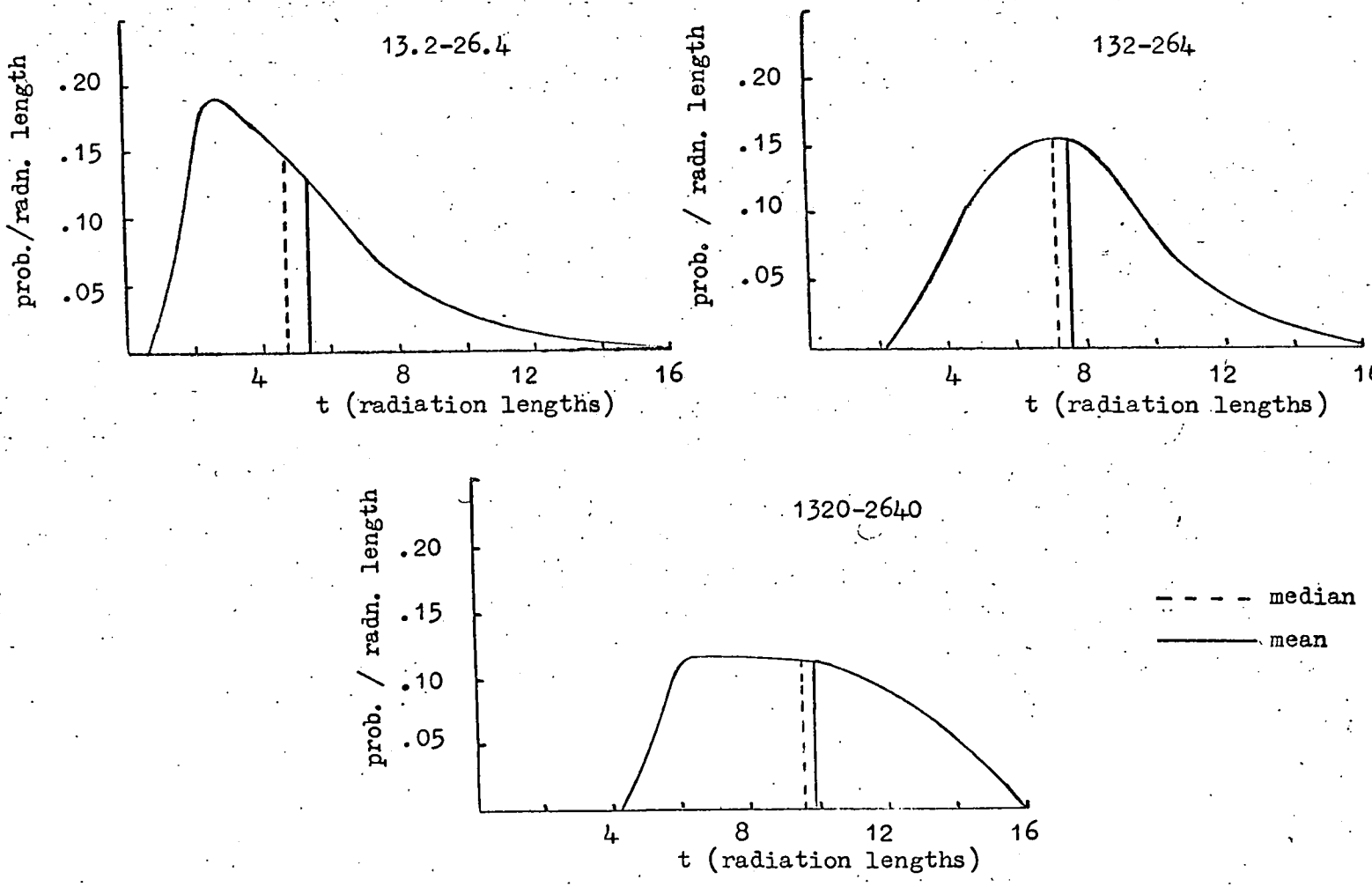

Figure 6.11. Depth probability distributions for various burst sizes in S_1.

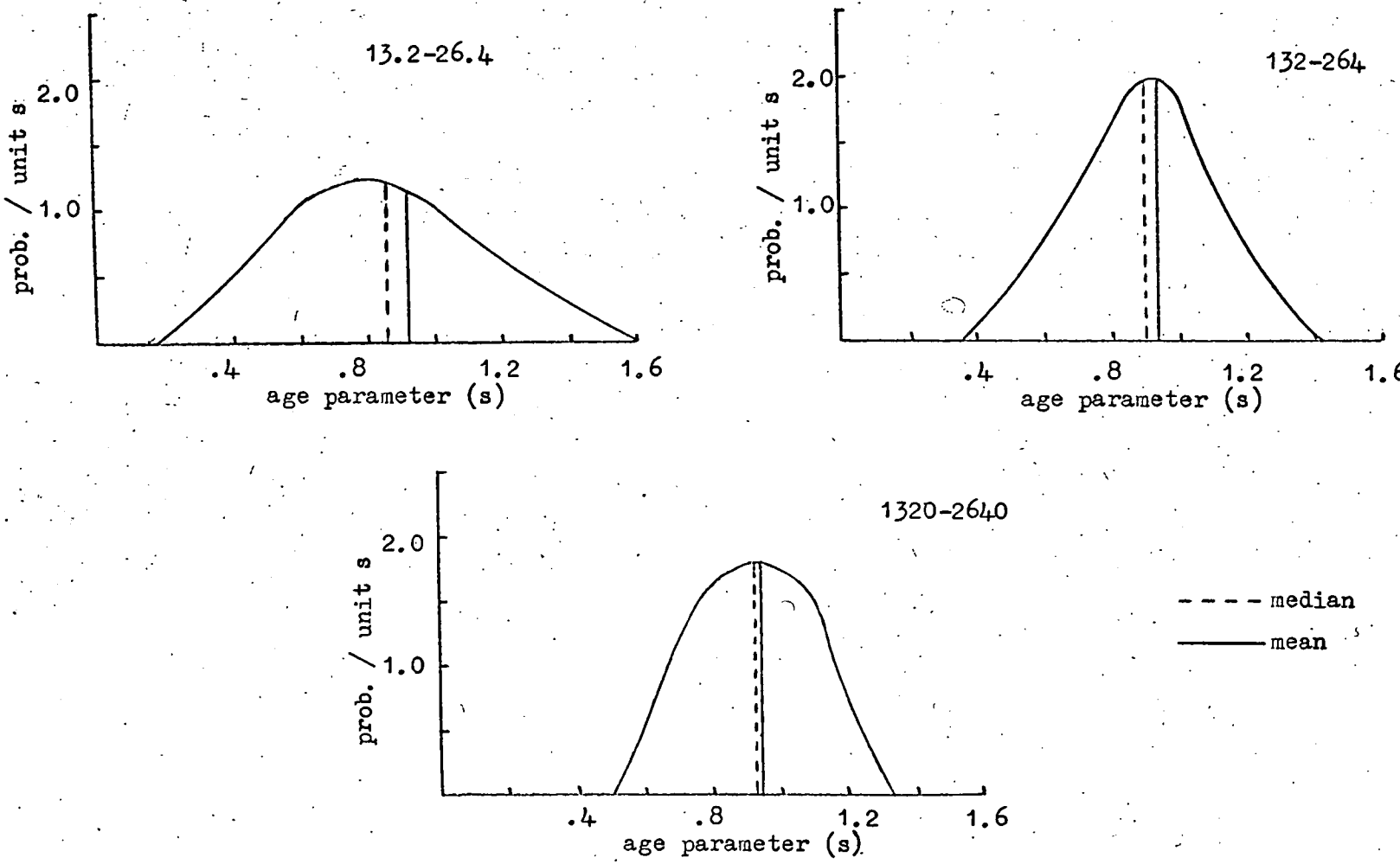

Figure 6.12. Distributions of age parameter (s) for various burst sizes in S_1.

occurring within a few radiation lengths of the scintillator, whereas larger bursts are produced by larger energy transfers taking place further from the scintillator. The depth distributions for three burst sizes ranges are shown in figure 6.11. The mean depth from the scintillator increases from 5.4 radiation lengths for bursts of size 13.2 - 26.4 to a value of 9.9 radiation lengths for bursts of size 1320 - 2640.

Distributions of the age of a cascade giving rise to various burst sizes in S_1 are shown in figure 6.12. The majority of bursts measured in the scintillator are near shower maximum. As the burst size increases the width of the age distribution giving rise to the particular burst decreases, on account of the finite thickness of the absorber.

6.4. Experimental data

6.4.1 Spectra of bursts

The results of the A series, in which 177 bursts were observed in a total useful running time of 489 hours, have been presented by Ashton et al. (1965b). During this series, only S_1 was operational. A further useful running time of 1442 hours was obtained in the B series, during which another 1150 bursts were analysed, 852 occurring in S_1 and 298 in S_2. The two series were mutually consistent.

The total measured spectra of bursts in S_1 and S_2 are compared

with prediction in figures 6.7 and 6.8 respectively. Both theoretical curves have been normalised to the measured points by a factor of 1.18, which was derived from a weighted comparison with prediction of the total number of bursts observed in the running time. The bursts in S_1 are in good agreement with expectation, assuming a constant value of the photonuclear cross-section, and there appears to be no evidence for σ_{hr} increasing as $E^{\frac{1}{2}}$. However, as bremsstrahlung is so dominant, the burst spectrum is not particularly sensitive to the nuclear interaction contribution. The bursts in S_2 are in agreement with theory for burst sizes $\leq$100 particles, but there is a discrepancy between measurement and prediction at larger burst sizes. This result is not considered significant due to the limited statistical accuracy of these latter measurements, especially in view of the agreement found in S_1. All the data for S_1 and S_2 have been grouped together and are shown in figure 6.13 together with the spectra predicted with σ_{hr} constant, and with σ_{hr} increasing as $E^{\frac{1}{2}}$, for $E > 5$ GeV. There is an indication of a better fit to the spectrum calculated assuming an increasing photonuclear cross-section for bursts $\sim$ 300 particles. However, this deviation is the result of the discrepancy observed in the S_2 spectrum at the same burst size. The contribution to the total spectrum by protons is small, amounting to 0.35% for a burst size of 10 particles and decreasing to 0.08% at 100 particles. Also displayed in figure 6.13 are the mean and median muon energies and energy transfers for a particular burst size.

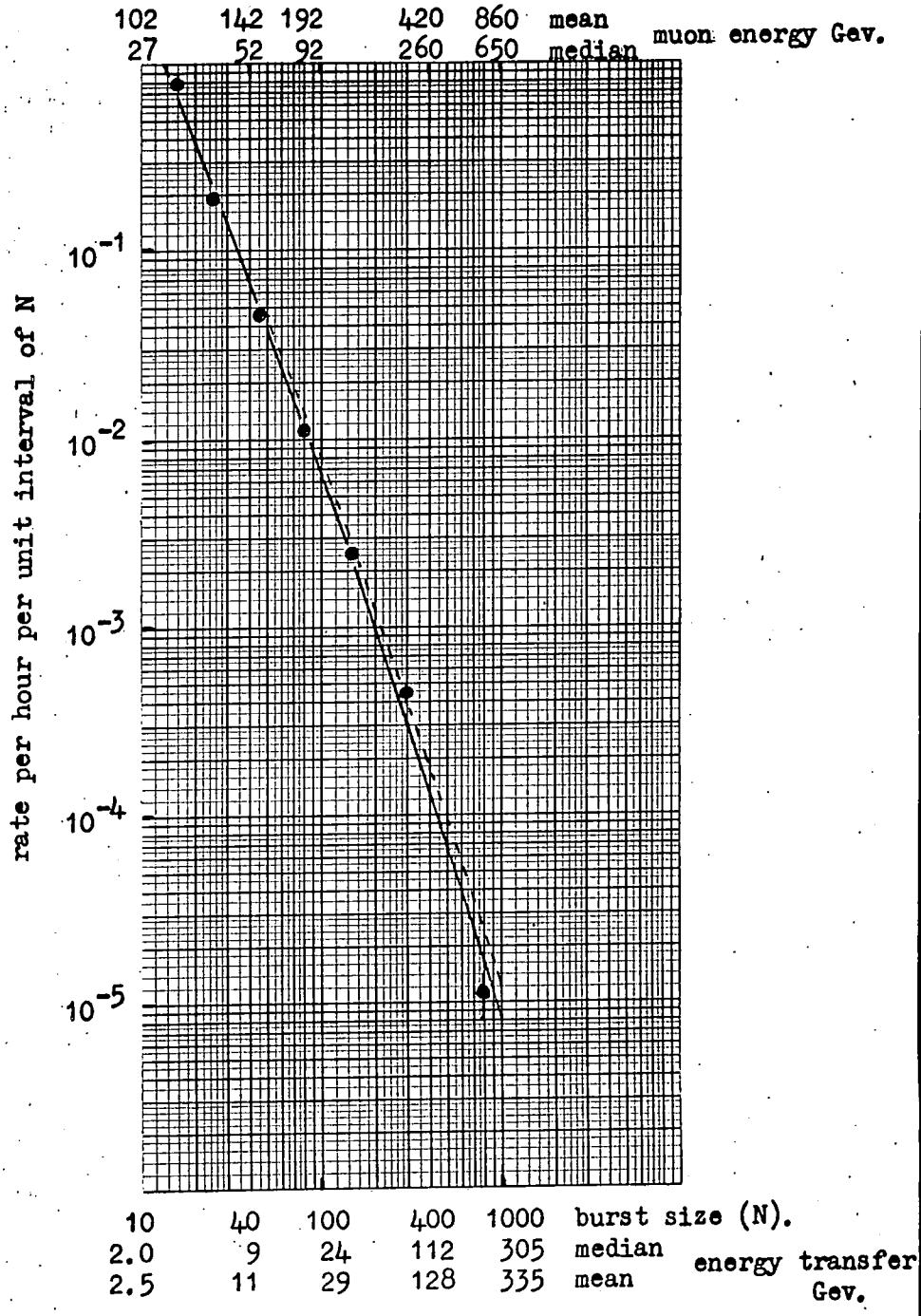

Figure 6.13. The total measured spectrum in both S_1 and S_2, and comparison with expectation. The full line is calculated on the basis of $\sigma_{h\nu}$=constant, and the broken line represents $\sigma_{h\nu}$ varying as $E^{\frac{1}{2}}$.

6.4.2 Angular distributions

Histograms of the projected zenith angle of muons producing bursts in S_1 are shown in figure 6.14, for bursts in the size ranges 12-20 and 100-200. The statistical accuracy of the events in each cell is indicated by the error flag. Also shown are the predicted distributions, which are in fair agreement with the measured distributions. There is no indication of any significant contribution from protons, which is in agreement with prediction. The angular distributions for S_2 are displayed in figure 6.15. Again, there is fairly good agreement between the measured and predicted distributions, considering the limited statistical accuracy of the S_2 bursts. These results indicate that the particles producing the bursts are in fact muons, as expected.

6.4.3 Lateral spread of bursts

One dimensional cascade theory assumes that all particles retain the direction of the shower axis, and neglects any angular deviation of the electrons. In practice this is not valid. The lateral spread of bursts, illustrated by C and D flash tube trays in figure 2.1, is principally due to multiple Coulomb scattering.

In figure 6.16 the mean number($\overline{N}_{cd}$) of flashes in trays C and D has been plotted as a function of burst size in S_1 as a 'dot' distribution, and the full line represents the best fit to the

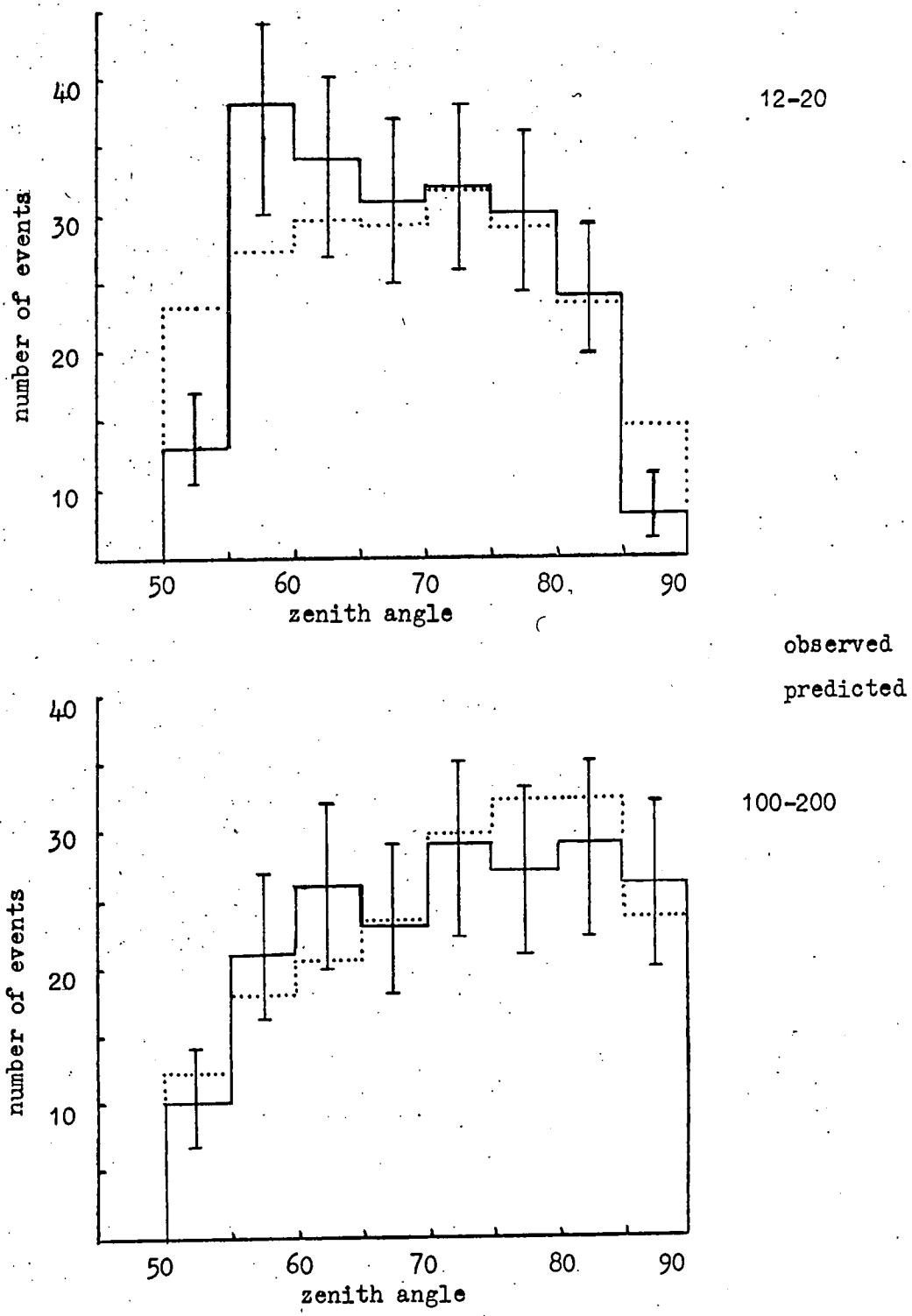

Figure 6.14. Angular distributions of bursts measured in S_1. The statistical accuracy of the number of events in each cell is indicated by an error flag. The broken line is the predicted distribution.

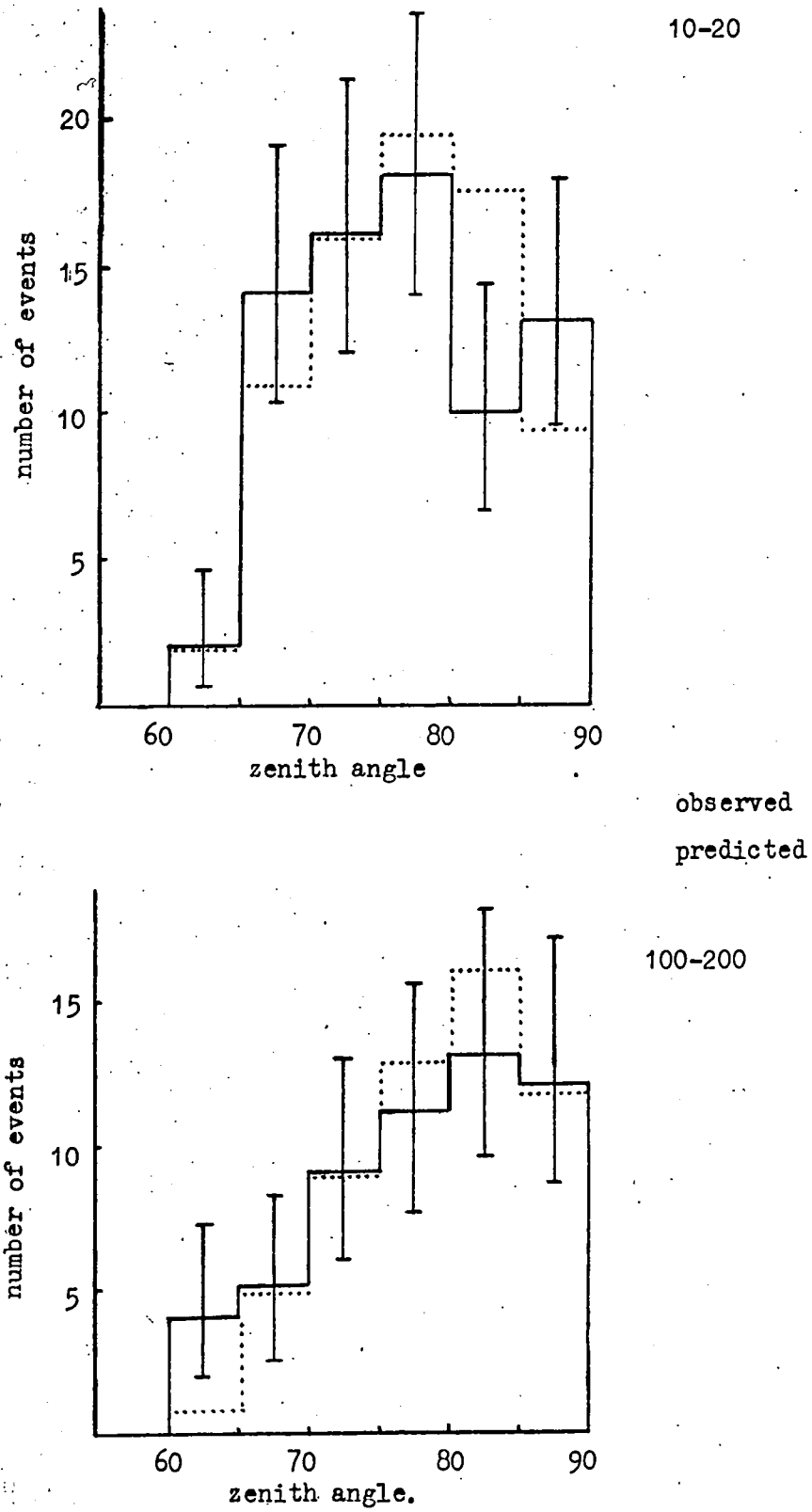

Figure 6.15. Angular distributions of bursts measured in S_2. The statistical accuracy of the number of events in each cell is indicated by an error flag. The broken line is the predicted distribution.

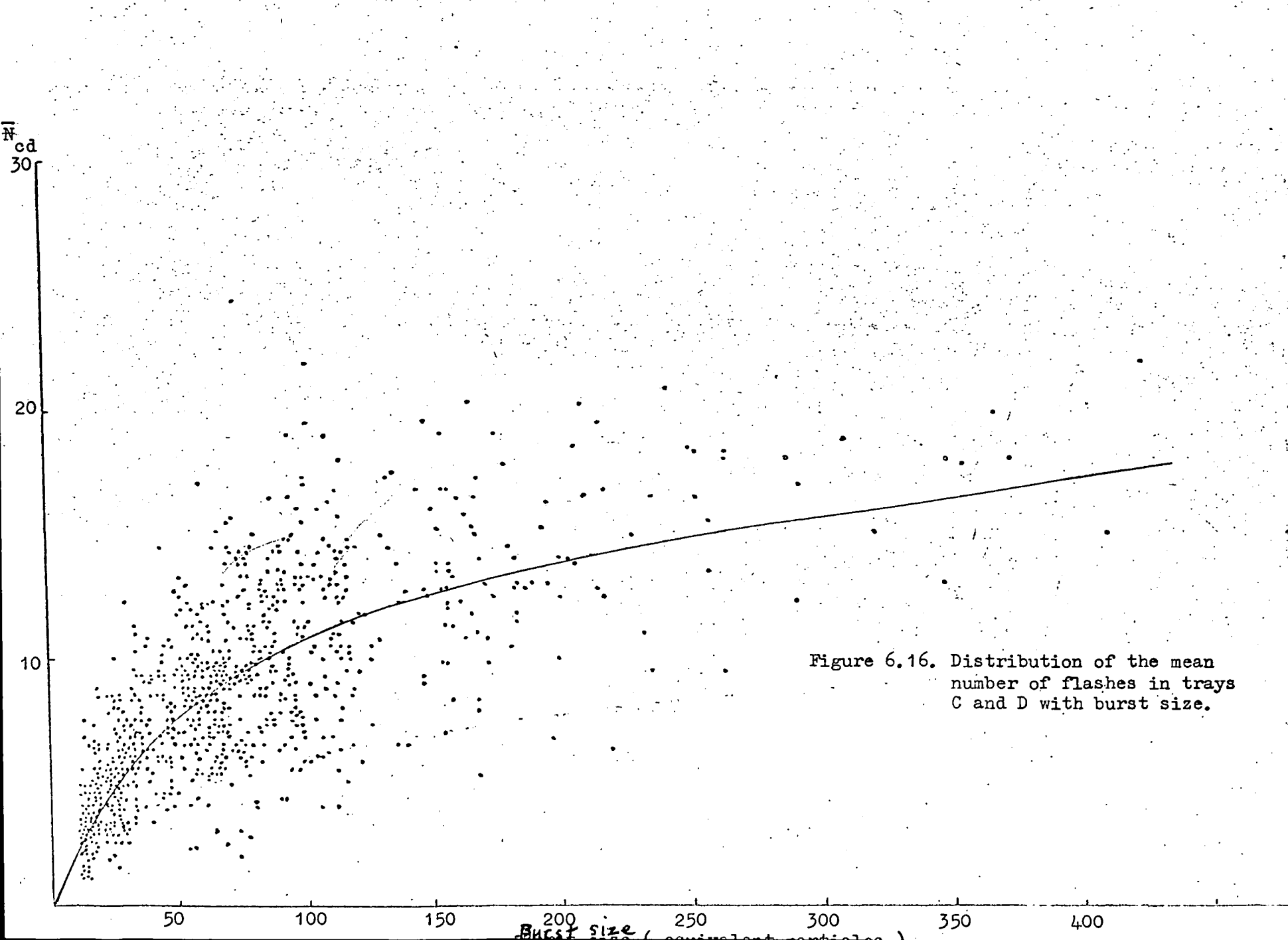

Figure 6.16. Distribution of the mean number of flashes in trays C and D with burst size.

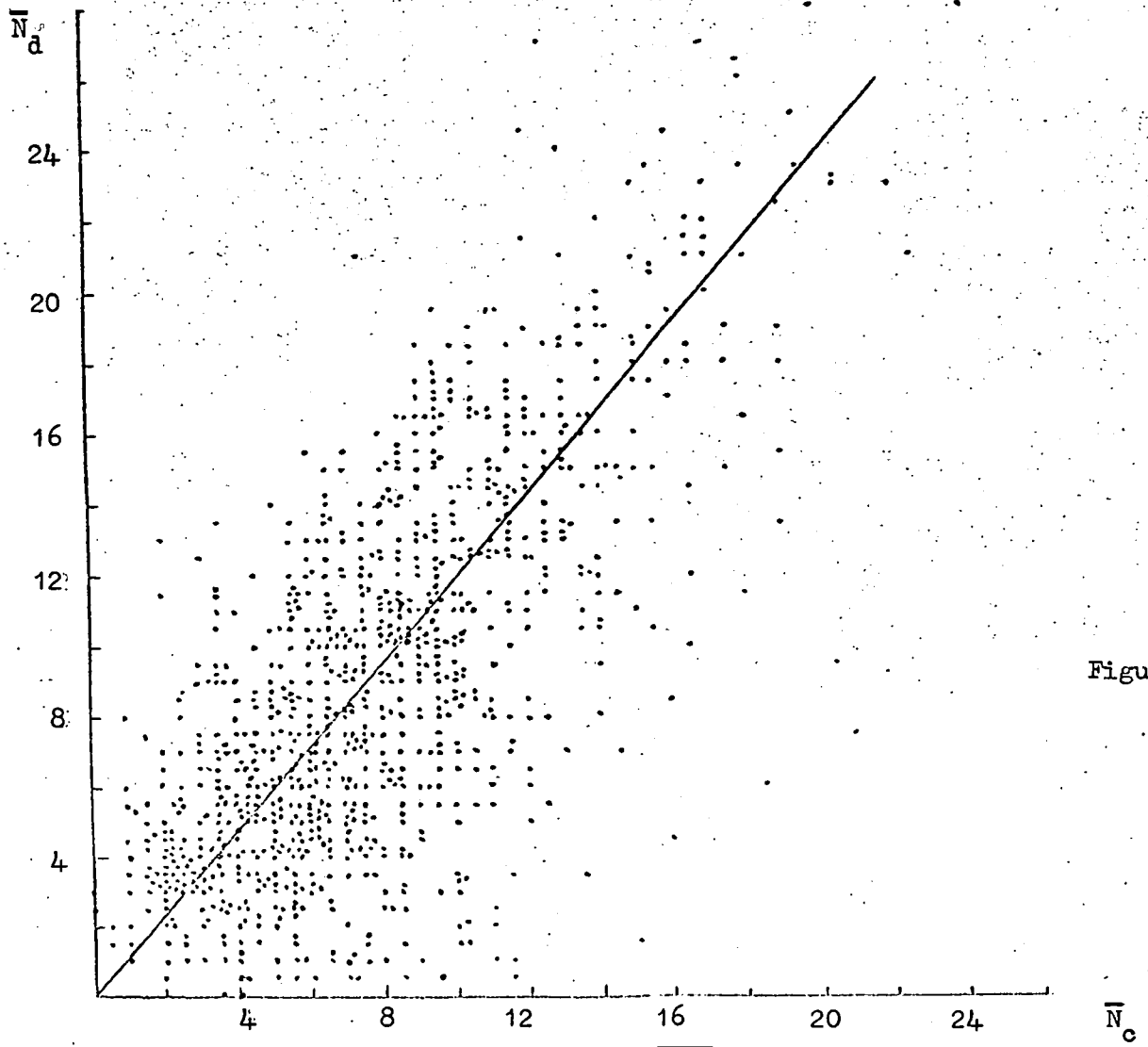

Figure 6.17. Distribution of the mean number of flashes in C with the mean number in D. The full line is the mean of the distribution.

points. The spread in $\bar{N}_{cd}$ for a given burst size is mainly due to the age variation. Young bursts produced by energy transfers occurring near the scintillator should be well collimated, whereas the effects of Coulomb scattering will be more pronounced on bursts reaching the scintillator after shower maximum, due to the lower mean particle energy. The mean number of flashes $(\bar{N}_c)$ in tray C has been plotted against the mean number $(\bar{N}_d)$ in D in figure 6.17. The full line is the best fit to the points, and is represented by $\bar{N}_d = 1.19\ \bar{N}_c$, showing that the electrons 'fan out' while traversing the scintillator. However, the effect is not as large as would be expected from geometrical considerations, which indicates absorption of the low energy electrons most distant from the shower axis.

6.5 Conclusions

The spectra of bursts measured in S_1 and S_2 are in agreement with the spectra predicted on the basis of Q.E.D. This result indicates the validity of the theoretical cross-sections for μ - e collision and bremsstrahlung for energy transfers $\leq$ 10 GeV and $\leq$ 200 GeV respectively. The agreement between the measured and predicted angular distributions shows that muons are the parents of the bursts.

CHAPTER 7

FEASIBILITY OF MEASURING THE HIGH ENERGY MUON SPECTRUM

7.1. Introduction

The momentum spectrum of muons incident at large zenith angles has been measured for momenta $\leq$ 2000 GeV/c using magnetic spectrographs, and Borog et al. (1965) have estimated the spectrum in the region 300 - 3000 GeV/c from burst measurements in an ionisation calorimeter. Both approaches are discussed in Chapter 3. However, these techniques are limited at higher muon momenta. Although magnetic spectrographs measure every particle traversing the apparatus, the number of high energy muons accepted is small due to the small apertures of present spectrographs. In calorimeter experiments the aperture can be made large, so that the flux of high energy muons is large compared with that of spectrographs. However, only a certain fraction of muons will undergo an electromagnetic interaction in the calorimeter. Hence the burst experiments are limited by the cross-sections for interaction.

It was pointed out by Alexeyev et al. (1959) that the effective cross-section for direct pair production increases rapidly with primary energy, and becomes the dominant process for large energy muons (> 1000 GeV) producing low energy transfers (~ few GeV). This process offers a possible means of recording every high energy muon with a large area multi-layer system of detectors.

7.2 Theoretical considerations

The feasibility of using the Durham horizontal burst apparatus to measure the high energy spectrum will be discussed first. The selection criteria of the array used in this mode of operation would be a single pulse from G_2 and two simultaneous pulses from S_1 and S_2, together with no pulse from S'. There are two types of process which can give rise to a double burst event, i.e. a burst in S_1 together with one in S_2.

In double energy transfer events two independent energy transfers take place, one in F_1 giving rise to a small burst in S_1, and a second in F_2 producing a burst in S_2. Direct pair production and μ - e collision are the processes which principally contribute to these events. Theoretical burst spectra have been derived using the M.U.T. cross-sections for pair production and the Bhabba expression for the μ - e collision cross-section given in Chapter 4. The burst spectrum in S_1 has been derived on the basis of a burst in S_2 of size $N_{S2} > 3$ particles, and is shown in figure 7.1 for the two cases of $E\mu > 500$ GeV and $E\mu < 500$ GeV. In the former case pair production is the major contributor, whereas μ - e collision plays an increasing role at lower muon energies.

A double burst can also arise from a large energy transfer taking place in F_1, and some of the resulting cascade surviving to reach S_2. These large transfers come mainly from bremsstrahlung, for which the double spectrum has been evaluated and is shown in

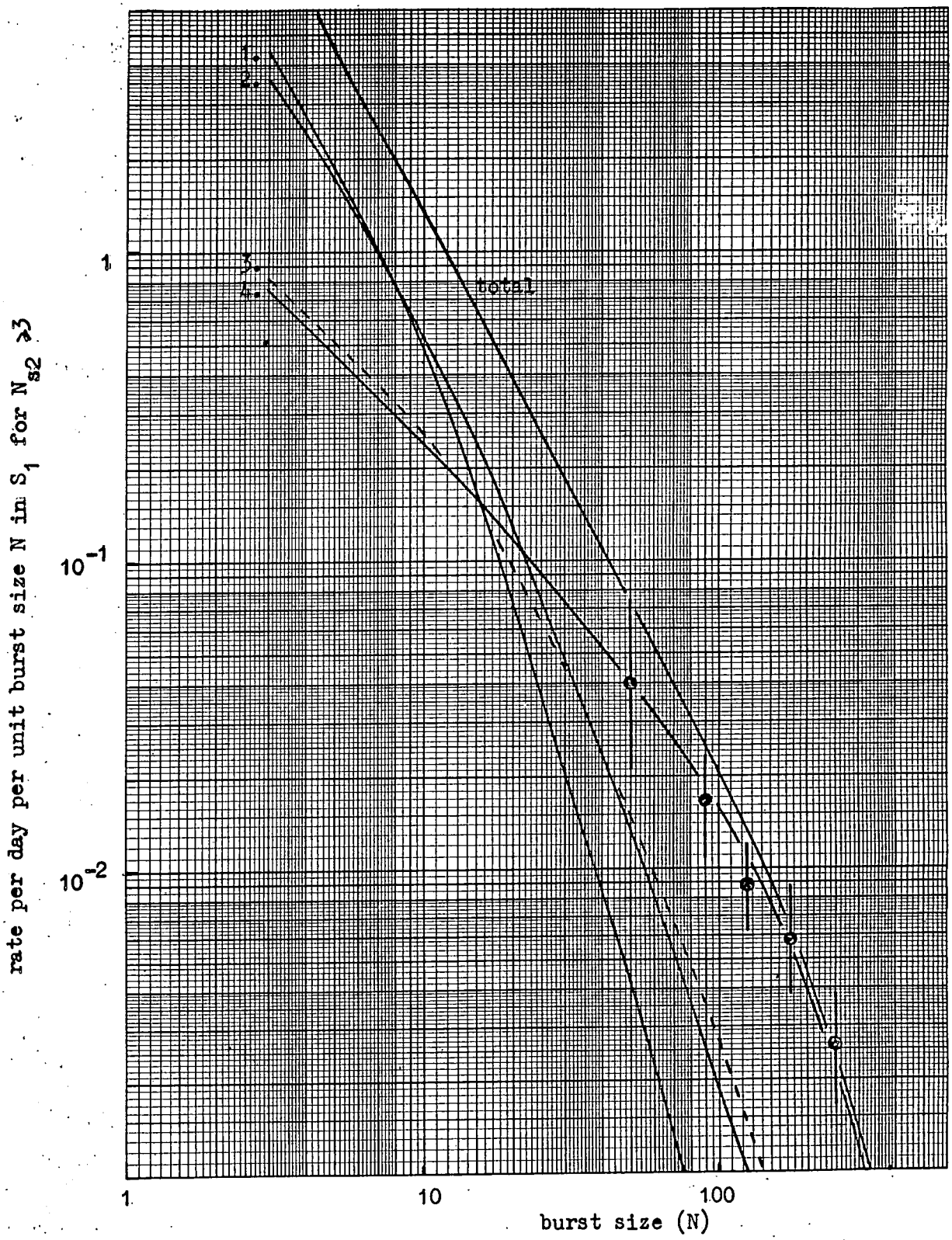

Figure 7.1. Spectra of double bursts due to the various processes.

1. E_μ <500 Gev
2. E_μ >500 Gev
} double energy transfers.

3. Nuclear interaction
4. Bremsstrahlung
} single energy transfers.

figure 7.1. Also displayed in the same figure are the experimental data available from the single burst runs, in which bursts were selected by a large pulse from either S_1 or S_2. These events were selected on the basis of a large pulse in S_1, together with the mean number of flashes in S_2 being $\bar{N}_E \geq 3$ (S_2 pulse was too small to be recorded). The agreement between prediction and the experimental results is good, considering the limited statistical accuracy of the measurements.

A nuclear interaction of a muon occurring in F_1 also gives rise to a double burst, due to the resulting pion cascade. The expected double burst spectrum has been evaluated, and is shown in figure 7.1. No account of the pion transverse momentum has been taken in these calculations.

7.3. Possible experimental arrangements

Over the burst size range N_{S1}= 3 - 10 particles the dominant contribution comes from double energy transfers (figure 7.1). Due to the relative abundance of muons with energy < 500 GeV, the contribution to the total double burst spectrum of muons in this energy range is similar to that of muons with $E\mu > 500$ GeV. For N_{S1}= 3 - 10 and $N_{S2} > 3$ the rate of doubles is ~ 10/day from $E\mu < 500$ GeV and $E\mu > 500$ GeV, i.e. a total of ~ 20/day. The introduction of a third absorber and scintillator would reduce the spectrum of double bursts produced by muons with $E_\mu < 500$ GeV, but with the present apparatus the extra length of arm would

reduce the effective aperture.

A better experimental apparatus would be a multi-layer detector of large aperture, with sufficient layers to reduce the multiple bursts produced by muons with $E\mu < 500$ GeV to a level which is negligible in comparison with the rate of multiple bursts produced by higher energy muons, but with large enough aperture so as to obtain an appreciable flux of high energy muons traversing the apparatus. A possible experimental arrangement is shown in figure 7.2. The apparatus essentially consists of four interaction blocks, each composed of an iron absorber (10 radiation lengths) together with a plastic scintillation counter and one tray of flash tubes containing 2 layers of tubes. A fifth scintillator (S) is used in the selection system. A tray of flash tubes (8 layers) is situated in front of S, and is used to select events produced by single particles incident on the array. The anti-coincidence scintillator (S′) is in the selection system to reduce the number of extensive air showers triggering the array. The selection criterion is:

$$S\ (\geq 1)\ S_1\ (\geq 3)\ S_2\ (\geq 3)\ S_3\ (\geq 3)\ S_4\ (\geq 3)\ \overline{S'(\geq 1)}.$$

With scintillation counters of area 75 x 140 cm^2 the rate of muons with $E\mu > 1000$ GeV is $\sim$ 18/day. Approximate rates of multiple bursts with ≥ 3 particles in each block are:

$E\mu(>1000)$: 1.9 day^{-1} ; $E\mu(500\text{-}1000)$: 3.3 x 10^{-1} day^{-1} ;

$E\mu(<500)$: 1.3 x 10^{-1} day^{-1}.

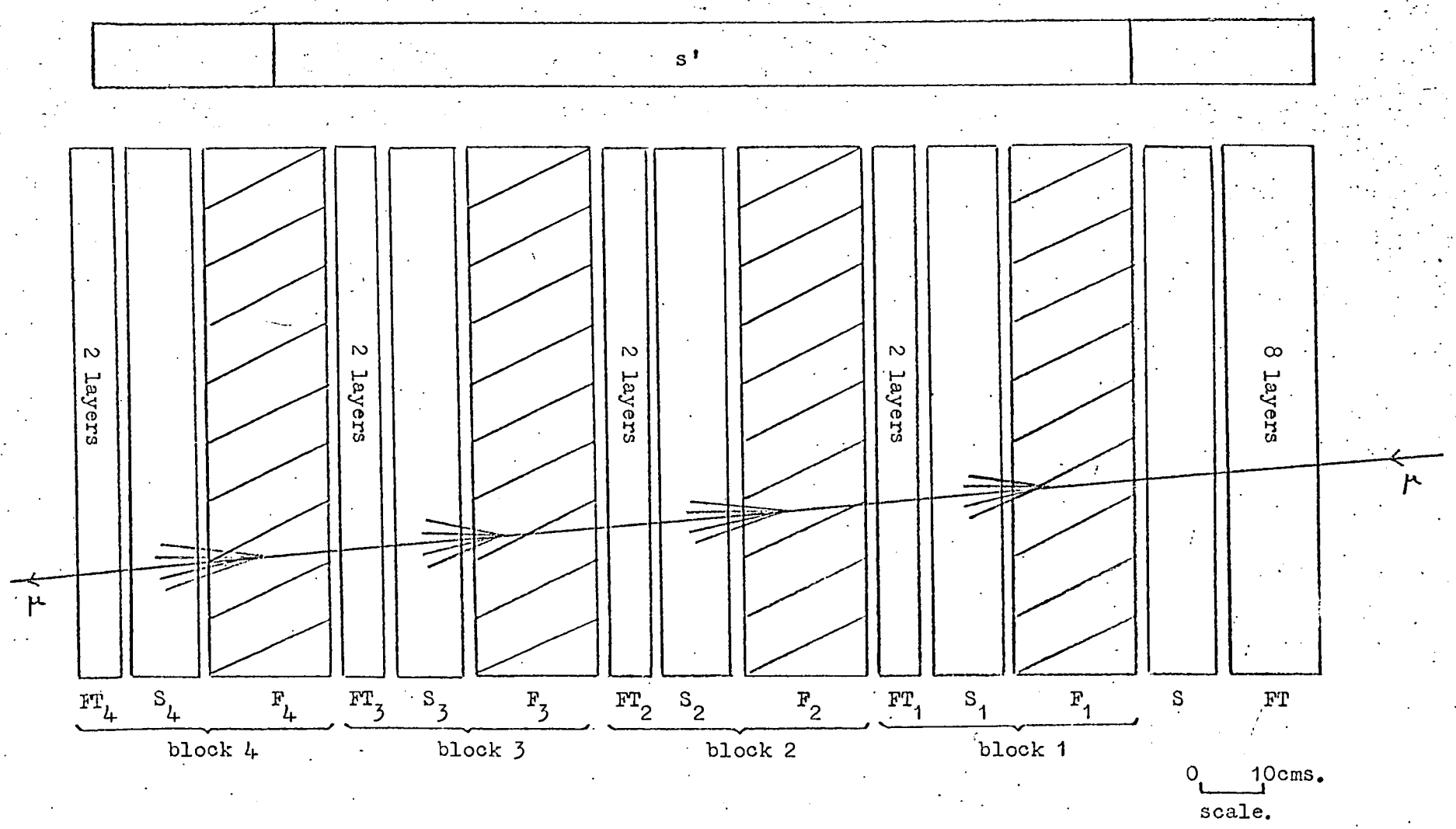

Figure 7.2. Scale diagram of proposed apparatus to measure the high energy muon spectrum by means of multiple bursts.

The values of E_μ correspond to the energy range of muons producing the multiple bursts. With this arrangement, ~ 10% of muons with $E_\mu > 1000$ GeV are detected. These rates correspond to muons incident from only one direction, and so could be increased by a factor of 2 by accepting bursts produced by muons traversing the apparatus in both directions. The thickness of absorber in each block has been selected to be 10 radiation lengths to reduce the effect of a transfer occurring near the end of one target, say F_1, and some of the cascade surviving to satisfy the selection criterion of S_2.

During the initial stages of development the apparatus would be operated with both scintillators and flash tubes, the latter being used to visually select events produced by single muons. The pulse heights from the five scintillators (S, S_{1-4}) would be recorded on punched tape, and only those events analysed which correspond to a single track. There would be no ambiguity on account of events produced by bremsstrahlung or nuclear interaction of muons. Both would be distinguishable because of the large pulse heights, which would correspond to four sampling levels on the cascade curve. In the case of four independent energy transfers there should be no correlation between pulse heights. Also, in a true event, each scintillator should register ~ 3-10 particles, so that upper level discriminators could be incorporated in the selection system to cut out bremsstrahlung and nuclear interaction events. If it was found that events could be selected without

the visual technique, then the apparatus could be fully automated.

7.4. Previous Experiments

A spark calorimeter, consisting of 5 layers of spark chambers separated with lead filters 15 cms. thick, has been operated by Bibilashvili et al. (1965) at a depth of 200 m.w.e. underground. The total sensitive area was 60 x 50 m^2. High energy muons passing through the calorimeter generated electron-positron pairs in the filters, and the resulting cascades are detected by the spark chambers. A spectrum of bursts was measured, and it was estimated that the interactions were produced by muons with energy in the range 100 - 1000 GeV. However, no attempt was made to derive the spectrum expected from the known cross-sections for the interactions producing bursts.

7.5. Conclusions

It would seem feasible to measure the high energy muon spectrum at large zenith angles using the technique of multiple bursts. With the present Durham apparatus, it would be difficult on account of the contamination from muons with energy <500 GeV, but this can be overcome by building a multi-layer detector.

CHAPTER 8

THE VERTICAL BURST EXPERIMENT

8.1. Introduction

Nuclear interactions of high energy cosmic ray protons, neutrons and pions incident at small zenith angles ($<50^{\circ}$) have been studied. The apparatus is very simple. It essentially consists of an iron target (F), 20 cms thick, beneath which is a liquid paraffin scintillation counter (S), of area 1.2 m^2 and of the type described in Appendix A. A scale diagram is shown in figure 8.1. The iron presents a target of thickness 1.18 interaction lengths to protons, so that the probability of an incident proton interacting in the iron is 69%. The energy transferred to secondary particles as a result of the interaction is detected by the scintillation counter in the form of a burst. Pions are predominantly produced in a nuclear interaction. Neutral pions decay rapidly into two γ-rays, which initiate an electromagnetic cascade. The charged pions produced in the initial interaction interact deeper in the iron to produce further charged and neutral pions. Hence, emerging from the iron will be a burst compring electrons, photons and pions. Bursts are also produced by electromagnetic interactions of muons.

Two trays of neon flash tubes, A and B, each containing two layers of flash tubes on either side of a central electrode, are mounted above the iron, and are used to determine the projected zenith angle of the particle producing the burst. Two other trays, C and D

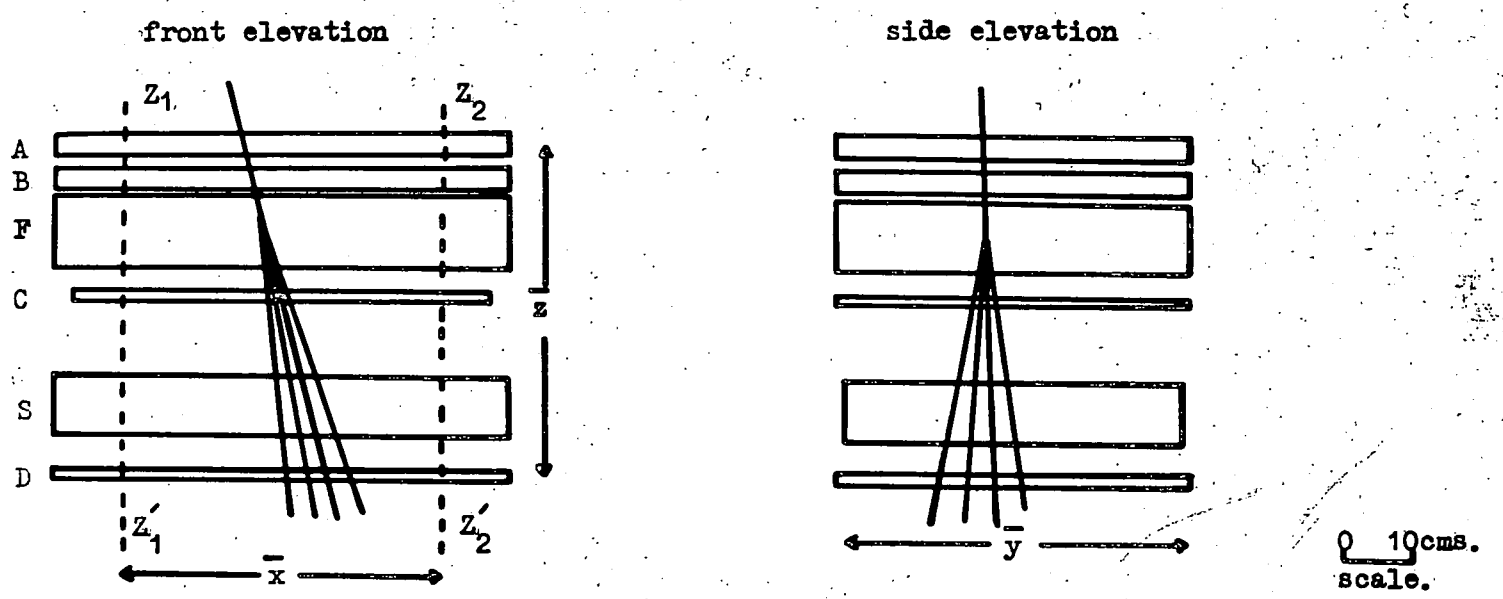

Figure 8.1. Scale diagram of the apparatus. A,B,C,D - flash tubes; S - scintillation counter; F - iron. The sensitive volume of the apparatus is the cuboid defined by the width of the phosphor ($\bar{y}$), the distance between the central electrodes of A and D ($\bar{z}$), and the distance between the broken lines $Z_1Z'_1$ and $Z_2Z'_2$. ($\bar{x}$).

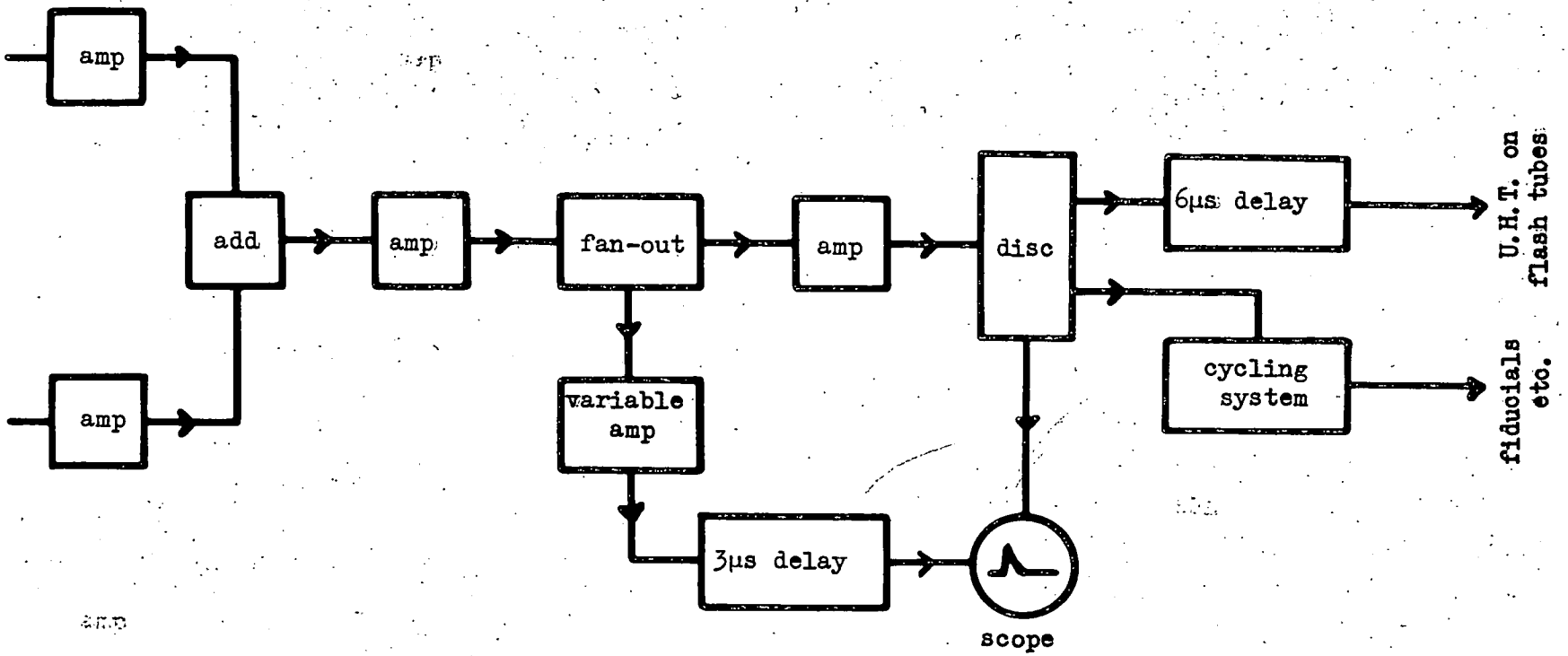

Figure 8.2. Block diagram of the electronics.

are mounted on either side of the scintillator so as to give visual information about the burst. C and D each contain two layers of flash tubes.

8.2. Calibration

A block diagram of the electronics is shown in figure 8.2. Pulses from the two photomultipliers are added, and the resulting pulse is fanned out after being amplified. The pulse on one channel of the fan-out is displayed on an oscilloscope, whilst the second pulse is fed into a discriminator. Events are selected by demanding a pulse larger than a predetermined level at the input to the discriminator. When this selection criterion is satisfied the oscilloscope is triggered, and the pulse recorded on film. A second camera is used to photograph the flash tube trays.

The photomultipliers and electronics were as used in scintillator S_1 in the horizontal burst experiment. The matching of the E.H.T's. on the two photomultipliers was checked using the light flasher, and was found to be consistent with the previous calibration. In order to extend the range of sizes over which bursts could be accepted, the E.H.T. on the photomultipliers was reduced to:

$$A_p : 1.2 \text{ kv} \quad ; \quad C_p : 1.1 \text{ kv}.$$

The size of a burst is defined as the ratio of the measured pulse height to the pulse height produced by a single ionising particle traversing the counter at normal incidence. A small geiger

telescope was employed to select vertical relativistic particles traversing the centre of the counter, and the resulting distribution of pulse heights due to single particles is shown in figure 8.3. The mean pulse height was 1.22 mv, with a full width of half-height of 85%. The efficiency of the flash tubes was also determined during the single particle calibration, the mean layer efficiency in trays A and B being 73%. A track in A and B is defined as being $n \geq 3$ flashes in a line, so that the probability of a charged particle traversing A and B and producing $n < 3$ flashes, is 0.64%.

8.3. Analysis of data

When an event is selected, the scintillator pulse is recorded on film from an oscilloscope, and the flash tube trays are photographed by a second camera. When the films are scanned, events are classified into two categories:

(a) Bursts produced by a charged particle ($B^{\pm}$).

(b) Bursts produced by a neutral particle (B^{o}).

Typical examples of each type of event are shown in figure 8.5. The upper photograph is a burst of size 188 equivalent particles produced by a charged particle incident on the iron at a projected zenith angle of 21^{o}. The lower photograph shows a B^{o} event of burst size 221 equivalent particles.

With such a free selection criterion for the triggering of the apparatus, it is necessary to define some sensitive volume.

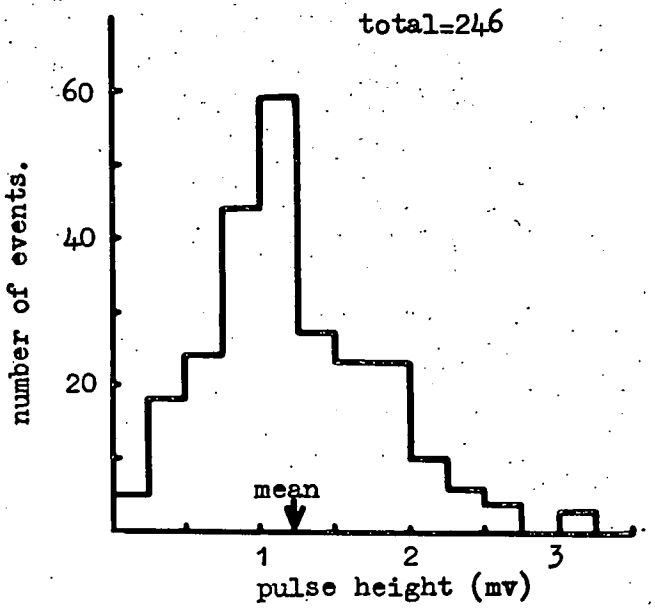

Figure 8.3. Distribution of pulse heights produced by single particles traversing the scintillator at normal incidence.

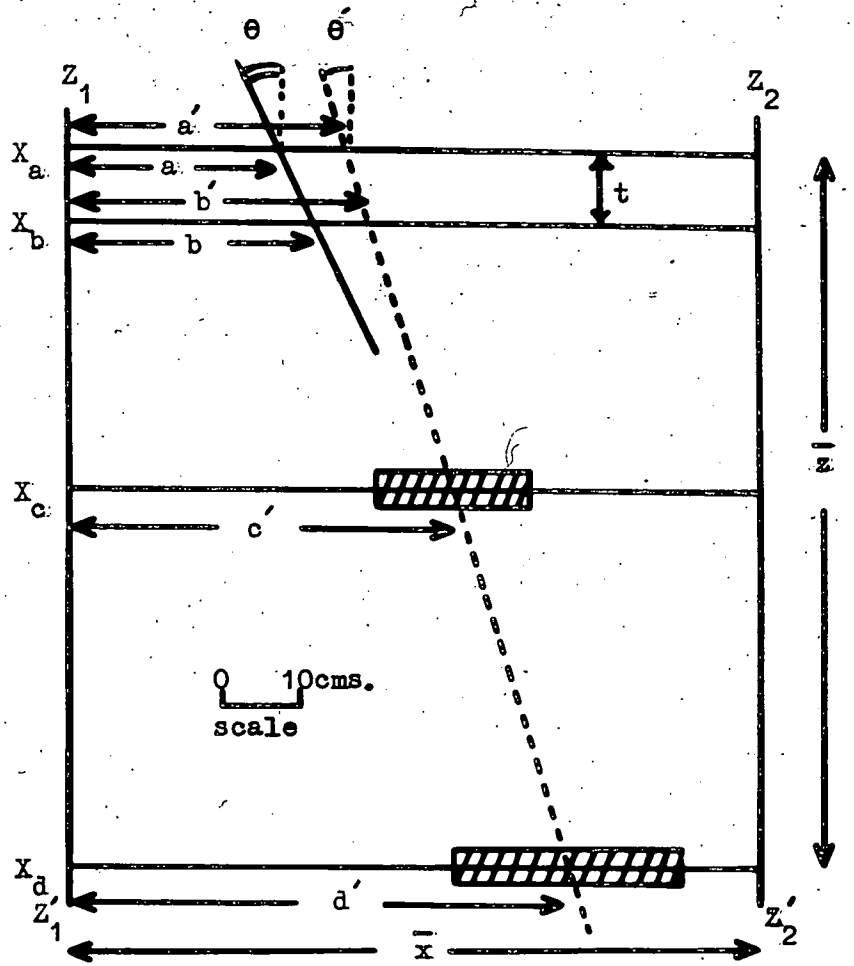

Figure 8.4. Sensitive area of the apparatus, showing the parameters measured during the film scanning.

a.

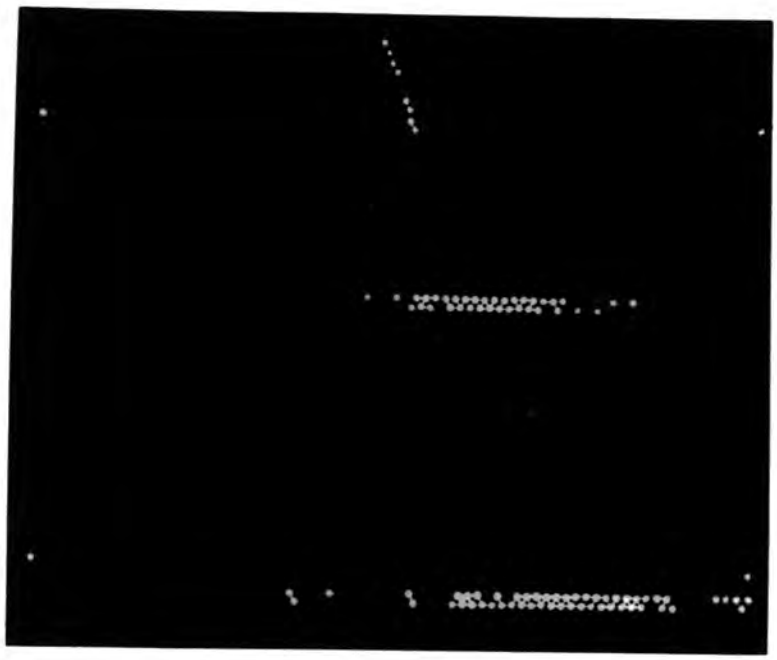

b.

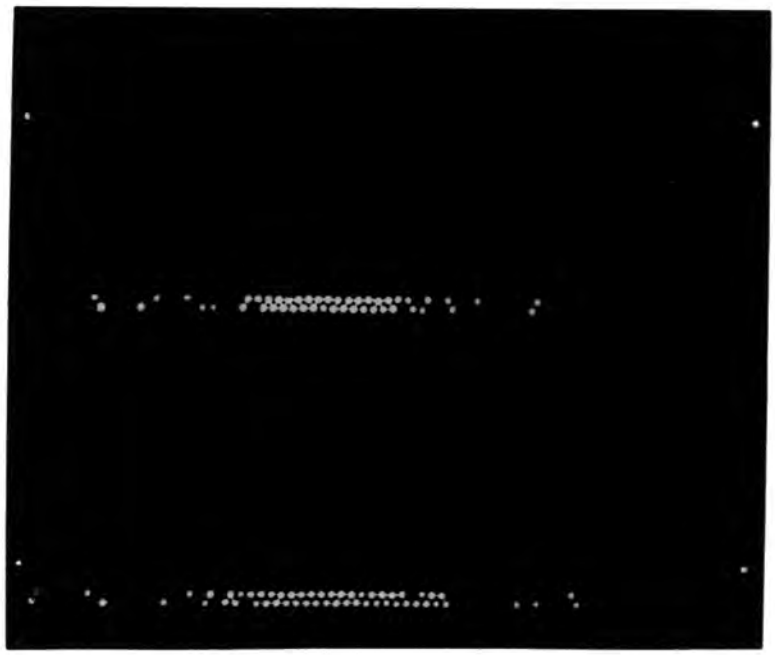

Figure 8.5. Unaccompanied bursts.

a. $B^{\pm}$ N_s=188 particles. θ=21.1°E.

b. B^{o} N_s=221 particles. θ= 0.7°E.

In this preliminary experiment the flash tubes were not crossed. Three mutually perpendicular axes are defined such that the x-axis is in the plane of the central electrode of tray A and perpendicular to the direction of the tubes. The y-axis is parallel to the lengths of the flash tubes, and the z-axis is perpendicular to the plane of the electrode. The sensitive volume is the cuboid defined by the width of the phosphor ($\bar{y}$), the distance ($\bar{z}$) between the central electrodes of the flash tube trays A and D, and the distance ($\bar{x}$) between two limits Z_1Z_1' and Z_2Z_2' as shown in figure 8.1. These two limiting lines have been selected from consideration of the lateral spread of the bursts, as indicated by trays C and D. The photographs in figure 8.5 show that the burst is made up of a central region in C and D, over which tubes in both layers have flashed, and a region at either end where there are scattered flashes.

A diagram of the sensitive area of the apparatus is shown in figure 8.4. X_A, X_B, X_C and X_D represent the central electrodes of the flash tube trays A, B, C and D respectively, and are used as co-ordinate axes. Z_1Z_1' and Z_2Z_2' are the limiting lines, selected so that there are at least 10 flash tubes in any layer of C and D outside the limits. This enables events to be used in which the median of the central region lies on either Z_1Z_1' or Z_2Z_2'.

The projected zenith angle θ of a $B^{\pm}$ event can be measured

directly. However, there is no track in A and B in a B^{o} event, so that the projected zenith angle must be determined from C and D flash tube trays. c′ and d′ in figure 8.4 are the co-ordinates of the medians of the central regions of the bursts in trays C and D respectively, and the line through these points is taken to be the best estimate of the trajectory of the primary particle. This line intersects X_A and X_B at the respective co-ordinates a′ and b′, so that the estimated value of the projected zenith angle θ' is given by

$$\theta' = \tan^{-1}\left(\frac{a'-b'}{t}\right)$$ where t is the separation of X_A and X_B.

The accuracy of θ' as a measure of the true projected zenith angle θ can be determined from the $B^{\pm}$ events. Two co-ordinates a and b are measured from the track recorded in each event, and θ is given by:

$$\theta = \tan^{-1}\left(\frac{a-b}{t}\right).$$

A frequency histogram of $(\theta-\theta')$ is shown in figure 8.6. The distribution is peaked towards small values of $(\theta-\theta')$, the mean and median values being 2.78^{o} and 1.92^{o} respectively, indicating that the projection method used to determine the trajectory of neutrals producing bursts in the apparatus gives a reliable estimate of the true zenith angle. The difference between the true co-ordinate (a), as measured on the reprojection system employed to scan the films, and the estimated co-ordinate (a′) is shown as a

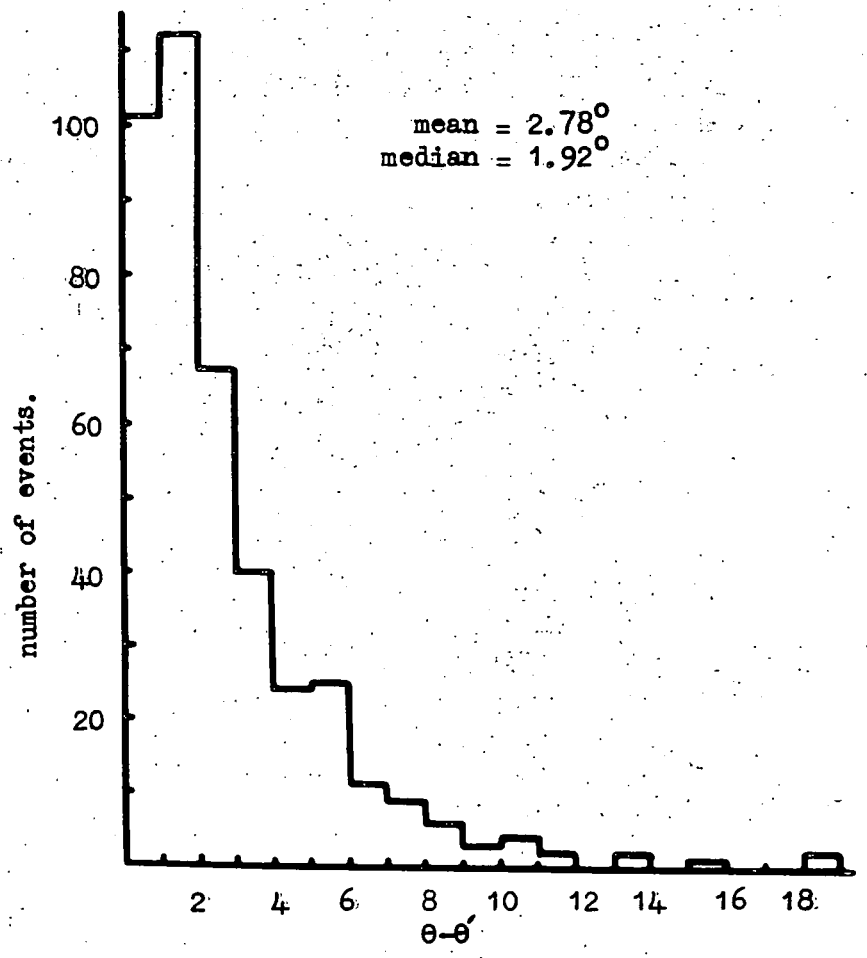

Figure 8.6. Distribution of the difference between true projected zenith angle (θ) and estimated projected zenith angle (θ́) for B events.

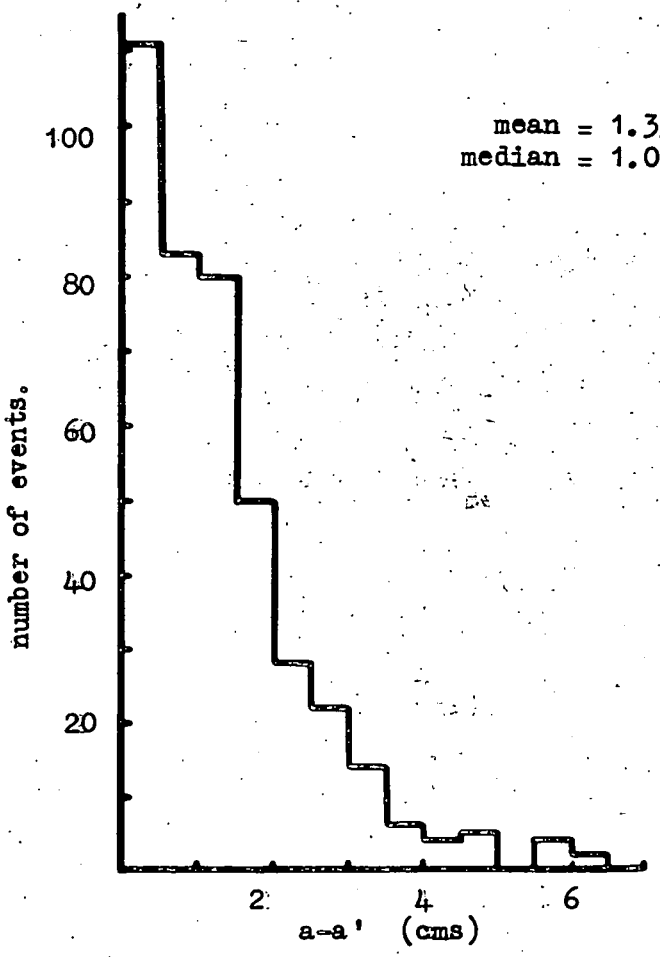

Figure 8.7. Distribution of the difference between the true co-ordinate (a) and the estimated co-ordinate (a) as measured from the reprojection system.

frequency distribution in figure 8.7. The mean and median values are 1.33 cms and 1.07 cms respectively. The reprojection system had a demagnification of 2.51, so that the mean of 1.33 cms is equivalent to a true magnitude of 3.33 cms. Thus, the trajectory of a neutral can be located to within 2 flash tubes at the central electrode of tray A, with a zenith angle accuracy of $\sim 2.8^{\circ}$.

8.4. Theoretical burst spectra

The size spectrum of bursts has been measured in the range 20 - 1500 particles. In order to calculate the expected burst spectrum, it is necessary to know the flux of primaries incident on the iron. Bursts are principally produced by protons, neutrons and pions, with some contribution from electromagnetic interactions of muons. Although the flux of muons at sea level is larger than either that of protons or pions, the number of bursts produced by muons is smaller due to the lower interaction cross-section. The sea level spectra of protons, pions and muons in both the vertical and inclined directions will be considered in the following sections.

8.4.1 Acceptance functions

The differential aperture of the sensitive volume (dimensions $\bar{x}$, $\bar{y}$ $(>\bar{x})$ and $\bar{z}$ with the primary flux incident on the $\bar{x}$ - $\bar{y}$ plane, has been evaluated from the following integral:

$$\frac{d\Omega}{d\theta} = \sin\theta\cos\theta \int_{\phi_1}^{\phi_2} (\bar{x}\bar{y} - \bar{x}\bar{z}\tan\theta\sin\phi - \bar{y}\bar{z}\tan\theta\cos\phi + \bar{z}^2\tan^2\theta\sin\phi\cos\phi)d\phi$$

with the limits given by

Range	ϕ_2	ϕ_1
$0 \leq \theta \leq \tan^{-1}(\bar{x}/\bar{z})$	$\frac{\pi}{2}$	0
$\tan^{-1}(\bar{x}/\bar{z}) \leq \theta \leq \tan^{-1}(\bar{y}/\bar{z})$	$\frac{\pi}{2}$	$\cos^{-1}(\bar{x}\cot\theta/\bar{z})$
$\tan^{-1}(\bar{y}/\bar{z}) \leq \theta \leq \tan^{-1}(\sqrt{\bar{x}^2+\bar{y}^2}/\bar{z})$	$\sin^{-1}(\bar{y}\cot\theta/\bar{z})$	$\cos^{-1}(\bar{x}\cot\theta/\bar{z})$

where θ is the true zenith angle, and ϕ is azimuth angle measured from the x-axis.

The differential aperture as a function of projected zenith angle θ_o has been evaluated from the following expressions given by Pattison (1965) for a primary flux following the power law $I_\theta = I_o \cos^n\theta_o$:

for $n > 1$

$$\left(\frac{d\Omega}{d\theta_o}\right)_n = \frac{K\bar{z}^{n+1}\cos^n\theta_o}{n(n+2)} \left(A_-^{-n/2} - A_+^{-n/2}\right) + \frac{n+1}{n+2}\cos^2\theta_o \left(\frac{d\Omega}{d\theta_o}\right)_{n-2}$$

with $K = 4\, I_o(\bar{y} - \bar{z}\tan\theta_o)$; $A_- = \bar{z}^2$; $A_+ = \bar{z}^2 + \bar{x}^2\cos^2\theta_o$

8.4.2 Cosmic ray spectra

The data of Zatsepin et al have been used in conjunction with the O.P.W. spectrum to determine the flux of muons in inclined directions, for energies > 100 GeV. For muons with energy in the range 10-100 GeV, the data of Allen et al has been employed. The intensities of muons at sea level with energies in the range 10-

10,000 GeV are given in Table 8.1, for θ in the zenith angle range 0°-60°.

The pion production spectrum has been derived by Osborne (1965) under the assumption that pions are the sole source of muons. Allowance has been made for loss of muons by μ-e decay, and energy loss by ionisation in the atmosphere. The best estimate of the spectrum is:

$$F_{\pi}^{\pm}(E_{\pi}^{\pm}) = 1.76 \times 10^{-1} \; E_{\pi}^{-2.65} \; cm^{-2} sec^{-1} sterad^{-1} \; GeV^{-1}$$

for $3.5 \leq E_{\pi}^{\pm} \leq 2000$ GeV.

The spectrum has been extrapolated up to 10,000 GeV, and is shown in figure 8.8.

An estimate of the primary spectrum has been made by Brooke et al. (1964a). It is possible to evaluate the intensity of the primary particles by examining the dependence of the energy spectra of cosmic ray protons and muons at sea level, assuming a particular model for the interaction of high energy nucleons. The O.P.W. spectrum was used in the calculations, together with the sea level proton spectrum measured by Brooke et al (1964b). The form of analysis was to take a trial spectrum of primary nucleons, and to determine a value of K_T, the fraction of energy lost by the high energy nucleon in a collision with an air nucleus, necessary to give the measured sea level proton spectrum, and the value of K_{π}, the fraction of energy appearing as pions, necessary to give the pion production spectrum, in turn derived from the sea level muon

Units: $cm.^{-2}$ $sec.^{-1}$ $sterad.^{-1}$ $Gev.^{-1}$

E_μ Gev. \ θ	0°	10°	20°	30°	40°	50°	60°
10.0	1.07_{10}-04	1.05_{10}-04	1.01_{10}-04	9.40_{10}-05	8.40_{10}-05	7.10_{10}-05	5.15_{10}-05
15.0	4.36_{10}-05	4.28_{10}-05	4.12_{10}-05	3.97_{10}-05	3.68_{10}-05	3.22_{10}-05	2.62_{10}-05
20.0	2.20_{10}-05	2.18_{10}-05	2.11_{10}-05	2.03_{10}-05	1.92_{10}-05	1.79_{10}-05	1.50_{10}-05
30.0	7.85_{10}-06	7.83_{10}-06	7.75_{10}-06	7.65_{10}-06	7.55_{10}-06	7.35_{10}-06	6.80_{10}-06
50.0	1.94_{10}-06	1.93_{10}-06	1.92_{10}-06	1.91_{10}-06	1.90_{10}-06	1.88_{10}-06	1.80_{10}-06
70.0	7.23_{10}-07	7.22_{10}-07	7.21_{10}-07	7.20_{10}-07	7.17_{10}-07	7.03_{10}-07	6.80_{10}-07
100.0	2.50_{10}-07	2.51_{10}-07	2.55_{10}-07	2.60_{10}-07	2.65_{10}-07	2.75_{10}-07	2.80_{10}-07
150.0	7.26_{10}-08	7.32_{10}-08	7.50_{10}-08	7.77_{10}-08	8.17_{10}-08	8.71_{10}-08	9.29_{10}-08
200.0	2.97_{10}-08	3.00_{10}-08	3.10_{10}-08	3.27_{10}-08	3.53_{10}-08	3.86_{10}-08	4.28_{10}-08
300.0	8.18_{10}-09	8.27_{10}-09	8.56_{10}-09	8.90_{10}-09	9.82_{10}-09	1.08_{10}-08	1.22_{10}-08
500.0	1.46_{10}-09	1.48_{10}-09	1.53_{10}-09	1.64_{10}-09	1.78_{10}-09	2.00_{10}-09	2.32_{10}-09
700.0	4.31_{10}-10	4.37_{10}-10	4.52_{10}-10	4.87_{10}-10	5.34_{10}-10	6.08_{10}-10	7.15_{10}-10
1000.0	1.15_{10}-10	1.17_{10}-10	1.21_{10}-10	1.31_{10}-10	1.46_{10}-10	1.68_{10}-10	2.02_{10}-10
1500.0	2.79_{10}-11	2.83_{10}-11	2.95_{10}-11	3.19_{10}-11	3.57_{10}-11	4.13_{10}-11	5.05_{10}-11
2000.0	9.38_{10}-12	1.00_{10}-11	1.05_{10}-11	1.14_{10}-11	1.27_{10}-11	1.48_{10}-11	1.84_{10}-11
3000.0	2.30_{10}-12	2.34_{10}-12	2.44_{10}-12	2.65_{10}-12	2.99_{10}-12	3.47_{10}-12	4.32_{10}-12
5000.0	3.28_{10}-13	3.34_{10}-13	3.49_{10}-13	3.79_{10}-13	4.30_{10}-13	5.02_{10}-13	6.30_{10}-13
7000.0	7.43_{10}-14	7.57_{10}-14	7.94_{10}-14	8.60_{10}-14	9.77_{10}-14	1.14_{10}-13	1.44_{10}-13

Table 8.1. The intensity of muons at sea level as a function of zenith angle θ for muons with energy in the range 10-10,000 Gev.

Units: $cm.^{-2}$ $sec.^{-1}$ $sterad.^{-1}$ $Gev.^{-1}$

E_p Gev. \ θ	0°	10°	20°	30°	40°	50°	60°
10.0	5.26_{10}-07	4.64_{10}-07	3.12_{10}-07	1.49_{10}-07	4.38_{10}-08	5.71_{10}-09	1.54_{10}-10
15.0	1.85_{10}-07	1.63_{10}-07	1.10_{10}-07	5.25_{10}-08	1.54_{10}-08	2.01_{10}-09	5.39_{10}-11
20.0	8.80_{10}-08	7.76_{10}-08	5.22_{10}-08	2.50_{10}-08	7.33_{10}-09	9.55_{10}-10	2.57_{10}-11
30.0	3.09_{10}-08	2.73_{10}-08	1.83_{10}-08	8.78_{10}-09	2.57_{10}-09	3.36_{10}-10	9.02_{10}-12
50.0	8.28_{10}-09	7.30_{10}-09	4.91_{10}-09	2.35_{10}-09	6.89_{10}-10	8.98_{10}-11	2.42_{10}-12
70.0	3.47_{10}-09	3.06_{10}-09	2.06_{10}-09	9.86_{10}-10	2.89_{10}-10	3.77_{10}-11	1.01_{10}-12
100.0	1.38_{10}-09	1.22_{10}-09	8.21_{10}-10	3.93_{10}-10	1.15_{10}-10	1.50_{10}-11	4.04_{10}-13
150.0	4.86_{10}-10	4.29_{10}-10	2.88_{10}-10	1.38_{10}-10	4.05_{10}-11	5.28_{10}-12	1.42_{10}-13
200.0	2.32_{10}-10	2.04_{10}-10	1.37_{10}-10	6.57_{10}-11	1.93_{10}-11	2.51_{10}-12	6.75_{10}-14
300.0	8.13_{10}-11	7.17_{10}-11	4.82_{10}-11	2.31_{10}-11	6.77_{10}-12	8.82_{10}-13	2.37_{10}-14
500.0	2.18_{10}-11	1.92_{10}-11	1.29_{10}-11	6.18_{10}-12	1.81_{10}-12	2.36_{10}-13	6.35_{10}-15
700.0	9.14_{10}-12	8.06_{10}-12	5.42_{10}-12	2.59_{10}-12	7.61_{10}-13	9.92_{10}-14	2.67_{10}-15
1000.0	3.64_{10}-12	3.21_{10}-12	2.16_{10}-12	1.03_{10}-12	3.03_{10}-13	3.95_{10}-14	1.06_{10}-15
1500.0	1.28_{10}-12	1.13_{10}-12	7.59_{10}-13	3.63_{10}-13	1.06_{10}-13	1.39_{10}-14	3.73_{10}-16
2000.0	6.09_{10}-13	5.37_{10}-13	3.61_{10}-13	1.73_{10}-13	5.07_{10}-14	6.61_{10}-15	1.78_{10}-16
3000.0	2.14_{10}-13	1.89_{10}-13	1.27_{10}-13	6.07_{10}-14	1.78_{10}-14	2.32_{10}-15	6.24_{10}-17
5000.0	5.73_{10}-14	5.05_{10}-14	3.40_{10}-14	1.63_{10}-14	4.77_{10}-15	6.21_{10}-16	1.67_{10}-17
7000.0	2.40_{10}-14	2.12_{10}-14	1.43_{10}-14	6.82_{10}-15	2.00_{10}-15	2.61_{10}-16	7.01_{10}-18

Table 8.2. The intensity of protons at sea level as a function of zenith angle θ for protons with energy in the range 10-10,000 Gev.

Units: $cm.^{-2}$ $sec.^{-1}$ $sterad.^{-1}$ $Gev.^{-1}$

E_π Gev. \ θ	0°	10°	20°	30°	40°	50°	60°
10.0	5.79_{10}-08	5.11_{10}-08	3.45_{10}-08	1.66_{10}-08	4.89_{10}-09	6.43_{10}-10	1.74_{10}-11
15.0	2.89_{10}-08	2.55_{10}-08	1.72_{10}-08	8.30_{10}-09	2.46_{10}-09	3.24_{10}-10	8.83_{10}-12
20.0	1.75_{10}-08	1.54_{10}-08	1.04_{10}-08	5.04_{10}-09	1.50_{10}-09	1.98_{10}-10	5.42_{10}-12
30.0	8.49_{10}-09	7.51_{10}-09	5.09_{10}-09	2.47_{10}-09	7.36_{10}-10	9.80_{10}-11	2.70_{10}-12
50.0	3.31_{10}-09	2.93_{10}-09	1.99_{10}-09	9.73_{10}-10	2.93_{10}-10	3.95_{10}-11	1.11_{10}-12
70.0	1.73_{10}-09	1.54_{10}-09	1.05_{10}-09	5.15_{10}-10	1.56_{10}-10	2.13_{10}-11	6.03_{10}-13
100.0	8.50_{10}-10	7.54_{10}-10	5.17_{10}-10	2.55_{10}-10	7.82_{10}-11	1.08_{10}-11	3.11_{10}-13
150.0	3.64_{10}-10	3.23_{10}-10	2.23_{10}-10	1.11_{10}-10	3.44_{10}-11	4.82_{10}-12	1.42_{10}-13
200.0	1.94_{10}-10	1.73_{10}-10	1.19_{10}-10	5.97_{10}-11	1.87_{10}-11	2.66_{10}-12	7.98_{10}-14
300.0	7.72_{10}-11	6.88_{10}-11	4.77_{10}-11	2.41_{10}-11	7.64_{10}-12	1.11_{10}-12	3.41_{10}-14
500.0	2.29_{10}-11	2.05_{10}-11	1.43_{10}-11	7.27_{10}-12	2.34_{10}-12	3.45_{10}-13	1.10_{10}-14
700.0	1.00_{10}-11	8.97_{10}-12	6.27_{10}-12	3.21_{10}-12	1.04_{10}-12	1.55_{10}-13	5.02_{10}-15
1000.0	4.11_{10}-12	3.67_{10}-12	2.57_{10}-12	1.32_{10}-12	4.30_{10}-13	6.50_{10}-14	2.14_{10}-15
1500.0	1.46_{10}-12	1.31_{10}-12	9.18_{10}-13	4.73_{10}-13	1.55_{10}-13	2.36_{10}-14	7.87_{10}-16
2000.0	6.98_{10}-13	6.24_{10}-13	4.38_{10}-13	2.26_{10}-13	7.43_{10}-14	1.14_{10}-14	3.82_{10}-16
3000.0	2.43_{10}-13	2.18_{10}-13	1.53_{10}-13	7.93_{10}-14	2.61_{10}-14	4.01_{10}-15	1.36_{10}-16
5000.0	6.40_{10}-14	5.73_{10}-14	4.03_{10}-14	2.09_{10}-14	6.90_{10}-15	1.06_{10}-15	3.64_{10}-17
7000.0	2.64_{10}-14	2.37_{10}-14	1.67_{10}-14	8.64_{10}-15	2.86_{10}-15	4.42_{10}-16	1.51_{10}-17

Table 8.3. The intensity of pions at sea level as a function of zenith angle θ for pions with energy in the range 10-10,000 Gev.

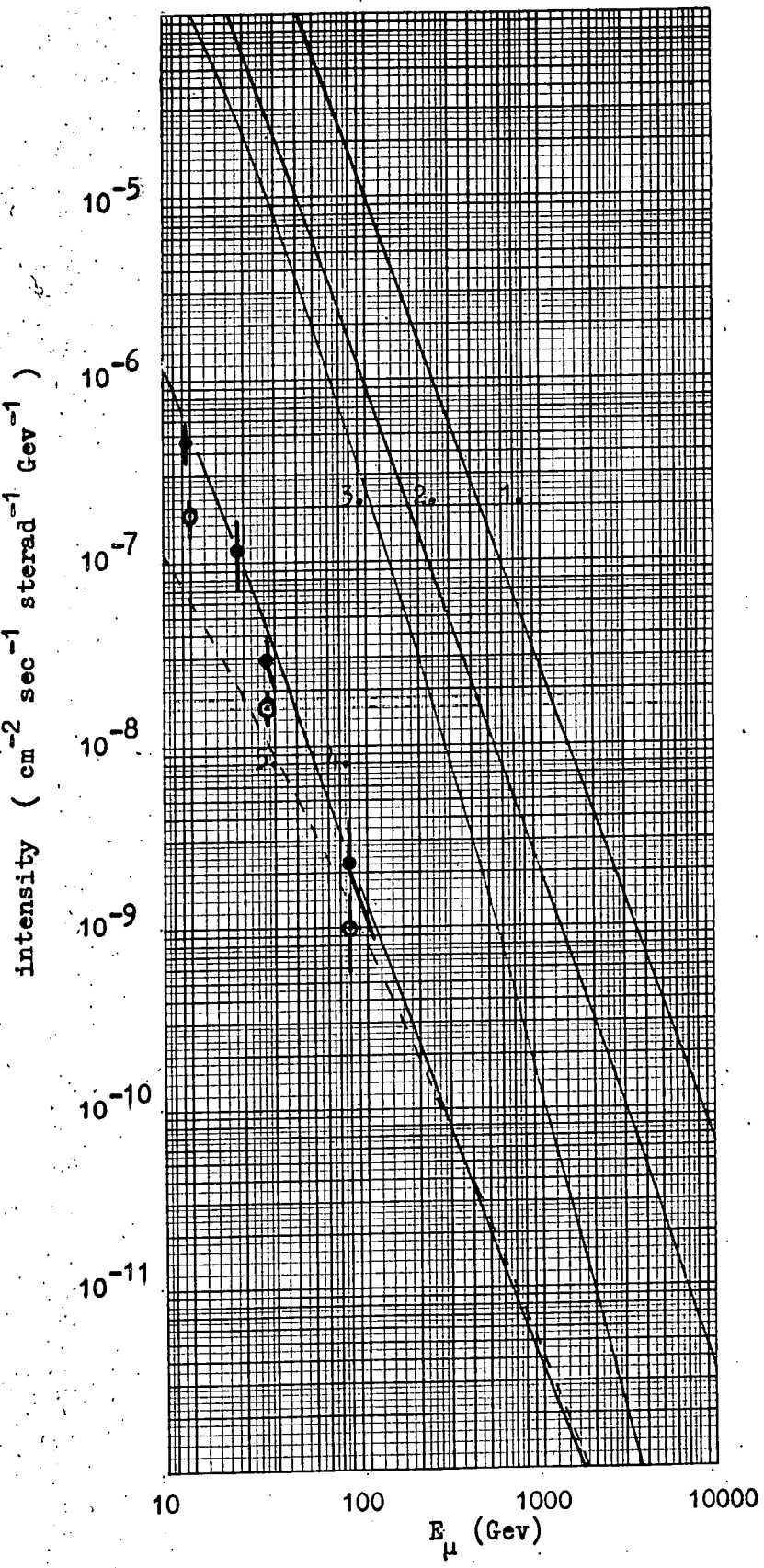

Figure 8.8. Cosmic ray spectra.
1. primary proton spectrum.
2. pion production spectrum.
3. sea level muon spectrum.
4. sea level proton spectrum.
5. sea level pion spectrum.

spectrum. The primary spectrum was then relaxed until the condition $K_\tau - K_\pi = 0.12$ was satisfied, this value being the best estimate from the experimental data available. The empirical relation of Cocconi et al. (1961) was used to describe the energy distribution of pions resulting from nucleon-light nucleus collisions. The best estimate of the primary spectrum is :

$$I(E_N) = 1.37 \begin{matrix} + 0.82 \\ - 0.47 \end{matrix} \quad E^{-2.58} \quad \text{cm}^{-2}\text{sec}^{-1}\text{ster}^{-1}\text{GeV}^{-1}$$

for $10 \leq E \leq 3 \times 10^4$, with E in units of GeV.

This spectrum is displayed in figure 8.8.

Brooke et al (1964b) have made measurements on the spectrum of protons at sea level using a magnetic spectrograph in conjunction with an I.G.Y. neutron monitor. The proton contribution was determined for each deflection cell by subtracting from the number of positive particles the corresponding number of negative particles multiplied by the positive-negative ratio for muons at that momentum, assuming this to have the same value for pions as for muons. The best estimate of the attenuation length for nucleons in air was $\lambda p = 127 \pm 4$ gm.cm^{-2}, for nucleon energies $\geq$ 2 GeV. This value was derived from the primary nucleon spectrum assuming $K_\tau - K_\pi = 0.12$, and that the neutron intensity at sea level is equal to the proton intensity at the same energy. The proton intensities at various zenith angles have been derived assuming $\lambda p = 127$ gm cm^{-2}, and are tabulated in Table 8.2. for protons in the energy range 10-10,000 GeV. The spectrum of neutrons is

assumed to be identical with that of protons in the energy range considered. The vertical sea level proton spectrum is shown in figure 8.8, together with the measured points of Brooke et al.

The energy spectrum of negative pions in the vertical direction has been measured by Brooke et al. (1964c) using the Durham spectrograph in conjunction with an I.G.Y. neutron monitor. Pions were detected by means of their interaction and subsequent neutron production in the monitor. The experimental measurements representing the total flux of charged pions at sea level are shown in figure 8.8. It was assumed that the positive-negative ratio for pions was unity, because calculations show that the majority of sea level pions are produced in collisions near sea level, where the proton-neutron ratio is unity.

Using the approach of Barrett et al. (1952) the intensity of pions with energy between E and (E+dE) at depth x in the atmosphere, $\pi(E,x)dE$, is related to the intensity of the pion production spectrum, $F(E)dE$, by the equation :

$$\pi(E,x)dE = F(E)dE \exp\left(-\frac{x}{\lambda_\pi}\right) \frac{x}{\lambda_p} \left\{\frac{1}{1+B/E} - \frac{x/\lambda'}{2+B/E} + \frac{1}{2!}\frac{(x/\lambda')^2}{3+B/E} \cdots\right\}$$

where $\frac{1}{\lambda'} = \frac{1}{\lambda_p} - \frac{1}{\lambda_\pi}$ and $B = \frac{mc^2 H}{c\tau_o}$

mc^2 and τ_o are the rest energy and lifetime of the pion respectively, and H is the ratio of atmospheric depth to the density of the air at that depth. λ_π is the pion attenuation length.

Assuming $\lambda_p = \lambda_\pi$, then the intensity of pions, $\pi(E,1030,\theta)$, at sea level and incident at a zenith angle θ, is related to the pion production spectrum by the equation:

$$\pi(E,1030,\theta)dE = F(E)dE. \quad \frac{1030 \sec \theta}{\lambda_p} \cdot \exp\left(-\frac{1030 \sec\theta}{\lambda_p}\right)\left\{\frac{1}{1+B\sec\theta/E}\right\} \quad ..8.1.$$

This equation has been evaluated for pion energies in the range 10 - 10,000 GeV, and the intensities are shown in Table 8.3 for θ in the zenith angle range 0° - 60°. Values of H corresponding to the mean depth of production for pions of a given energy have been used. The predicted vertical spectrum is shown in figure 8.8, together with the measured points of Brooke et al (1964c). The discrepancy at 10 GeV (a factor of 3) cannot be accounted for by varying λ_π, because equation 8.1 is very insensitive to variations in λ_π, due to the pions being produced at such low altitudes.

8.4.3 Predicted burst spectra

Cascades in iron have been considered in Chapter 6, and the cascade curves developed for use with liquid paraffin scintillation counters in the horizontal burst experiment have been used in the vertical burst analysis. Typical curves for electron-photon cascades are shown in Figure 6.5. The curves in figure 6.6 have been used for pion induced cascades, assuming an inelasticity of 100% for pion interactions.

(a) $B^{\pm}$ events

Those events which have a track in A and B associated with a

burst in the scintillator are classified as $B^{\pm}$ events. The expected spectrum of bursts has been calculated, assuming the inelasticities of proton and pion collisions to be 50% and 100% respectively, and is shown in figure 8.9. The relative contributions of muons, pions and protons to the total spectrum are indicated. Pions are the dominant primaries for bursts of size > 100 particles but for smaller bursts their contribution is reduced through decay losses in the atmosphere. Protons and muons are of equal importance for small burst sizes.

The distribution of energies of a primary particle giving rise to a $B^{\pm}$ event of size in the range 132 - 264 particles is shown in figure 8.10 for proton, pion and muon primaries. The mean energy of a proton producing a burst in this size range is 173 GeV, whereas the mean pion energy is 93 GeV. The difference arises from the different inelasticities. The figures in parenthesis indicate the relative contributions of each to the total spectrum. Similar distributions for bursts in the size range 1320 - 2640 are shown in figure 8.11.

(b) B^{o} events

Those events which have no track in A and B associated with a burst in the scintillator are classified as B^{o} events. Neutrons are the main producers of such events, but charged particles can simulate B^{o} events by entering the iron from the side and missing A and B, such that the projected zenith angle θ' is within the

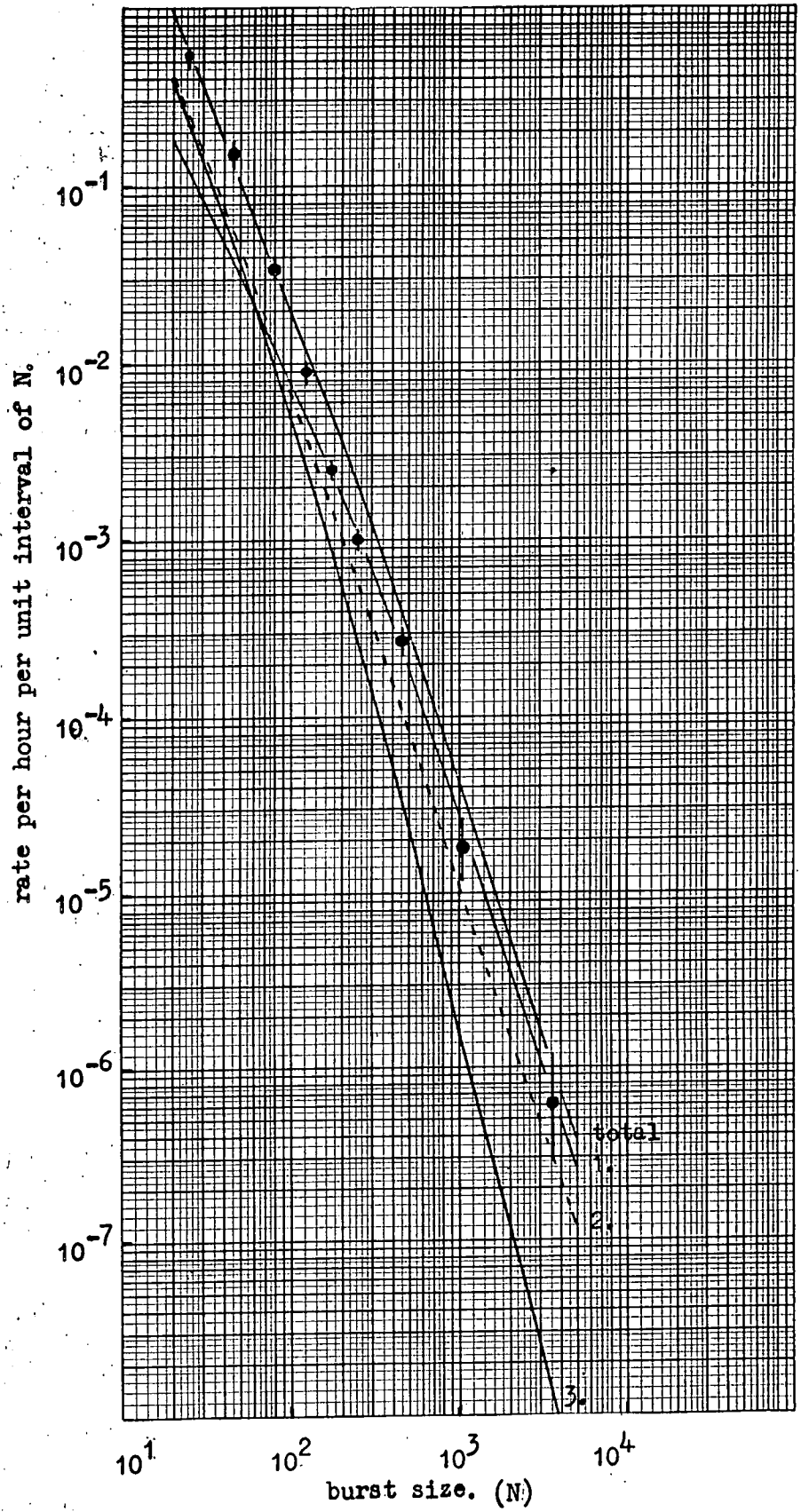

Figure 8.9. The expected spectrum of B^{t} events, showing the relative contributions of the different primaries.
1 - pions; 2 - protons; 3 - muons.

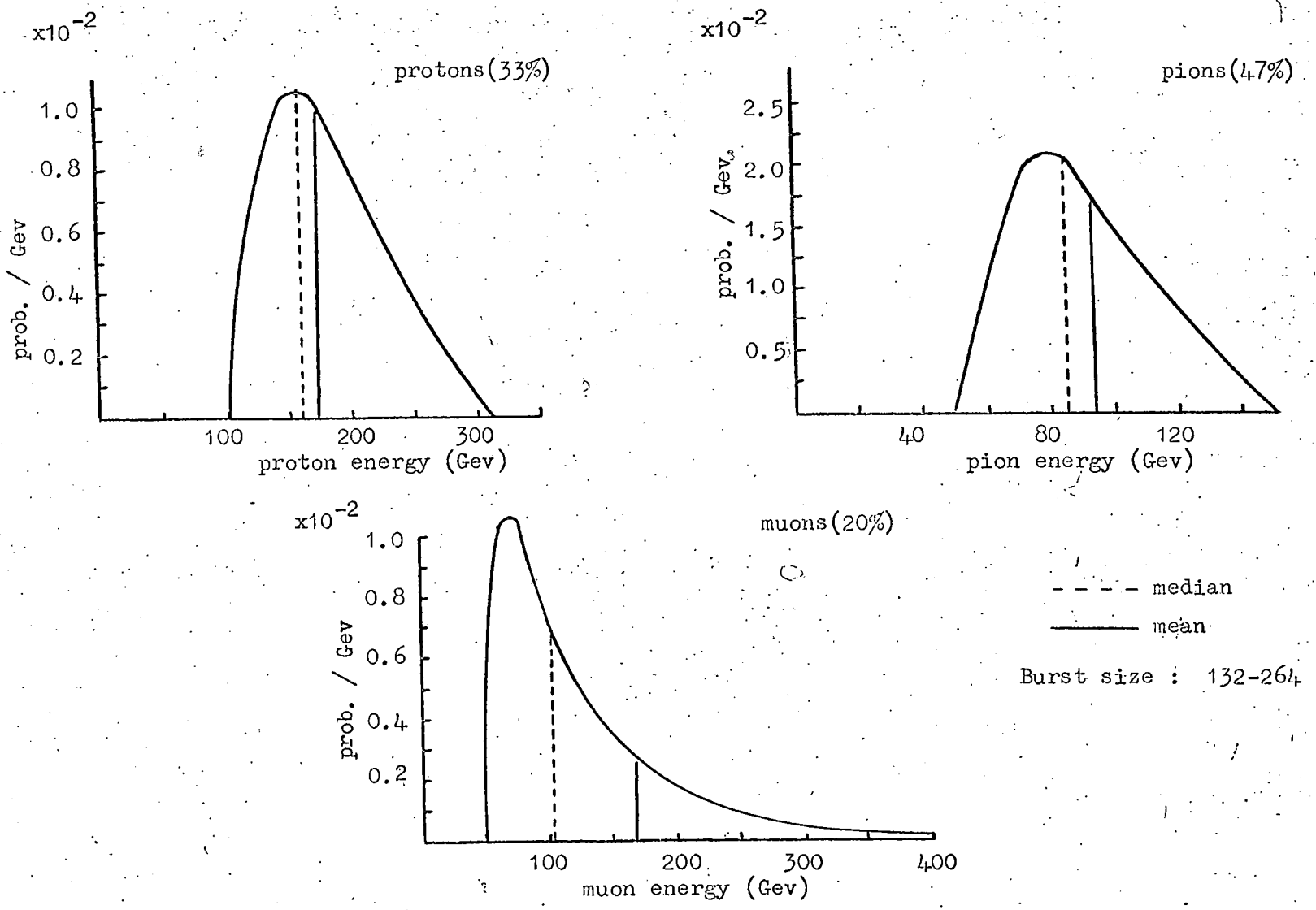

Figure 8.10. Energy distributions of protons, pions and muons producing a burst of size 132-264 particles. The figures in parenthesis are the relative contributions of each type of primary to the total.

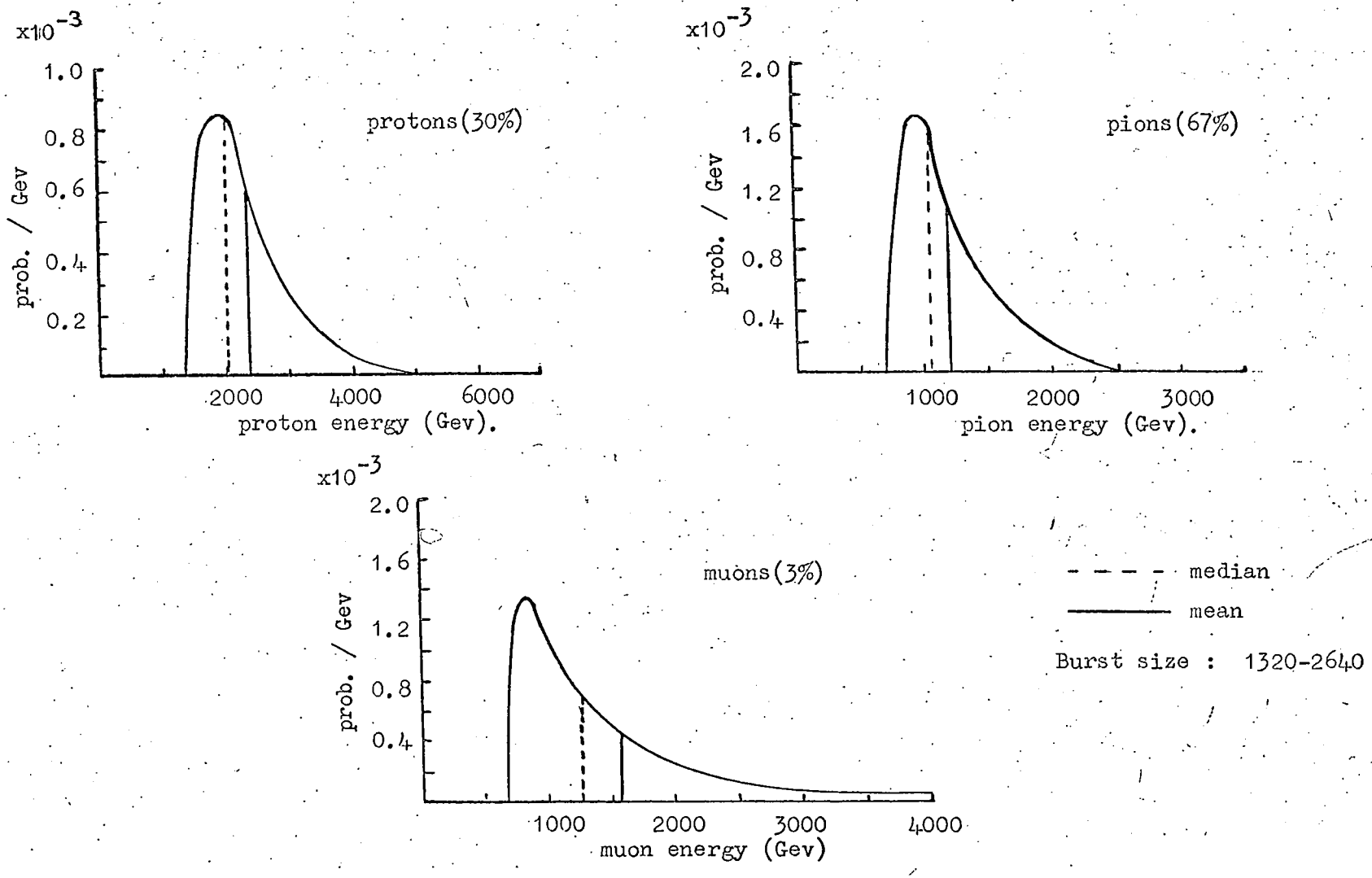

Figure 8.11. Energy distributions of protons, pions and muons producing a burst of size 1320-2640 particles. The figures in parenthesis are the relative contributions of each type of primary to the total.

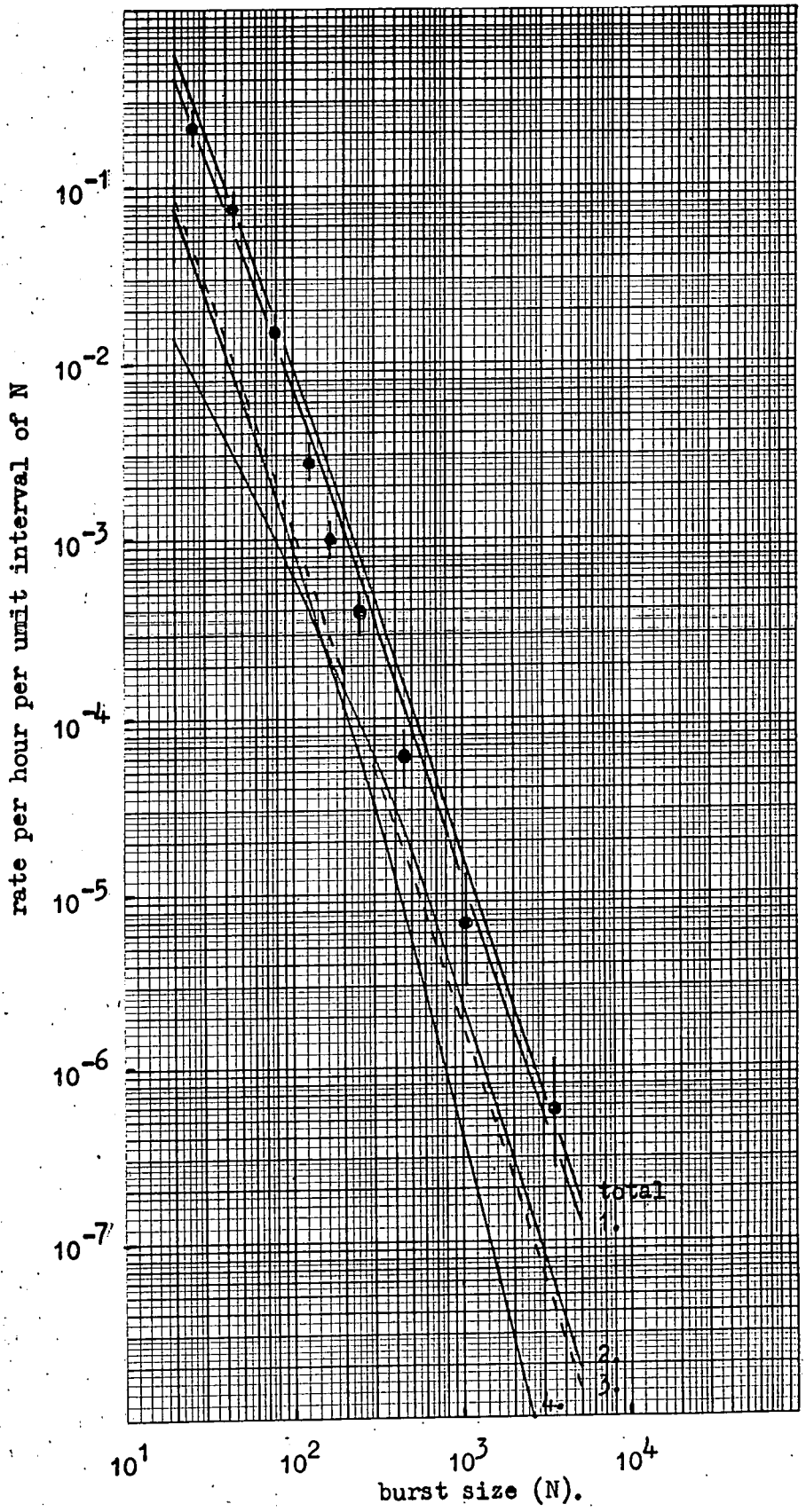

Figure 8.12. The expected spectrum of B^{o} events, showing the relative contributions of the different primaries.
1 - neutrons; 2 - pions; 3 - nucleons; 4 - muons.

accepted geometry. The expected spectrum of B^{o} events is shown in figure 8.12, together with the relative contribution of the different parents. Neutrons are the dominant contributors over the whole range of burst sizes.

8.5 Experimental results

8.5.1 Spectra of $B^{\pm}$ and B^{o} events

The apparatus was run for a total of 702.1 hours, in which time a total of 573 bursts (414 $B^{\pm}$ and 159 B^{o}) were recorded. The measured spectra of $B^{\pm}$ and B^{o} events are shown in figures 8.9 and 8.12 respectively. Corrections for day-to-day variations in pressure have been applied using a Barometer Coefficient of 10% per cm. Hg., and the data have been normalised to a pressure of 76 cms. Hg. The full lines are the total predicted spectra. Although the statistics are rather limited, especially for B^{o} events, agreement between prediction and measurement is good for burst sizes < 100 particles. However, at larger burst sizes there is a systematic difference between theory and experiment in both the $B^{\pm}$ and B^{o} spectra, the predicted spectra being larger than actually measured.

8.5.2 Angular distributions

The angular distributions of the measured $B^{\pm}$ and B^{o} events are plotted as frequency histograms in figure 8.13. A power

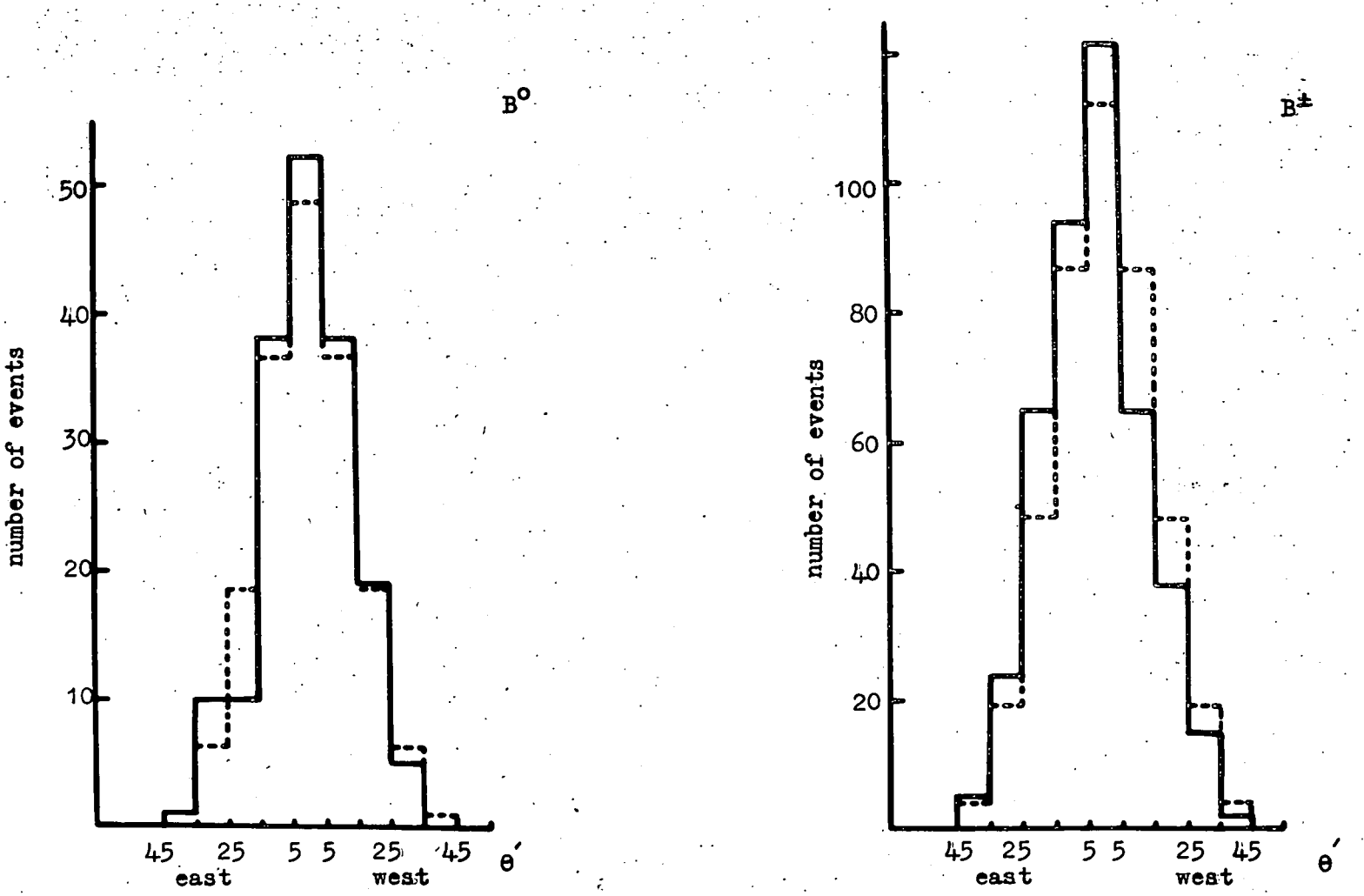

Figure 8.13. Angular distributions of $B^{\pm}$ and B^{o} events. the broken lines are the best fit (minimum χ^2) of theory to the measurements.

law of the form $I_\theta = I_o \cos^n\theta$ has been fitted to the distributions, and the best fit determined by the minimum χ^2 value. The corresponding values of the exponent are:

$$B^{\pm} : n = 3.8 \pm 1.3 \quad ; \quad B^{o} : n = 7.0 \pm 2.3$$

Both distributions contain some contamination from muon induced bursts, and as the muon spectrum decreases relatively slowly with increasing θ, a small contribution from muons will effect the exponent considerably. Allowance has been made for muons, and the angular dependence recalculated for each distribution, the best values of the exponent being:

$$B^{\pm} : n = 7.0 \pm 1.7 \quad ; \quad B^{o} : n = 8.7 \pm 2.1$$

These values of the exponent indicate that, after allowance has been made for the muon contamination, the remaining events are due to nuclear-active particles. The mean values of n have been calculated from the angular variation of the pion and proton intensities at sea level, and are 8.15 and 8.65 for pions and protons respectively. Hence the measured values are in agreement with prediction , to within experimental error.

8.5.3 Lateral distribution of bursts

In the analysis of the films, the mean numbers of tubes flashed in trays C and D were noted, these being denoted by $\bar{N}_c$ and $\bar{N}_d$ respectively. $\bar{N}_{cd}$ has been plotted as a function of burst size in a 'dot' distribution, and is shown in figure 8.14. The

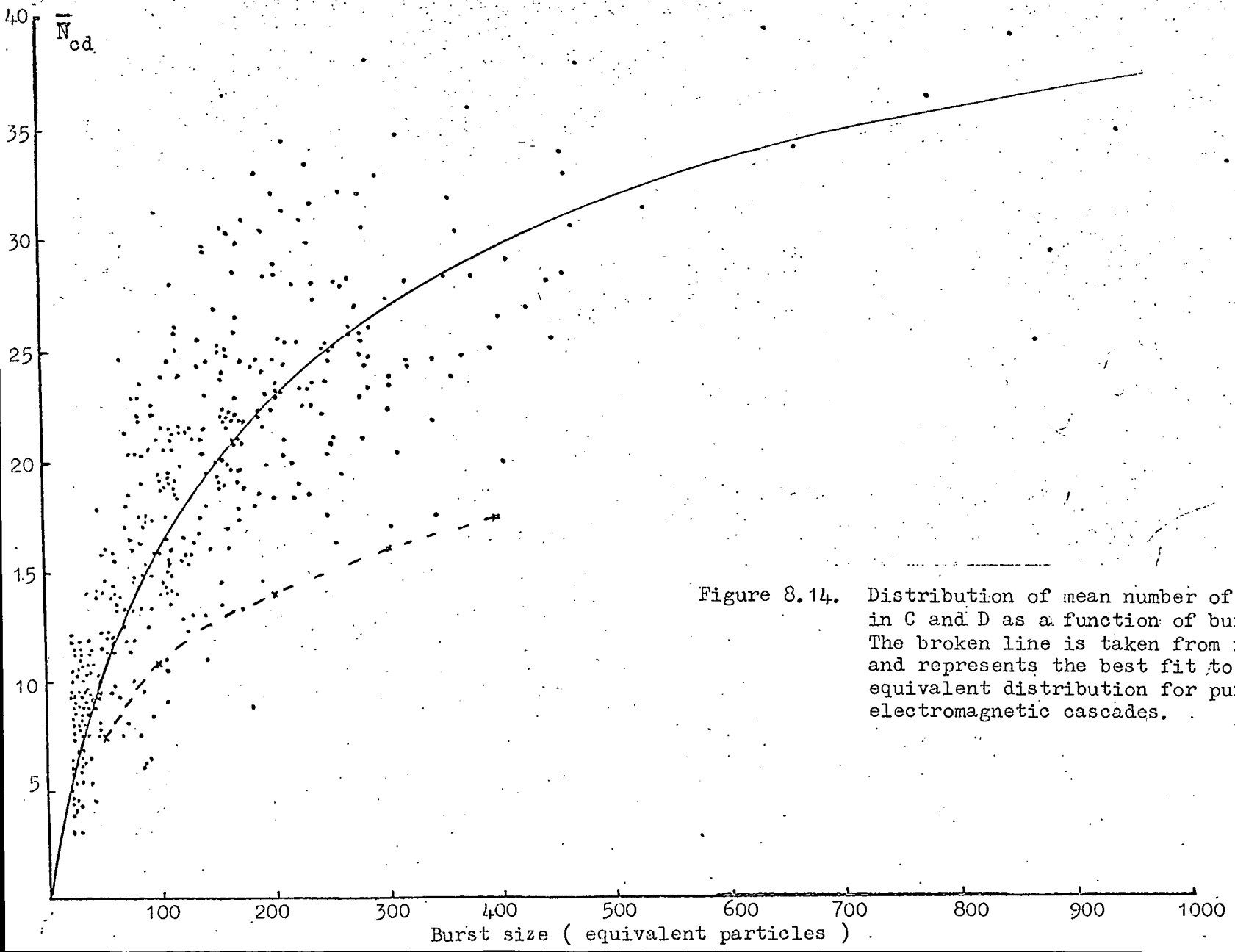

Figure 8.14. Distribution of mean number of flashes in C and D as a function of burst size. The broken line is taken from figure 6.27, and represents the best fit to the equivalent distribution for pure electromagnetic cascades.

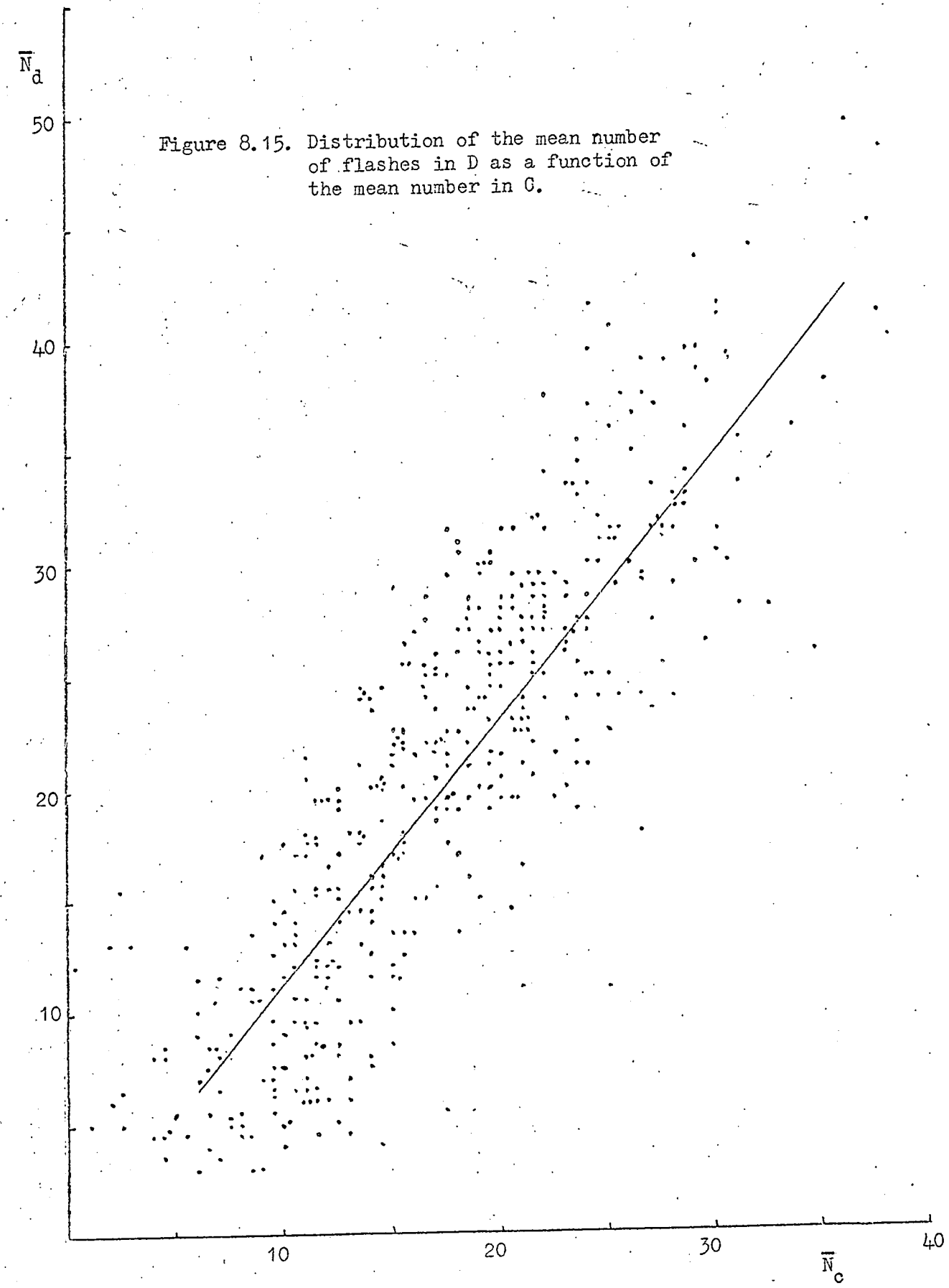

Figure 8.15. Distribution of the mean number of flashes in D as a function of the mean number in C.

full line represents the mean variation of the lateral spread with burst size. Also shown as a broken line is the corresponding variation determined for pure electromagnetic cascades in the horizontal burst experiment. There is a considerable discrepancy between the two measurements, the lateral spread of a burst measured in the vertical experiment being larger than that of the same burst size measured in the horizontal experiment. This is probably caused by the different nature of the bursts. Those measured in the horizontal experiment were mainly electromagnetic in nature, originating from either a photon or an electron. However the vertical bursts are thought to be predominantly pion induced, and the transverse momentum of the pions will tend to broaden the lateral distribution of the burst. Figure 8.15 is a plot of $\overline{N}_d$ against $\overline{N}_c$, and shows the same fanning-out characteristic observed in the horizontal burst experiment.

8.5.4 Accompanied events

Some events contain tracks in A and B which are not associated with the burst, but accompany the primary particle producing the burst. Typical examples are shown in figure 8.16. The upper photograph is a $B^{\pm}$ event accompanied by two other tracks in A and B. A B^{o} event with two parallel tracks in A and B is illustrated in the lower photograph. An accompanying track is defined as ≥ 3 flashes in a line.

a.

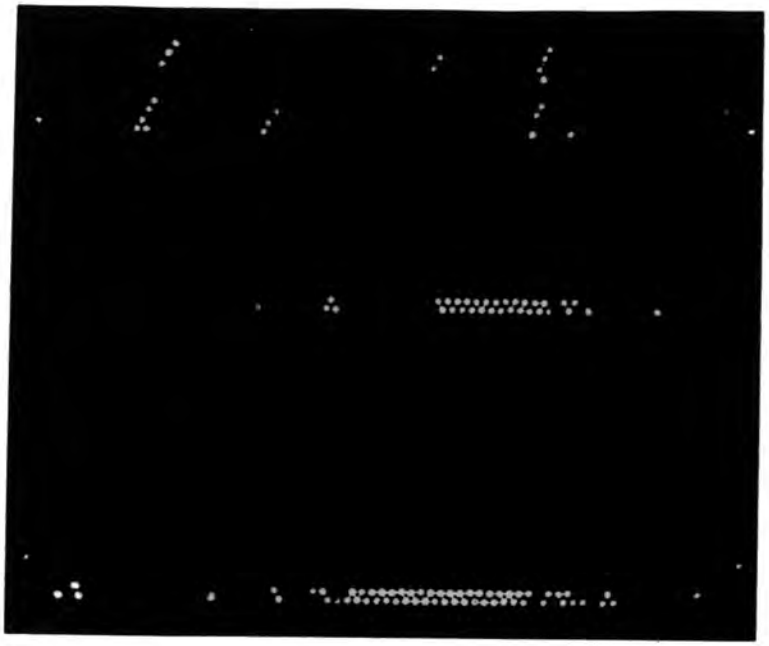

b.

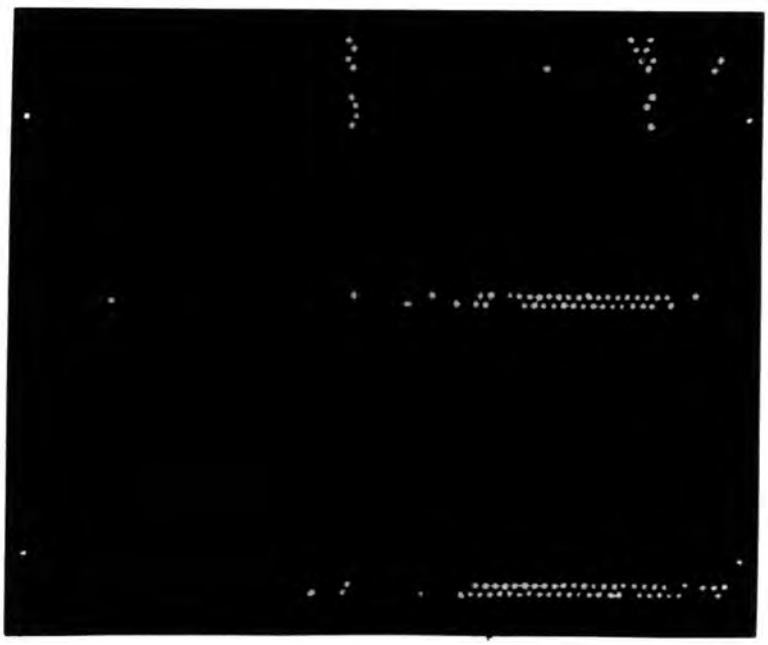

Figure 8.16. Accompanied bursts.

a. $B^{\pm}$ N_s=164 particles. θ=0.7°W. Acc=2 tracks.

b. B^{o} N_s=310 particles. θ=6.5°W. Acc=2 tracks.

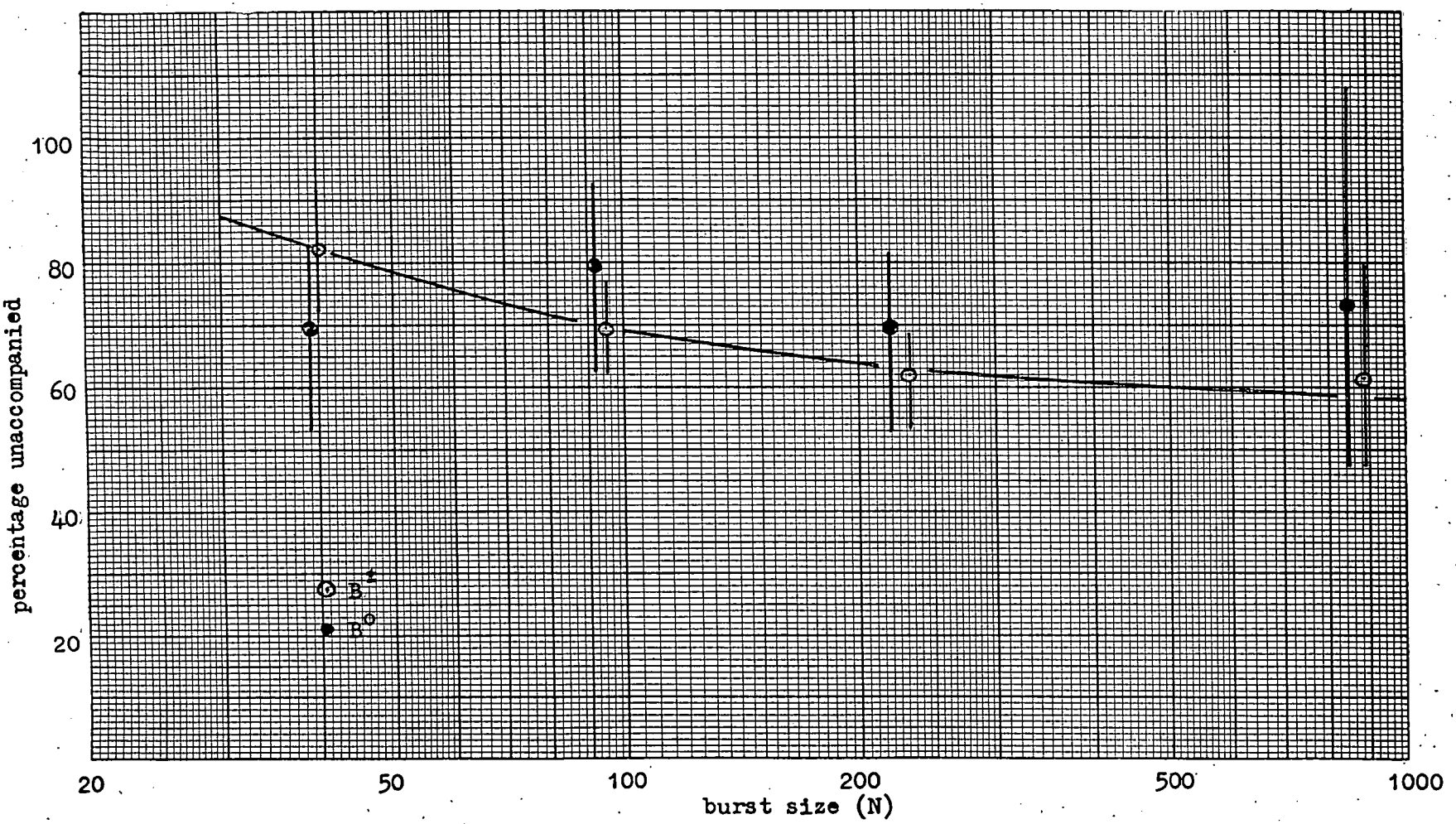

Figure 8.17. Percentage of bursts accompanied by ≤5 flashes in A and B as a function of burst size.

a.

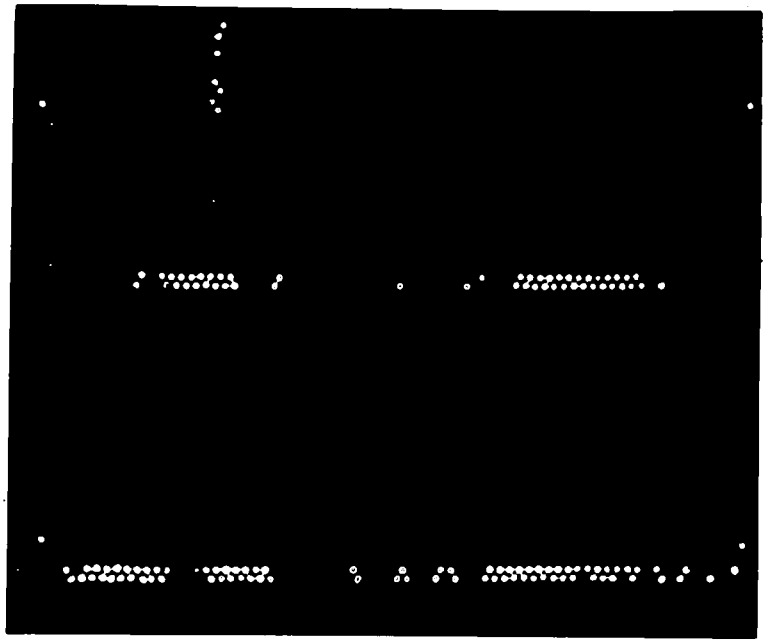

b.

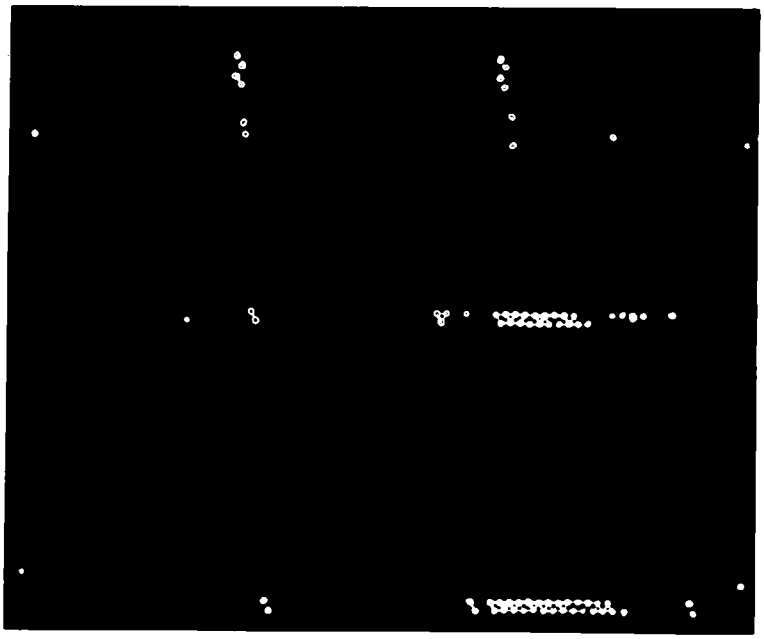

Figure 8.18. Unusual events.

a. Double burst.

b. N_s=52.5 particles. θ=4.4°E. Accompanied by a penetrating particle, probably a muon.

The mean number of spurious flashes in trays A and B is $(0.86 \,^{+\,0.98}_{-\,0.86})$ per trigger. This value was determined by triggering the trays at random using a pulse generator. An unaccompanied event is defined as containing ≤ 5 flashes in A and B unassociated with the burst. A plot of the percentage of bursts which are produced by unaccompanied primaries is shown in figure 8.17 as a function of burst size for $B^{\pm}$ and B^{o} events. The fraction of unaccompanied primaries decreased from a value of 80% at a burst size of 40 particles to 58% at 900 particles. Although the statistics are poor, there appears to be no significant difference between the accompaniment of $B^{\pm}$ or B^{o} events. The degree of accompaniment was measured over an area of 1.3 m^2.

The upper photograph in figure 8.18 shows a neutral burst accompanied by one track in A and B. The second particle also gives rise to a burst in C and D, and the burst in D shows some structure. The event can be described as a neutron accompanied by a proton or charged pion. The lower photograph shows a $B^{\pm}$ event accompanied by a penetrating particle, probably a muon.

8.5.5 Photography rate

Events were selected by demanding only a large pulse from the scintillation counter. The discriminator was biassed at, say 100 particles, and all events producing more than 100 particles in the scintillator were accepted. Subsequent scanning of the films enabled

the $B^{\pm}$ and B^{o} events to be picked out. However, with such a free selection criterion, the ratio of useful events to the total number of exposures becomes important. The integral photography rate as a function of burst size is shown in figure 8.19, together with the total spectrum of $B^{\pm}$ and B^{o} events. If the discriminator is set at 200 particles, 1/5.5 frames would be useful, but the ratio decreases to 1/7.6 frames at 20 particles. The non-useful events are principally caused by extensive air showers.

Green et al. (1959) have measured the total counting rate of an unshielded scintillation counter of area 7.3 m^2. This spectrum is displayed in figure 8.19, normalised to an area of 1.2 m^2. Comparison between the Green spectrum and that measured by the vertical burst spectrum shows the efficiency of the iron in shielding the counter.

8.6 Discussion

Figure 8.12 shows that neutrons contribute principally to the expected B^{o} spectrum. Hence it is possible to compare the measured B^{o} spectrum with the proton measurements of Brooke et al (1964b), assuming the neutron spectrum to be the same as that of protons at sea level, and making corrections for the contamination to the measured B^{o} spectrum. The proton measurements of Brooke et al are shown in figure 8.20, together with the predicted sea level neutron spectrum. The corrected B^{o} measurements are plotted in the same figure at the median neutron energies corresponding to the burst

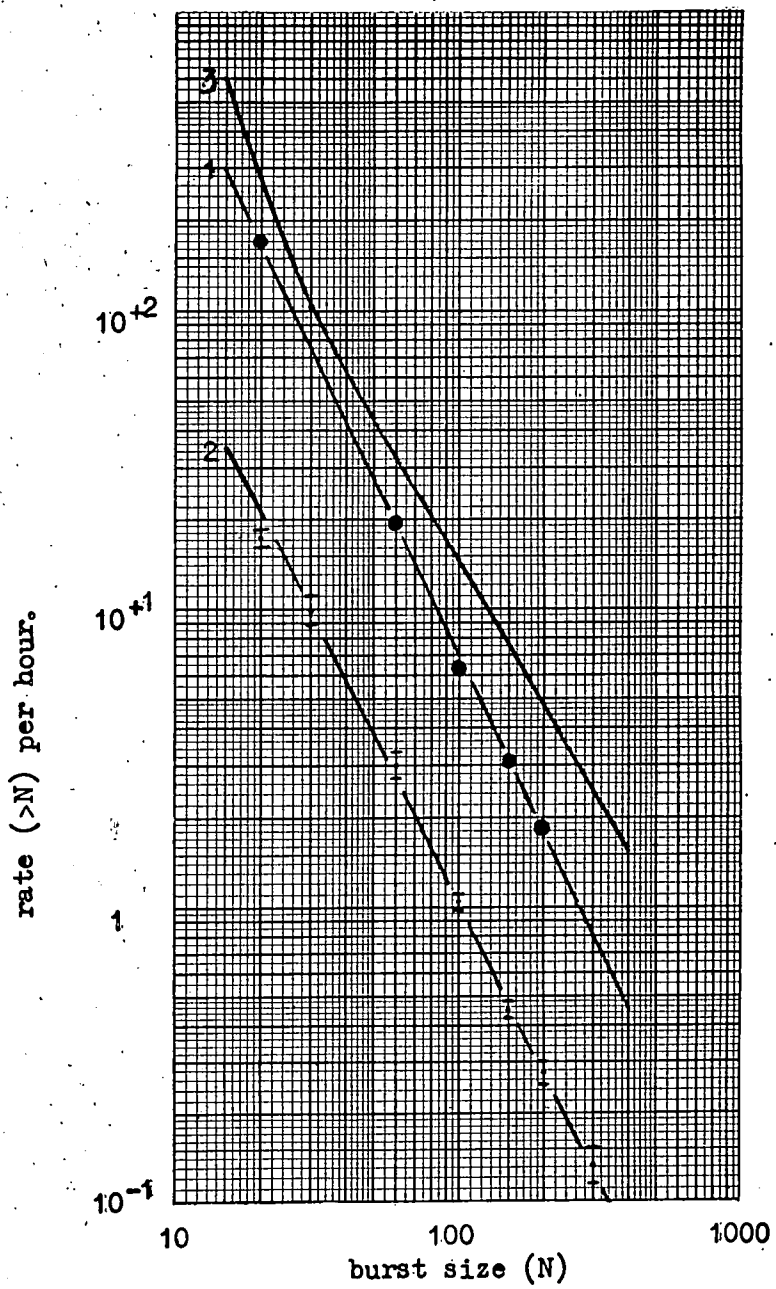

Figure 8.19. Integral counting rate of a scintillator shielded by 20cms. iron.
1. photography rate.
2. total burst spectrum ($B^{\pm}$ and B^{o}).
3. size spectrum measured by Green et al (1959) using an unshielded scintillator of area 7.3m^2. The results have been normalised to an area of 1.2m^2.

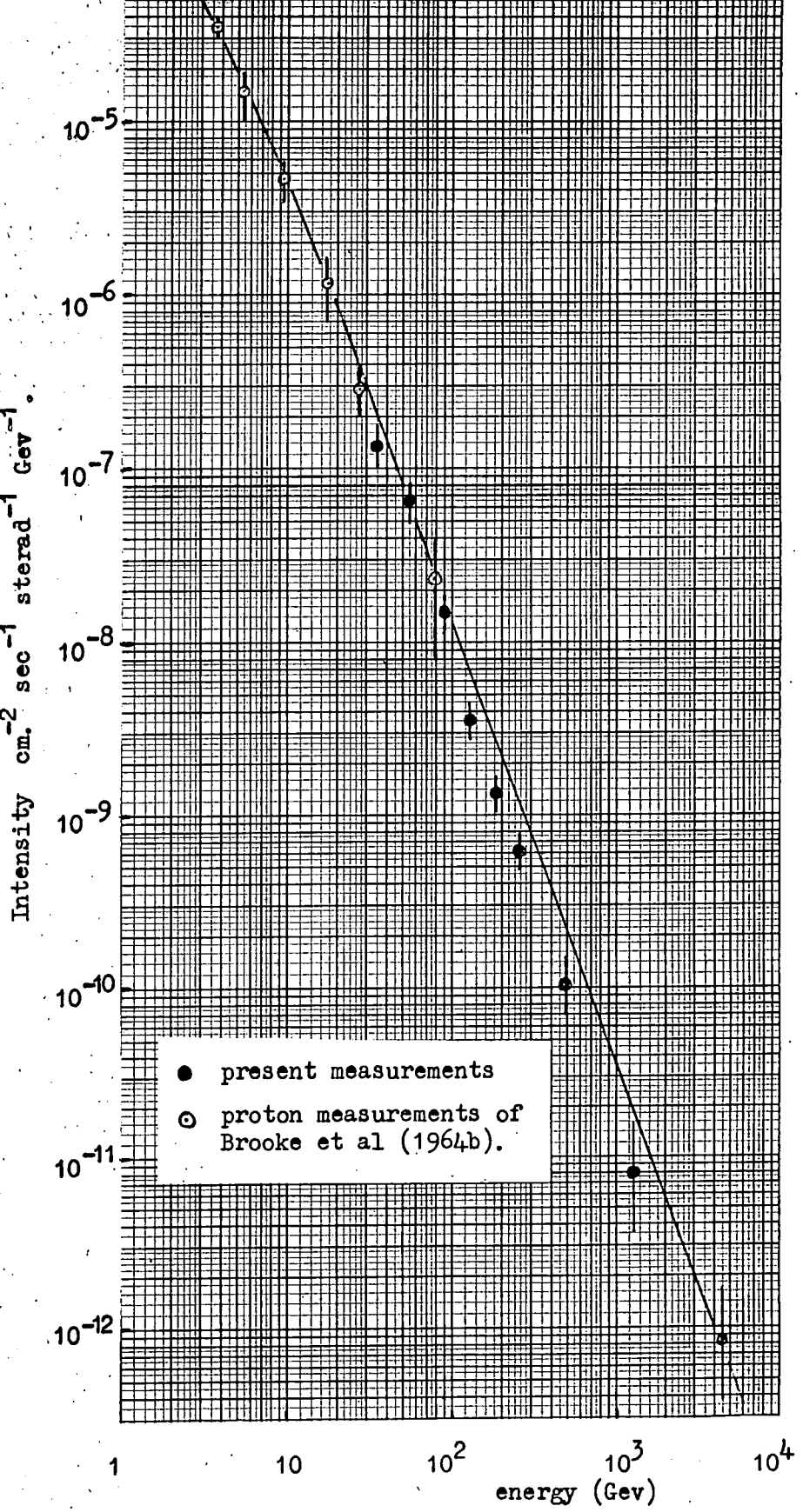

Figure 8.20. The measured neutron flux compared with the predicted spectrum, and the proton measurements of Brooke et al (1964b).

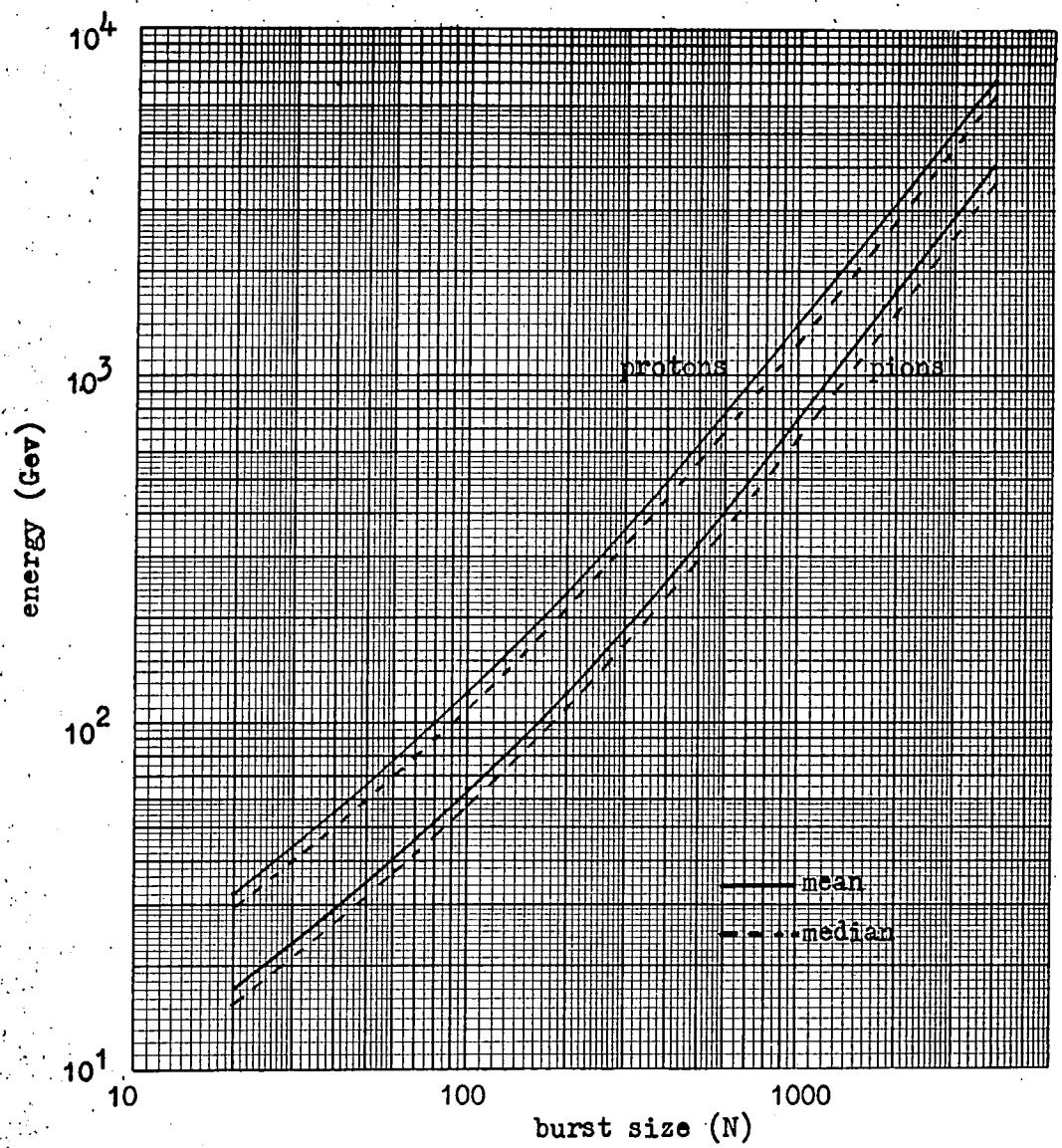

Figure 8.21. Mean and median energies of protons and pions giving rise to a particular burst size. Values of 0.5 and 1.0 were taken for the respective coefficients of inelasticity of protons and pions.

size ranges. The variation of mean and median pion and proton energies with burst size is shown in figure 8.21. Values of $K_p = 0.5$ and $K_\pi = 1.0$ were taken for the respective values of proton and pion coefficients of inelasticity.

For energies < 100 GeV the experimental points are in agreement with the Brooke et al proton measurements, and the predicted spectrum. However, at energies > 100 GeV there is a deviation of the measured points from expectation, the experimental data being a factor ~ 2 lower than the predicted spectrum. An examination of the assumptions made in the theoretical analysis may account for the difference.

The primary spectrum used in the calculations was the best estimate given by Brooke et al (1964a), namely

$$I(E_n) = 1.37^{+0.82}_{-0.47} E^{-2.58} \text{ cm}^{-2} \text{ sec}^{-1} \text{ sterad}^{-1} \text{ GeV}^{-1} \text{ for E}$$

in the range $10 \leq E \text{ (GeV)} \leq 3 \times 10^4$.

Malhotra et al (1966) find the primary spectrum is best represented by

$$I(E_n) = 2.48^{-1.97}_{-1.15} E^{-2.60} \text{ cm}^{-2} \text{ sec}^{-1} \text{ sterad}^{-1} \text{ GeV}^{-1} \text{ for E}$$

in the range $100 \leq E \text{ (GeV)} \leq 6 \times 10^5$.

To account for the discrepancy found in the vertical burst experiment, the Brooke et al primary spectrum would have to be reduced by a factor of more than 2, which is contrary to the findings of Malhotra et al. Although the primary spectrum is not known accurately, it would appear that the Brooke spectrum is an underestimate rather than an overestimate of the primary spectrum, and so it seems unlikely that the discrepancy is due to the spectrum

adopted.

Brooke et al (1964b) found the best value of the proton attenuation length to be $\lambda p = 127 \pm 4$ gm. cm^{-2} in the energy range 2 - 100 GeV. This value was adopted in the vertical burst analysis to cover the entire range of proton energies considered (10-10,000 GeV). However, agreement can be obtained between the measured points and the predicted spectrum by reducing the proton attenuation length to a value of $\lambda p = 117$ gm. cm^{-2} for energies > 100 GeV (sea level), and a similar reduction in the pion attenuation length would result in agreement between the predicted and measured $B^{\pm}$ spectra.

During the scanning of the films, all events were rejected which could not be unambiguously classified into either $B^{\pm}$ and B^{o} categories according to the criteria discussed in §8.3. It was not normally possible to classify events with several (≥ 10) tracks in A and B and containing a burst in C and D. Consequently a bias may have been introduced into the measured spectra. However it is not thought to be a large effect, and is unlikely to account for the discrepancy. Any analysis bias would be expected to increase with burst size, whereas the observed discrepancy is nearly constant for burst sizes $\geq$ 100 particles.

S U_3 predicts a nucleon to be composed of three quarks. If this is correct, it would be feasible for a nucleon to dissociate into its constituent parts in a high energy collision, provided that the energy available was above the threshold for quark

production. Consider an interaction between an energetic primary cosmic ray proton and a nucleon in an air nucleus. γ_c and γ_L, the respective Lorentz factors of the centre of Mass system and the Laboratory system, are related by the equation $\gamma_c^2 = (\gamma_L + 1)/2$. Taking the threshold process to be

$$p + p \rightarrow (q_1 + q_1 + q_2) + (q_1 + q_1 + q_2)$$

where q_1 is the quark of charge + $\frac{2}{3}$, strangeness 0 and q_2 is the quark of charge - $\frac{1}{3}$, strangeness 0, then the energy threshold is 1800 GeV for a quark mass of 10 GeV. This primary energy corresponds to a proton energy of ~ 100 GeV at sea level. Hence, if quarks are produced in the initial interactions of the primary protons, a reduction in the flux of nucleons with energy $\geq$ 100 GeV would occur at sea level.

Assume that quark production occurs in a fraction F of high energy collisions above threshold, and that protons have an inelasticity of 50% in the remaining (1-F) collisions. The observed discrepancy can then be explained using this simple model and it is found that the experimental points are best fitted (minimum χ^2) by a value of F = 18%. However, it should be noted that all values of F give rise to values of χ^2 which are significant at the 5% level. Neutron production by quarks has been ignored.

8.7. Conclusions

This preliminary experiment was performed to test the feasibility of measuring the sea level spectra of nuclear-active particles using a shielded scintillation counter. Bursts produced in the local shielding were used to determine the energy of the primary particles. In principle the spectra of both charged and neutral particles can be measured. A refinement to the present apparatus would be to incorporate flash tubes crossed with those in trays C and D, so that neutrons can be uniquely distinguished from simulated neutral events.

The present results show a discrepancy between the measured burst spectra (both $B^{\pm}$ and B^{o}) and prediction for burst sizes in excess of 100 particles. The most probable explanation is that the value adopted for the proton attenuation length in the theoretical calculations has been overestimated. Agreement can be obtained by reducing the value to $\lambda p = 117$ gm. cm^{-2}, for proton energies (sea level) > 100 GeV. The possibility of the primary spectrum being in error cannot be ruled out entirely, but to reduce it by a factor of 2 would not be in agreement with Brooke et al and Malhotra et al.

The discontinuity is not inconsistent with quark production. Nominally the results indicate a quark mass ~ 10 GeV, and that the high energy nucleons dissociate into their constituent quarks in about 18% of their collisions above threshold. However, all values of F produce values of χ^2 which are significant at the 5%

level, whereas reducing the value of λ_p to 117 gm cm^{-2} produces a χ^2 which is not significant at the 30% level.

CHAPTER 9

SUMMARY

The nearly horizontal muon flux at sea level has been used to study the interactions of high energy (34-520 GeV) muons in an iron absorber producing energy transfers in the range 3-240 GeV. No significant divergence from the theory as predicted by Bhabba (1938) has been found. This result substantiates the findings of Barton et al (1966), but extends the range of energy transfers over which quantum electrodynamics is found to apply. The excess of events reported by Deery and Neddermeyer (1961) is not evident, but this effect would only have been detected if there was a deviation which increased with increasing energy transfer. Although there is a tendancy for the burst spectrum measured in S_2 to fit a theoretical spectrum calculated with the photonuclear cross-section increasing as $E^{\frac{1}{2}}$ for $E \geq 5$ GeV, the same effect is not apparent in the S_1 burst spectrum. The measurements in the relevant region ($\geq$ 100 GeV energy transfer) are not sufficiently reliable statistically to be able to make any quantitative statement.

Measurements on the energy spectra of nuclear-active particles at sea level have been made over the range 20-4000 GeV. A divergence of measurement from theory is apparent in both the charged and neutral burst spectra, occuring at energies > 100 GeV. The observed discontinuity can be taken to support the suggestion of S U_3 that the

proton is a tightly bound system of three charged quarks. This interpretation would indicate a quark mass of about 10 GeV, and also that high energy protons dissociate into their constituent quarks in about 18% of their collisions above threshold (1800 GeV). Assuming the validity of this interpretation, the observed result implies that quarks interact very strongly in the atmosphere, otherwise an abundance of relativistic e/3 and 2e/3 quarks would have been recorded by the various quark telescope experiments which have been performed. An alternative to account for the observed discrepancy is that the attenuation length of protons in the atmosphere be reduced from 127 gm cm^{-2} to a value of 117 gm cm^{-2} for energies $>$ 100 GeV. The latter appears to have more statistical reliability, but the possibility of quark production cannot be ruled out.

ACKNOWLEDGEMENTS

The author wishes to thank Professor G. D. Rochester for the provision of the facilities for this work, and for his interest and support.

He is very grateful to his supervisor, Dr. F. Ashton, for his willing guidance and invaluable help throughout the work. The author would also like to thank Professor A. W. Wolfendale for his interest in the work, and for his freely given advice.

Members of the Cosmic Ray Research Group are thanked for helpful discussion.

The technical staff of the Physics Department, in particular Mr. W. Leslie, Mr. P. Finley, Mr. K. Tindale, Mr. J. Webster, Mr. M. Lee and Miss P. Wallace are thanked for their willing help. The assistance of the staff of the University Computer Unit, and the use of their facilities is acknowledged with gratitude.

The author is grateful to Mrs. J. Moore for her patient work in preparing this thesis.

Finally the Science Research Council is thanked for the provision of a Research Studentship, without which this work could not have been carried out.

REFERENCES

P.I.C.C.R. : Proceedings of the international conference on Cosmic Rays.

ALEXEYEV, I.S., and ZATSEPIN, G. T., (1959), P.I.C.C.R., Moscow, 1, 324.

ALLEN, J. E., and APOSTOLAKIS, A. J., (1961), Proc. Roy. Soc., A265, 117.

ASHTON, F., and WOLFENDALE, A. W., (1963), Proc. Phys. Soc., 81, 593.

ASHTON, F., COATS, R. B., HOLYOAK, B., SIMPSON, D.A., and THOMPSON, M.G., (1965a), Nuc. Instrum. and Methods, 37, 181.

ASHTON, F., and COATS, R.B., (1965b), P.I.C.C.R., London, 2, 959.

ASHTON, F., KAMIYA, Y., MACKEOWN, P.K., OSBORNE, J. L., PATTISON, J.B.M., RAMANA MURTHY, P.V., and WOLFENDALE, A.W., (1966), Proc. Phys. Soc., 87, 79.

ASHTON, F., COATS, R.B., KELLY, G. N., SIMPSON, D.A., SMITH, N.I., TAKAHASHI, T., (1967), P.I.C.C.R., Calgary, to be published.

ASHTON, F., COATS, R.B., and SIMPSON, D.A., (1967b), P.I.C.C.R., Calgary, to be published.

ASHTON, F., and COATS, R.B., (1967c), P.I.C.C.R., Calgary, to be published.

BACKENSTOSS, G., HYAMS, B.D., KNOP, G., MARIN, P.C., and STIERLIN, U., (1963), Phys. Rev., 129, 2759.

BARRETT, P.H., BOLLINGER, L.M., COCCONI, G., EISENBERG, Y., and GREISEN, K., (1952), Rev. Mod. Phys., 24, 133.

BARTON, J.C., BARNABY, C.F., JASANI, B. M., and THOMPSON, C.W., (1962), J. Sci. Instrum., 39, 360.

BARTON, J.C., ROGERS, I.W., and THOMPSON, M.G., (1966), Proc. Phys., Soc., 87, 101.

BELENKII, S.Z., and IVANENKO, I.P., (1959), Usp. Fiz. Nauk., 69, 591.

BHABBA, H.J., (1935), Proc. Roy. Soc., A152, 559.

BHABBA, H. J., (1938), Proc. Roy. Soc., A164, 257.

BIBILASHVILI, M.F., BARNAVELI, T.T., GRUBELASHVILI, G.A., and MURADOVA, N.A., (1965), P.I.C.C.R., London, 2, 956.

BOROG, V.V., KIRILLOV-UGRYUMOV, V.G., PETRUKHIN, A.A., ROSENTAL, I.L., and SHESTAKOV, V.V., (1965), P.I.C.C.R., London, 2, 962.

BROOKE, G., HAYMAN, P.J., KAMIYA, Y., and WOLFENDALE, A.W., (1964a), Proc. Phys. Soc., 83, 853.

BROOKE, G., and WOLFENDALE, A.W., (1964b), Proc. Phys. Soc., 83, 843.

BROOKE, G., MEYER, M.A., and WOLFENDALE, A.W., (1964c), 83, 871. Proc. Phys. Soc.

BUJA, Z., (1963), Acta Physica Pol., 24, 381.

CHAUDHURI, N., and SINHA, M.S., (1964), N.C., 32, 853.

CHAUDHURI, N., and SINHA, M.S., (1965), N.C., 35, 13.

CHRISTY, R.F., and KUSAKA, S., (1941), Phys. Rev., 59, 405.

COCCONI, G., KOESTER, L.J., and PERKINS, D.H., (1961), Lawrence Radiation Lab. High Energy Physics Study Seminars No. 28 pt.2 (UCID) - 1444.

CRAWFORD, D.F., and MESSEL, H., (1965), Nuc. Phys., 61, 145.

DEERY, R. F., and NEDDERMEYER, S.H., (1961), Phys. Rev., 121, 1803.

DENISOV, E.V., DEDENKO, L.G., DUBROVINA, S.A., DENIKAEV, R.Z., EMELJANOV, Yu.A., FETISOV, F.N., LUKIN, Yu.T., MOROSOV, A.E., OGURZOV, O.F., SOKOLOVSKY, V.V., SLAVATINSKY, S.A., and TAKIBAYEV, J.S., (1965), P.I.C.C.R., London, 2, 824.

DMITRIEV, V.A., and KHRISTIANSEN, G.B., (1963), J.E.T.P.,(Eng.Trans.) 17, 276.

FOWLER, G.N., and WOLFENDALE, A.W., (1958), Prog. in elementary particle and C.R. Physics, Vol. IV, Chapter 3, (Eds: J. G. Wilson and S. A. Wouthuysen: North-Holland).

FURRY, W.H., (1937), Phys. Rev., 52, 569.

GAEBLER, J.F., HAZEN, W.E., and HENDAL, A.Z., (1961), N.C., 19, 265.

GEORGE, E.P., and EVANS, J., (1950), Proc. Phys. Soc., A,63, 1248.

GERASIMOVA, N.M., (1965), Bull. Acad. Sci., U.S.S.R., Ser. No. 11 64, 1758.

GREEN, J.R., and BARCUS, J.R., (1959), N.C., 14, 1356.

HIGASHI, S., KITAMURA, T., WATASE, Y., ODA, M., and TANAKA, Y., (1964), N.C., 32, 1.

HIGASHI, S., et al., (1966), private communication to Professor A. W. Wolfendale.

HILTON, L.K., (1967), Ph.D. Thesis, University of Utah.

IVANENKO, I.P., and SAMOSUDOV, B.E., (1959), JETP, 8, 884, (Eng.Trans.)

JAKEMAN, D., (1956), CANADIAN J. Phys., 34, 432.

JUDGE, R.J.R., and NASH, W.F., (1964a), N.C., 35, 1025.

JUDGE, R.J.R., and NASH, W.F., (1964b), N.C., 35, 999.

KAWAGUCHI, S., SAKAI, T., ODA, H., UENO, H., and KAMIYA, Y., (1965), P.I.C.C.R., London, 2, 941.

KERNS, Q.A., KIRSTEN, F.A., and COX, G.C., (1959), Rev. Sci. Instrum., 30, 34.

KRASILNIKOV, D.D., (1965), Bull. Acad. Sci. U.S.S.R., Ser. No. 11, 64, 1742.

LAMB, R.C., LUNDY, R.A., NOVEY, T.B., and YOVANOVITCH, D.D., (1966), Phys. Rev. Letters, Vol. 17, 20, 1068.

LATTES, C.M.G., MUIRHEAD, H., OCCHIALINI, G.P.S., and POWELL, C.F., (1947), Nature, 159, 694.

MACKEOWN, P.K., SAID, S.S., WDOWCZYK, J., and WOLFENDALE, A.W., (1965), P.I.C.C.R., London, 2, 964.

MAEDA, K., (1964), J. of Geophysical Research, 69, 1725.

MALHOTRA, P.K., SHUKLA, P.G., STEPHENS, S.A., VIJAYALAKSHMI, B., BOWLER, M.G., FOWLER, P.H., HACKFORTH, H.L., KEEREETAVEEP, J., MAYES, V.M., and TOVEY, S.N., (1966), Nature, 209, 567.

MATANO, T., NAGANO, M., SHIBATA, S., SUGA, K., KAMEDA, T., TOYADA, Y., and MAEDA, T., (1965), Phys. Rev. Letters, 15, 594.

MCDIARMID, I.B., and WILSON, M.D., (1962), Canad. J. Phys., 40, 698.

MITRA, S.M., and ROSSER, W.G.V., (1949), Proc. Phys. Soc., A62, 364.

MITRA, A.N., (1957), Nuc. Phys., 3, 262.

MORRISON, P.R.O., (1963), CERN Preprint, 63-1.

MORTON, G.A., (1949), R.C.A. Rev., 10, 525.

MUROTA, T., UEDA, A., and TANAKA, H., (1956), Prog. Th. Phys.,(Kyoto), 16, 482.

MURZIN, V.S., and RAPOPORT, I.D., (1965), JETP, 20, 1-3.

NASSAR, S., and HAZEN, W.E., (1946), Phys. Rev., 69, 298.

OSBORNE, J.L., (1966), Ph.D. Thesis, University of Durham.

OSBORNE, J.L., WOLFENDALE, A.W., and PALMER, N.S., (1964), Proc. Phys. Soc., 84, 911.

OTT, K., (1954), Z. Naturforsch, 9A, 488.

PAK, W., OZAKI, S., ROE, B.P., and GREISEN, K., (1961), Phys. Rev., 121, 905.

PATTISON, J.B.M., (1965), Ph.D. Thesis, University of Durham.

PERKINS, D.H., (1961), Prog. in Elementary Particle and C.R. Physics, (Eds: Wilson, J.G., and Wothuysen, S.A., North-Holland).

PIPKIN, F.M., (1965), Proc. Int. Conf. on Elementary Particles, Oxford, 1, 61.

RICHARDS, J.A., and NORDHEIM, L.W., (1948), Phys. Rev., 74, 1106.

ROE, B.P., and OZAKI, S., (1959), Phys. Rev., 116, 1022.

ROGERS, I.W., (1965), Ph.D. Thesis, University of Durham.

ROSSI, B., (1952), High Energy Particles (Prentice Hall Inc.).

SAID, S.S., (1966), Ph.D. Thesis, University of Durham.

SIMPSON, D.A., (1964), M.Sc. Thesis, University of Durham.

SMITH, J.A., and DULLER, N.M., (1959), J. Geophys. Res., 64, 2297.

TAKBAEV, Zh.S., LUKIN, Yu.T., and EMELYANOV, Yu.A., (1965),
P.I.C.C.R., London, 2, 967.

VERNOV, S.N., KHRISTIANSEN, G.B., NETCHIN, YU.A., VEDENEEV, O.V.,
and KHRENOV, B.A., (1965), P.I.C.C.R., London, 2, 952.

YUKAWA, H., (1935), Proc. Phys. Math. Soc., Japan, 17, 48.

ZATSEPIN, G.T., and KUZ'MIN, V.A., (1961), JETP, 12, 1171.
(Eng. Trans.).

APPENDIX A

LIQUID PARAFFIN SCINTILLATION COUNTERS

A1 Experimental

The scintillation counters used in the experiments described in this thesis are of the design recommended by Barton et al. (1962). A comprehensive study of the properties of these counters has been carried out by Simpson (1964). This appendix is concerned with the physical properties of the light guides, and an estimate is made of the fraction of the produced light that is collected by the photomultipliers, from which the absolute scintillation efficiency of the phosphor has been evaluated.

The liquid phosphor, medicinal paraffin plus 0.5 g. l^{-1} of p-terphenyl and 0.005 g.l^{-1} of POPOP, is contained in a rectangular Perspex box ($\frac{3}{8}$ in. wall thickness, dimensions 130 x 90 x 17.8 cms). This box is mounted in a larger light-tight wooden box on wooden rods so that light is transmitted in the phosphor by total internal reflection. One photomultiplier (E.M.I. type 9583 B) views the phosphor through a rectangular light guide consisting of plane mirrors mounted in air along the sides WX, YZ and AEHD (figure A1). A second photomultiplier views the phosphor from the other end.

Measurements were made of the pulse height distribution produced by photomultiplier PM_2 as a function of the position of relativistic muons traversing the counter along its centre line.

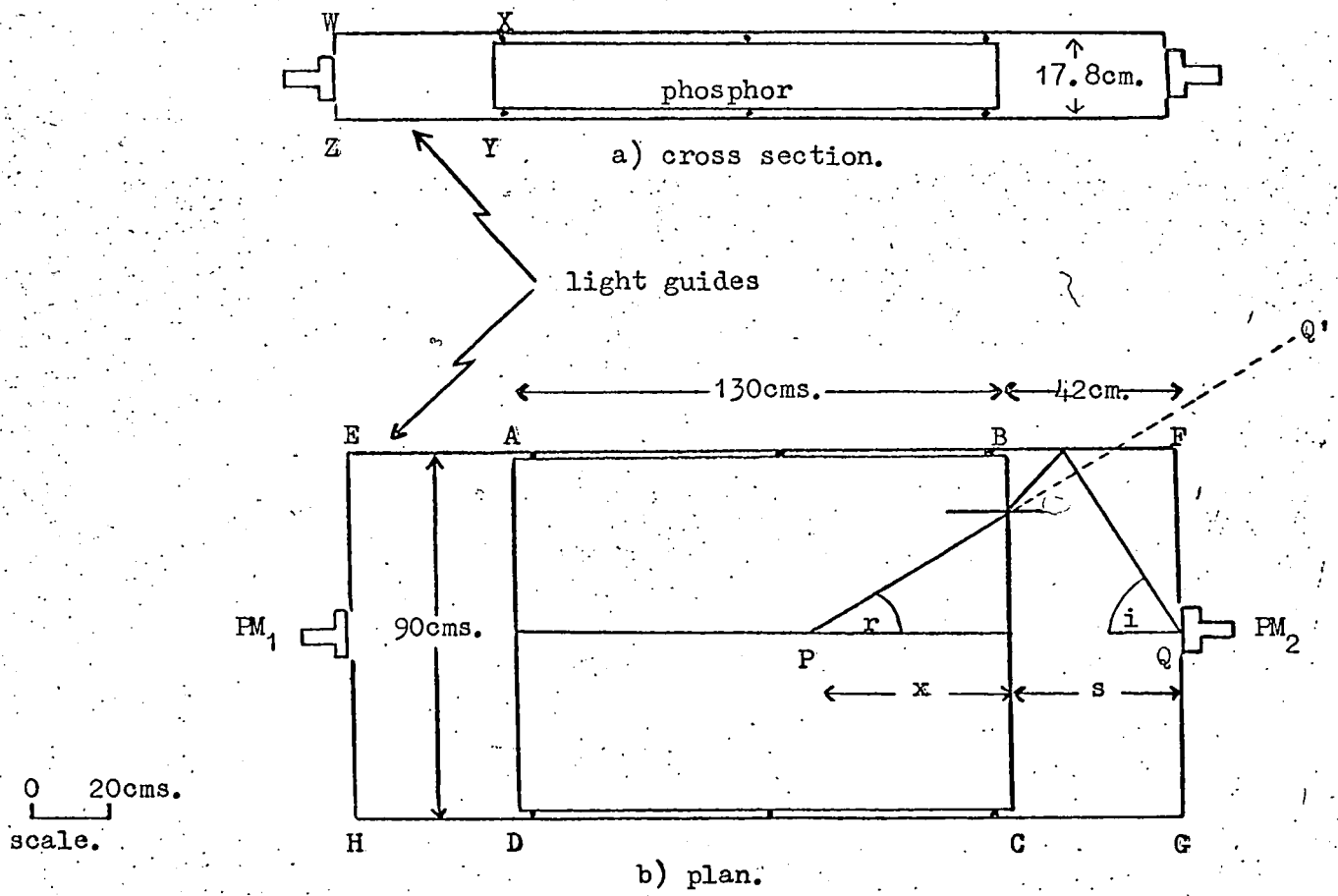

Figure A1. Scale diagram of a liquid paraffin scintillation counter.

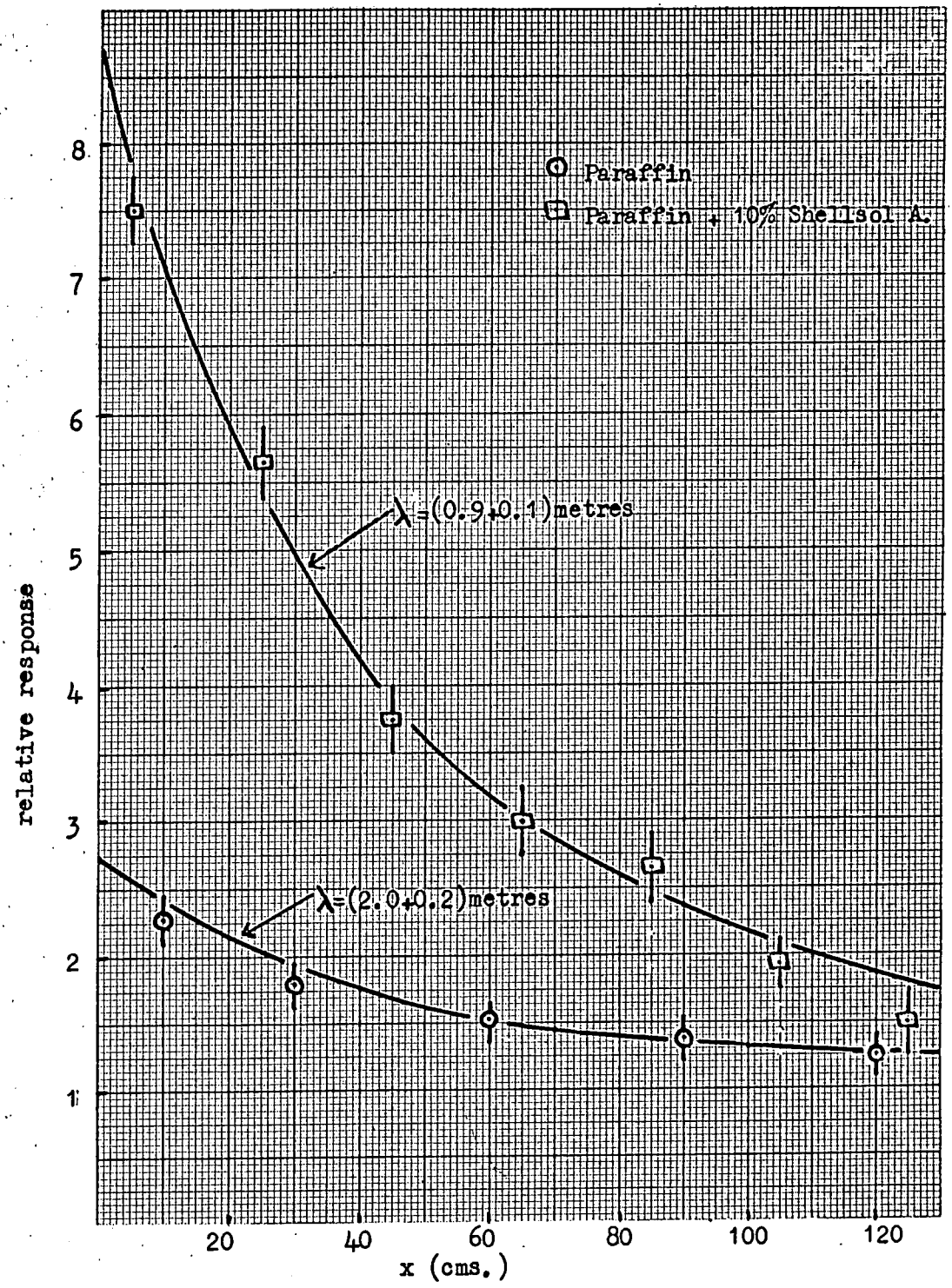

Figure A.2. Response of photomultiplier PM_2 as a function of the position of particles traversing the counter along its centre line.

This was carried out by means of a small scintillator telescope so that only muons traversing a small region of the counter normal to its area were selected. The results are shown in figure A2, together with those for the same phosphor plus 10% Shellsol A (Simpson, 1964) for comparison. These measurements give a measure of the attenuation length of scintillation light in the phosphor.

A2 Light collection in the counter

Consider a rectangular slab of transparent material, refractive index n, mounted in air, and within which there is an isotropic point source of light. Light leaves the slab in six escape cones each of half-angle θ_c, where θ_c is the critical angle. The remaining light is trapped inside the slab, and undergoes repeated reflections until it is absorbed. Thus the fraction of light leaving the slab is $3[1-(n^2-1)^{\frac{1}{2}}/n]$. For organic liquids and perspex n is 1.485, so that each escape cone contains 13% of the produced light, and 22% is trapped in the phosphor. Hence, in the counter described, only the scintillation light emitted in the two escape cones directed towards the photomultipliers (26%) is available for collection. To calculate the fraction of this light that is collected by the photomultipliers it is necessary to know the attenuation length of scintillation light in the phosphor. This can be determined from the results in figure A2.

Consider a point P on the centre line of the phosphor at a distance x + s from photomultiplier PM_2. Due to refraction at the phosphor boundary the image of the point Q at the centre of the photocathode of PM_2 appears to be at Q′. By summing the solid angles subtended at P by all such reflected images, the fraction of produced light that is collected by either photomultiplier can be determined and is given by:

$$\frac{1}{4\pi} \sum_i \frac{A \cos \theta}{d_i^2} f_1 f_2 \exp(d_i'/\lambda)$$

where A is the area of the photocathode, d_i' is the path length in the phosphor of a light ray corresponding to the ith image of the photomultiplier at a distance d_i, θ is the angle that the ray makes with the normal to the photocathode, and λ is the attenuation length of scintillation light in the phosphor. f_1 is a correction factor introduced to account for the reduction in solid angle due to refraction at the phosphor boundary, and $f_2 = r^n$ where r is the reflection coefficient of the light guide mirrors and n is the number of mirror reflections. r = 0.9 when averaged over the POPOP emission spectrum. In the particular case illustrated in figure A1, $d_i = (x \sec(r) + s \sec(i))$, $d_i' = x \sec(r)$.

For a given value of λ the expected response of photomultiplier PM_2 was calculated for different positions along the centre line of the counter, and λ was then relaxed until the best fit with the experimental data was obtained. The results are shown in figure A2, and are $\lambda = (2.0 \pm 0.2)$m for the paraffin phosphor and $\lambda = (0.9 \pm 0.1)$m

when 10% Shellsol A is added.

In normal use the gains of both photomultipliers are adjusted to be equal, and the pulses from each are added linearly. Under these conditions the uniformity of response (percentage difference between the response at a given point to the response averaged over the whole area for particles traversing the counter at normal incidence) has been investigated. The worst position is found to be directly opposite the photomultiplier, at a point on the counter axis, the non-uniformity being a maximum there with a value of 18%.

A3 The absolute scintillation efficiency of the phosphor

The absolute scintillation efficiency η of a phosphor is defined as the amount of energy a relativistic particle must lose in the phosphor to produce one scintillation photon. If E is the energy lost by a relativistic particle traversing the counter through its centre point and normal to its largest area, then

$$\eta = E \alpha_1 \alpha_2 / n$$

where α_1 is the fraction of produced light collected by both photomultipliers, α_2 is the quantum efficiency of their photocathodes and n is the number of photoelectrons produced by the two photomultipliers. The light collection calculations give $\alpha_1 = 0.017$ for a value of $\lambda = 2.0$m, and $\alpha_2 = 0.12$ according to the data provided by the photomultiplier manufacturers. The value of n for the paraffin phosphor has been measured by three independent methods

as discussed by Morton (1949).

(a) The most probable pulse height (v) of the distribution produced by the passage of single muons through the centre of the counter was measured. The particles were selected by a small telescope. The number of photoelectrons (N) at the photocathode corresponding to this pulse height is related to v by the equation:

$$N = \frac{C_o v}{Ge}$$

where G is the absolute gain of the photomultiplier, C_o is the capacitance across which the pulse is formed, and e is the electronic charge.

The absolute gain of each photomultiplier was measured using a method suggested by Morton (1949). Firstly one photomultiplier was operated at a low voltage, so that the gain was correspondingly low ($\sim 10^3$), and the input and output currents produced by a dim light directed at the photocathode were measured directly with a scalamp galvanometer, from which the gain was evaluated. Next the intensity of the light was reduced. The anode current was again measured using the galvanometer, and the input current calculated knowing the value of the gain. Finally the E.H.T. was increased to the operating value, and the anode current remeasured, keeping the intensity of the bulb, and hence the input current, the same. The absolute gain was then determined as the ratio of the anode and the input currents.

The capacity C_o was extrapolated from observations on the variation of pulse height with capacity as different capacities were connected in parallel with C_o.

From these measurements the number of photoelectrons corresponding to the passage of a single muon through the centre of the counter was found to be n = 29.

(b) The basic source of noise in a photomultiplier is due to thermionic emission from the photocathode. In principle the mean pulse height (vo) of the distribution (standard deviation σo) produced by thermal electrons corresponds to the emission of a single electron from the photocathode. The total dark current and the integral distribution of pulse heights produced by thermal electrons have been measured for each photomultiplier, from which the mean pulse height produced by a single photoelectron was deduced. The ratio v/vo gives a value of n = 47.

(c) The measured full width at half height of the distribution of pulse amplitudes due to the passage of muons through the centre of the counter is 80% and this gives a value of n = 16, allowing for ionization loss fluctuations (Landau distribution) of 15% and fluctuations in the photomultiplier process. The contribution to the fractional full width at half height due to fluctuations in the number n of photoelectrons produced is $2.36/\sqrt{n}$, and that due to fluctuations in the multiplication process in the photomultiplier is $2.36\ \sigma o/(vo\sqrt{n})$. The measured value of $\sigma o/vo = 0.91$, and table

A1 shows the numerical contributions of the different fluctuation processes to the full width at half height of the scintillation distribution.

TABLE A1.

FLUCTUATION PROCESS	CONTRIBUTION TO FULL WIDTH AT HALF HEIGHT (%)
LANDAU	15
PHOTOELECTRON PRODUCTION	58
PHOTOMULTIPLIER CASCADE	53

The three methods produce widely differing results, indicating the difficulties involved in making an evaluation of n. Taking the average value as n = 31 ± 9 photoelectrons, and a value of E = 28.5 MeV (Ashton et al (1965)), the absolute scintillation efficiency is

$$\eta = (1.82 \pm 0.53) \text{ kev/photon.}$$

A4 Conclusions

Figure A2 shows that the response of the paraffin phosphor can be improved by the addition of 10% Shellsol A. However, the uniformity is correspondingly worsened, due to the shorter attenuation length of photons in the phosphor. Both the experiments described in this thesis require as uniform a response as possible over the area of the counter. Hence the paraffin phosphor has been preferred. The particular counters employed are uniform to 18%

over 99.5% of their areas.

APPENDIX B

SPURIOUS FLASHING IN NEON FLASH TUBES

Experiments designed to measure low density events and comprising large arrays of neon flash tubes may be handicapped by the spurious flashing of the tubes. The manufacture ofa large number of tubes consists of making a number of small batches, and these are necessarily made at different times. Although every effort is made to ensure that the same conditions exist during each separate batch filling, the composition and purity of fillings may vary from batch to batch. In an attempt to determine the effect of variations in the purity of the filling of a particular tube on its spurious flashing rate, two sets of tubes were selected. Batch A consisted of standard flash tubes, internal diameter 1.55 cms and external diameter 1.8 cms, filled with commercial neon (98% Ne. 2% He) to a pressure of 60 cm Hg. Similar tubes with the same filling, but to each of which was added a quantity of iron filings, comprised batch B.

A high voltage pulse (rise time 1μs and duration 4μs) was applied to two electrodes, between which were situated the two batches of tubes. A high voltage probe (Tektronix P6013) was employed to display the applied pulse on an oscilloscope (Tektronix 543A), by which means the pulse height was determined. The stack was randomly triggered with a pulse generator at a frequency of 1 per 7 seconds, and the number of flashes per trigger in each batch was recorded

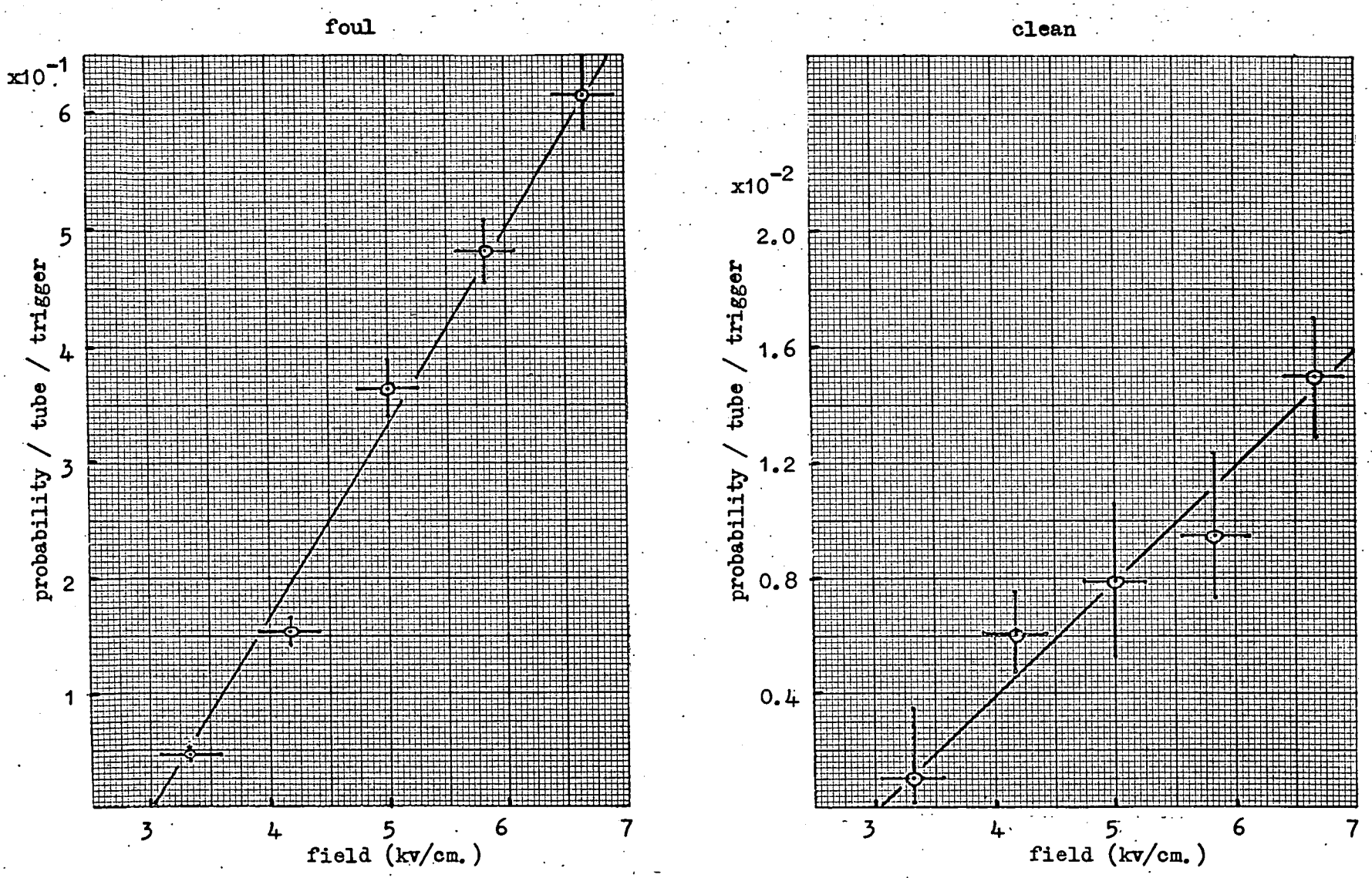

Figure B.1. Probability of spurious flashing as a function of applied field in clean and contaminated flash tubes.

for various applied pulse heights. The probability/tube/trigger as a function of the electric field is shown in figure B1 for both batches. Each batch commences to flash spuriously at a field of ~3 kv./cm., but the rate of flashing in the contaminated batch increases more quickly than the pure batch, so that at a field of 6 kv/cm the probability of a spurious flash in the contaminated batch is 50%,as compared with 1.2% in the pure batch.

The results show that the tubes containing a small quantity of iron filings are more prone to spurious flashing than the standard tubes. Local distortions in the field due to sharp edges in the filings lead to breakdown, and other matter in the tube, such as dust, would produce the same effect. No attempt has been made to establish any quantitative relationship between the impurity content and the probability of spurious breakdown rate, but this study emphasises the importance of obtaining filling conditions which are as clean as possible.